



저작자표시-비영리-변경금지 2.0 대한민국

이용자는 아래의 조건을 따르는 경우에 한하여 자유롭게

- 이 저작물을 복제, 배포, 전송, 전시, 공연 및 방송할 수 있습니다.

다음과 같은 조건을 따라야 합니다:



저작자표시. 귀하는 원저작자를 표시하여야 합니다.



비영리. 귀하는 이 저작물을 영리 목적으로 이용할 수 없습니다.



변경금지. 귀하는 이 저작물을 개작, 변형 또는 가공할 수 없습니다.

- 귀하는, 이 저작물의 재이용이나 배포의 경우, 이 저작물에 적용된 이용허락조건을 명확하게 나타내어야 합니다.
- 저작권자로부터 별도의 허가를 받으면 이러한 조건들은 적용되지 않습니다.

저작권법에 따른 이용자의 권리는 위의 내용에 의하여 영향을 받지 않습니다.

이것은 [이용허락규약\(Legal Code\)](#)을 이해하기 쉽게 요약한 것입니다.

[Disclaimer](#)

공학박사 학위논문

**3D printing of porous shape memory polymers  
via frontal polymerization and their applications  
to space environment**

정면 중합을 이용한 다공성 형상기억고분자의

삼차원 프린팅 및 우주환경 응용

2021 년 8 월

서울대학교 대학원

재료공학부

장 준 혁

**3D printing of porous shape memory polymers  
via frontal polymerization and their applications  
to space environment**

Advisor: Woong-Ryeol Yu

by

Joon Hyeok Jang

2021

Department of Materials Science and  
Engineering Graduated School Seoul  
National University

# 3D printing of porous shape memory polymers via frontal polymerization and their applications to space environment

정면 중합을 이용한 다공성 형상기억고분자의 삼차원 프린팅 및  
우주환경 응용

지도 교수 유 응 열

이 논문을 공학박사 학위논문으로 제출함

2021 년 6 월

서울대학교 대학원

재료공학부

장 준 혁

장준혁의 공학박사 학위논문을 인준함

2021 년 6 월

위 원 장 \_\_\_\_\_ 안 철 희 \_\_\_\_\_

부 위 원 장 \_\_\_\_\_ 유 응 열 \_\_\_\_\_

위 원 \_\_\_\_\_ 이 명 규 \_\_\_\_\_

위 원 \_\_\_\_\_ 구 남 서 \_\_\_\_\_

위 원 \_\_\_\_\_ 나 원 진 \_\_\_\_\_

# Abstract

Shape memory polymers (SMPs) are attracting attention as deployment structures in space environments due to their high deformability, lightweight and self-depolyable properties. However, they have the disadvantage of being vulnerable to space environments such as heat, ultraviolet radiation, atomic oxygen. Prediction model of long-term properties in aerospace and proper design and manufacturing method for long-term durability of shape memory polymer are required.

To predict long-term properties of shape memory polymer in the space environment, an accelerated testing method was proposed. It is hard to simulate the space environment in practice, and it is difficult to observe properties change of shape memory polymer continuously for a long time. Therefore, a prediction model for the long-term durability of shape memory polymers in the space environment was suggested based on the time-temperature superposition principle. The storage modulus of shape memory polymer was investigated in a simulation of a low Earth orbit (LEO) environment involving three harsh conditions: high vacuum, and atomic oxygen (AO) and ultraviolet (UV) light exposure. SMP in a LEO environment

degrade over time due to temperature extremes and matrix erosion by AO. The opposite behavior was observed in our experiments, due to crosslinking induced by AO and UV light exposure in the LEO environment. The effects of the three harsh conditions on the properties of SMPs were characterized individually, using accelerated tests conducted at various temperatures in a space environment chamber, and were then combined using the time–temperature superposition principle. The long-term mechanical behavior of SMPs in the LEO environment was then predicted by the linear product of the shift factors obtained from the three accelerated tests. The results also indicated only a slight change in the shape memory performance.

Porous shape memory polymers are suggested for long-term durability. Porous polymers are used as shielding materials due to their large surface area. Due to the low thermal conductivity of the air and the reflection of radiation due to the large surface area, they are used as insulators, and also used as electromagnetic interference shielding materials due to internal reflection. However, the porous structure has a disadvantage in that mechanical properties are poor. Therefore, it is necessary to design a porous structure with excellent shielding properties while maintaining mechanical properties. A new 3D printing process was developed to print porous shape memory polymer. The ability to print geometrically complex, free-standing forms with

SMPs is crucial for extend application of SMP. A SMP capable of frontal polymerization featuring exothermic self-propagation was synthesized by adding cyclooctene to a poly(dicyclopentadiene) network, resulting in switching segments. The rheological properties of this SMP were controlled by adjusting incubation time. A nozzle system was designed such that the SMP could be printed with simultaneous polymerization to yield a free-standing structure. Additionally, core-shell nozzle was introduced to generate pore inside the polymer matrix. The porous structure was successfully printed and structural properties were analyzed. Porosity was formed in the low porosity region between 0 and 0.1 under various printing conditions. Thermal/mechanical properties were analyzed and verified through finite element modeling. Elastic modulus and thermal conductivity decreased linearly with porosity, and at a porosity of 0.1, they decreased by 19% and 12%, respectively. Finally, a shape memory polymer having a porous structure was printed in a free-standing structure and shape memory properties were characterized.

Keywords: Shape memory polymer, space environment, porous structure, 3D printing, frontal polymerization

Student number: 2015-22757

# Contents

<b>Abstract.....</b>	<b>i</b>
<b>Contents.....</b>	<b>iv</b>
<b>List of Tables.....</b>	<b>vii</b>
<b>List of Figures.....</b>	<b>viii</b>
<b>1. Introduction.....</b>	<b>1</b>
1.1. Shape memory polymers and their application.....	1
1.2. 3D printing process of shape memory polymers.....	3
1.3. 3D printing method of porous shape memory polymers.....	4
1.4. Research objectives.....	6
<b>2. Prediction of long-term properties of shape memory polymer /composite in a Low earth orbit.....</b>	<b>8</b>
2.1. Experimental.....	10
2.1.1. Materials and sample preparation.....	10
2.1.2. Environmental chamber and acceleration test.....	12
2.1.3. Characterization.....	15
2.2. Effects of Ultraviolet irradiation.....	17
2.2.1. Effects of UV irradiation and exposure temperature.....	17
2.2.2. Acceleration effects of time degradation by temperature.....	22
2.2.3. Quantitative analysis of the UV effects on long-term properties.....	25

2.3. Effects of Atomic oxygen irradiation.....	31
2.3.1. Effects of AO irradiation and temperature on matrix erosion.....	31
2.3.2. Quantitative analysis of the AO effects on long-term properties.....	36
2.4. Effects of a Low earth orbit environment.....	41
2.4.1. Quantitative analysis of long-term properties under LEO environment..	41
2.4.2. Shape memory properties under UV/AO/LEO environments.....	50
2.5. Summary.....	52
<b>3. 3D printing of shape memory polymer.....</b>	<b>54</b>
3.1. Experimental.....	56
3.1.1. Materials and sample preparation.....	56
3.1.2. Characterization.....	57
3.1.3. 3D printing process for shape memory polymer.....	59
3.2. 3D printing of frontal polymerized shape memory polymer .....	60
3.2.1. Thermomechanical and shape memory properties.....	60
3.2.2. Rheological properties and frontal properties.....	64
3.2.3. 3D printing and the shape memory properties of <i>fp</i> SMP.....	69
3.3. Summary.....	72
<b>4. 3D printing of porous shape memory polymers.....</b>	<b>73</b>
4.1. Experimental.....	74
4.1.1. Materials and sample preparation.....	74
4.1.2. 3D printing system for porous shape memory polymer.....	75
4.1.3. Characterization.....	77

4.2. Modelling approach of mechanical/thermal analysis of porous structure.....	78
4.2.1. Generation of porous structure.....	78
4.2.2. Mechanical/thermal analysis of porous structure.....	78
4.3. 3D printing of porous shape memory polymer.....	80
4.3.1. Structural analysis of porous shape memory polymer.....	80
4.3.2. Mechanical/thermal properties of porous shape memory polymer.....	84
4.3.3. 3D printing of <i>fp</i> SMP and shape memory properties.....	87
4.3. Summary .....	91
<b>5. Conclusions.....</b>	<b>92</b>
<b>Reference.....</b>	<b>94</b>
<b>Korean abstract.....</b>	<b>108</b>

## List of Tables

Table 2-1 Curing schedule of the samples

Table 2-2 Glass transition temperature of unexposed and UV-exposed SMPCs

Table 2-3 Glass transition temperature and storage modulus of UV- exposed SMPC with different treatment temperatures and times.

Table 2-4 Mass change of Kapton® HN film and atomic oxygen (AO) flux estimation.

Table 2-5 Thermal properties and mass loss of AO-exposed carbon fiber-reinforced shape memory polymer composites (CF-SMPCs).

Table 2-6 Thermomechanical properties and mass loss for five validation data sets in an AO environment.

Table 2-7 Thermomechanical properties of LEO-exposed CF-SMPCs

Table 2-8 Thermomechanical properties for five validation datasets in a low-Earth orbit (LEO) environment

Table 2-9 Shape memory properties of unexposed and UV/AO/LEO-exposed CF-SMPCs

Table 3-1 Thermomechanical and shape memory properties of *fpSMP*.

Table 4-1 Material parameter for mechanical/thermal analysis

Table 4-2 Average pore diameter of porous *fpSMP* at each printing condition

## List of Figures

Figure 2-1 DSC analysis of CF-SMPCs according to curing schedule

Figure 2-2 Space environmental chamber: (a) schematic diagram, (b) built-in chamber, and (c) overall appearance

Figure 2-3 Effects of VUV exposure on carbon fiber-reinforced shape memory epoxy/polymer composites (CF-SMPCs): (a) thermomechanical behavior (straight line – storage modulus, dash line – tangent delta), (b) FTIR spectra, (c) the absorbance changes in the characteristic peak, and (d) the surface morphology.

Figure 2-4 (a) Storage modulus of unexposed CF-SMPCs as a function of temperature (left) and its master curve determined at 70°C (right), and (b) the corresponding shift factors used to build the master curve.

Figure 2-5 Thermomechanical behavior of VUV-exposed SMPCs. (a) Storage moduli measured as a function of frequency at a reference temperature of 70°C (in DMA) and a master curve built at the reference temperature of 70°C (in the VUV chamber), and (b) shift factors for the master curve.

Figure 2-6 Long-term variation in the storage modulus of CF-SMPCs when left at 70°C under VUV irradiation. Legends for each data point represent VUV-exposure conditions. The original data were subjected to shift operations.

Figure 2-7 Effects of atomic oxygen (AO) exposure on surface morphology of carbon fiber-reinforced shape memory polymer composites (CF-SMPCs) according to exposure temperature: (a) unexposed, (b) 70°C, (c) 110°C and (d) 150°C

Figure 2-8 Effects of atomic oxygen (AO) exposure on CF-SMPCs: (a) mass loss, (b) thermomechanical behavior (straight line—storage modulus, dashed line—tangent delta), (c) Fourier transform in-frared (FT-IR) spectra and (d) thermogravimetric analysis/differential thermal analysis (TGA/DTA) data.

Figure 2-9 Thermomechanical behavior of AO-exposed CF-SMPCs. (a) Storage moduli measured as a function of frequency at a reference temperature of 70 °C using dynamic mechanical thermal analysis (DMA) and the master curve built at the reference temperature of 70 °C, and (b) shift factors for the master curve.

Figure 2-10 Long-term variation in the storage modulus of CF-SMPCs when maintained at 70°C under AO irradiation. Legends for each data point represent the AO exposure conditions. The original data were subjected to shift operations.

Figure 2-11 Effects of LEO exposure on CF-SMPCs: (a) thermomechanical behavior, (b) FT-IR spectra, and (c) TGA/DTA curve of LEO-exposed CF-SMPCs.

Figure 2-12 Thermomechanical behavior of LEO-exposed SMPCs. (a) Storage moduli measured as a function of frequency at a reference temperature of 70 °C (in DMA) and a master curve built at the reference temperature of 70 °C, and (b) shift factors for the master curve.

Figure 2-13 Long-term variation in the storage modulus of CF-SMPCs when maintained at 70 °C under a LEO environment. Legends for each data point represent the LEO-exposure conditions. The original data were subjected to shift operations.

Figure 2-14 Master curve for each environment (UV, AO and LEO exposure). Each data point represents an experimental value.

Figure 2-15 Shape memory properties of unexposed-CF SMPCs (cyclic test)

Figure 3-1 (a) Schematic diagram of frontal polymerization and (b) polymerization mechanism and chemical structure of frontal SMP.

Figure 3-2 TGA analysis of *fpSMP* according to CO content.

Figure 3-3 (a) Thermomechanical behavior of *fpSMP* according to CO content (straight line - storage modulus, dash line - tan delta) and (b) shape memory behavior is shown for a formulation containing 0.15 molar equivalents of CO.

Figure 3-4 (a) Rheological properties of *fpSMP* and (b) the appearance of extruded filaments at each state

Figure 3-5 (a) Frontal polymerization of *fpSMP* ink, (b) IR camera image for frontal velocity, and (c) frontal velocity according to incubation time.

Figure 3-6 (a) Schematic showing the printing head used to extrude *fpSMP*, (b) 3D design of free-standing structure along with a (c) picture of the actual 3D-printed part.

Figure 3-7 Shape memory behavior of 3D printed *fpSMP* under (a) tensile deformation and (b) compressive deformation.

Figure 4-1 Schematic diagram of (a) 3D printing system for porous shape memory polymer (b) core-shell nozzle and (c) cooling chamber with Peltier cooler

Figure 4-2 Printability of porous shape memory polymer at different printing condition

Figure 4-3 (a) Reconstructed 3D micro CT image and (b) 2D micro CT image of porous *fp*SMP (Flow rate : 1.57ml/min, air pressure : 0.08 MPa)

Figure 4-4 Porosity of printed *fp*SMP at each printing condition (a) 1.56 ml/min (b) 5.41 ml/min and (c) 15.93 ml/min

Figure 4-5 Experiment/simulation results of (a) mechanical (elastic modulus) and (b) thermal (thermal conductivity) of porous *fp*SMP

Figure 4-6 (a) 3D printing of a free-standing structure, (b) top/side view of printed *fp*SMP and (c) 3D/2D micro CT image of printed porous *fp*SMP

Figure 4-7 Shape memory behavior of 3D printed porous *fp*SMP under compressive condition

# **Chapter 1. Introduction**

## **1.1. Shape memory polymers and their application**

Shape memory polymers (SMPs) are materials that have the ability to memorize and recover their original shapes in response to specific stimuli [1]. Due to several additional advantages, including light weight, low cost, excellent recoverability, good manufacturability and high shape deformability, SMPs have been evaluated for use in various applications including biomedical stents or suture [2-6], robotic actuators [3, 7-9], and sensors [7, 10].

The stimuli required for recovery of SMPs have various forms such as heat, electrical voltage, magnetic field, and PH, and shape memory polymers are classified into various forms such as thermo-, electro-, magneto- and chemo- according to external stimulus [11, 12]. Each application field is different depending on the appropriate stimulus source. Among them, thermo-responsive shape memory polymer is the most widely used because it is easy to apply a stimulus and is the basic form of shape memory mechanism [13]. The shape memory mechanism can be explained thermodynamically. When the temperature rises above the transition region, the polymer chain becomes flexible and the SMP can be easily deformed. At this time, as SMP deforms, entropy is lost due to entropic elasticity. If the deformed state is maintained and temperature is lowered below the transition temperature, the deformed state becomes fixed due to strain-induced crystallization. Afterwards, if

the temperature is raised above the transition temperature by applying heat, the shape is restored while recovering the lost entropy [14]. However, SMPs have not been used as structural materials due to their low stiffness, strength, and recovery stress.

Shape memory polymer composites (SMPCs) have been developed to overcome these drawbacks. Currently, fiber-reinforced polymers meet these needs and are used as load-carrying components as well as structural materials. Carbon fiber-reinforced SMP has the great advantage that it is lighter than shape memory alloys [11, 13]. For this reason, many researchers have conducted research to apply shape memory polymer composites to the aerospace field. [14-26]. In the aerospace field, there is a disadvantage that an external power source is required to use the form of a deployment structure. In the case of SMPCs, since they have self-deployable properties, if shape memory programming is performed properly, they can be used as a deployable structure by recovering their shape by heat of solar radiation without an external power source in aerospace application [20, 27-31]. However, the durability of the polymer matrix must be ensured for use in the space environment. Therefore, both the mechanical properties and long-term durability of a structural material are important in space applications [31-34].

There are many factors that determine the long-term durability of SMPCs in low earth orbit (LEO) environments, including high vacuum, ultraviolet (UV) radiation, atomic oxygen, and micrometeoroids. High vacuum leads to outgassing of polymer matrix, and UV radiation can break the molecular bonds of the polymer causing degradation. In addition, AO causes surface erosion and degrades the mechanical

properties of the polymer composite [32-34]. For these reasons, the mechanical properties of polymers and polymer composites in a LEO environment have been of great interest [32-35]. Recently, research has been conducted on surface coating and reinforcement to protect against UV and AO exposure [33, 36, 37]. However, the long-term properties and durability of SMPCs in a LEO environment, i.e., for a duration of up to 10 years, have yet to be fully clarified [38]. Because long-term exposure tests in a LEO environment are not routine and can be practically inefficient, most studies have been conducted in the range of up to 100 h (typically several hours to tens of hours) [32, 34, 37-41]. Therefore, testing methods are required to assess the durability of SMPCs in LEO and the feasibility of SMPCs as structural materials in features such as hinges [16, 22], reflector antennas [13, 22, 42-46], reflectors [44], and morphing wings [10, 45].

In order to practically use SMPC in the space environment, it is necessary to ensure reliability for long-term properties. Therefore, it is necessary to present a model that can predict durability.

## **1.2. 3D printing process of shape memory polymer**

3D printing of shape memory polymer is called 4D printing in that a new dimension (i.e., time) is added to the existing 3D printing. In the case of SMP, their shape and physical properties can be changed over time after printing, and through this, functionality can be obtained [47]. In general, the most used materials for 4D printing

are hydrogels [48-52] and SMPs [53-57]. In the case of hydrogel, two materials with different degrees of swelling are printed at the same time, and the shape changes due to the difference in swelling, and through this, 4D printing can be realized. However, in the case of hydrogel, the mechanical properties are poor, the response speed is low, and it is dependent on the solvent [54]. On the other hand, in the case of SMP, it has high strength, good actuating force, and fast response speed. However, there is a disadvantage that a programming process is required after printing. The need for an additional programming process means that simple shape programming is possible, but it is difficult to change to a complex shape. In order to solve this problem, a manufacturing method using 3D printing of shape memory polymer is required. By appropriate design of 3D printing systems, a complex geometry can be printed and a shape programming process can be easily accomplished with a simple operation [54].

### **1.3. 3D printing methods of porous shape memory polymers**

Porous polymers are gaining increased interest in several areas due to their large surface area and unique physiochemical properties [58-62]. The difference in the properties of polymer and air and the large surface area are expanding the application range of porous polymers to separation membranes[58], electronic devices [62], and tissue engineering [63, 64]. In particular, porous polymers are used as shielding materials due to their large internal surface area [65]. Due to the low thermal

conductivity of the air and the reflection of radiation due to the large surface area, it is used as an insulator [66-68], and is also used as electromagnetic interference shielding materials due to internal reflection [61, 69]. However, the porous structure has a disadvantage in that mechanical properties are poor [70]. Therefore, it is necessary to design a porous structure with excellent shielding properties while maintaining mechanical properties.

Porous polymers are conventionally manufactured using microfluidic foaming [71, 72], gas foaming [73], freeze drying method [68, 74], and emulsion templating [75], supercritical fluids [76]. However, most methods of fabricating porous structures are not suitable for complex shapes [77]. Recently, research has been conducted on a method of 3D printing by introducing the above methods. A typical method is to use a supercritical fluid. It is a method of forming pores inside by lowering the pressure after injecting supercritical CO<sub>2</sub> into the thermoplastic polymer [76]. This method is not suitable for thermosetting polymers, and thermoplastic polymers have the disadvantage of poor thermal stability. Additionally, studies have been conducted on methods of forming a porous structure while injecting air from an inner nozzle using a core-shell nozzle using hydrogel [73]. However, it is not suitable for printing complex structures without support.

Among 3D printing materials, thermosetting polymers are useful for various applications due to their thermodynamic stability, excellent chemical resistance, and solvent resistance [78, 79]. However, thermosetting polymers have limited printing methods unlike thermoplastic polymers that can be 3D printed simply by fused

deposition modeling (FDM). Even in the case of stereolithography apparatus (SLA), and digital lighting processing (DLP), which are methods of curing the resin by irradiating light on the substrate after spraying the photocurable resin on the substrate in the material injection, there is a disadvantage in that it is limited to the photocurable resin [80]. Recently, a method of modifying the rheological properties of thermosetting resins to be suitable for 3D printing and post-curing after 3D printing has been developed, but this method has the disadvantage that the post-curing process takes 4 to 24 hours [79, 81-83]. Therefore, it is also need to develop a new 3D printing system for a porous thermosetting SMPs.

#### **1.4. Research objectives**

Shape memory polymers are attracting attention as deployment structures in space environments due to their high actuating force and self-depolyable properties. However, it has the disadvantage of being vulnerable to external environments such as heat and ultraviolet radiation. In order to solve this problem, a manufacturing method having a porous structure is required.

In Chapter 2, a method for predicting of long-term durability in the space environment was proposed. It is hard to simulate the space environment in practice, and it is difficult to observe properties change of shape memory polymer continuously for a long time. Therefore, it is limited to methods such as

characterizing only in a short time. Therefore, a prediction model for the long-term durability of shape memory polymers in the space environment was suggested based on the time-temperature superposition principle for the external environment.

In Chapter 3, a new 3D printing process for shape memory polymer was developed. In particular, a complex structure is required for use it as a space structure. To solve this problem, a 3D printing method of shape memory polymer was proposed. By synthesizing SMP capable of front polymerization, shape memory polymer could be printed. The 3D printing conditions were determined by analyzing the rheological properties and frontal polymerization velocity of SMP. Finally, free-standing SMP was printed and characterized.

In Chapter 4, a new 3D printing process was developed to print porous SMP to long-term durability. For this, core-shell nozzle was introduced to generate pore inside the polymer matrix. The porous structure was printed and structural properties were analyzed. In addition, the thermal/mechanical properties of the porous structure were analyzed. Finally, a shape memory polymer having a porous structure was printed in a free-standing structure and shape memory properties were characterized.

## **Chapter 2. Prediction of long-term properties of shape memory polymer/composite in a Low earth orbit**

Shape memory polymer/composites (SMPCs) are promising materials for space application. To extend the application field of SMPCs for aerospace, it is necessary to secure the durability of SMPCs in space environment. Accelerated test methods are commonly used to characterize the durability of SMPCs. Accelerated test methods are commonly used to predict long-term properties and durability. In short-duration experiments, accelerated tests are conducted under conditions that are harsher than those of the target environment to project long-term performance [79, 81-89]. In the LEO environment, there are factors such as ultraviolet radiation (UV), atomic oxygen (AO), and high vacuum that affect the polymer composite, and accelerated test for these factors are required. For example, changes in properties caused by electromagnetic waves, such as UV light, are predicted by examining the material's response to shorter wavelengths [90] and increasing temperature [91].

Generally, accelerated UV exposure tests are carried out using a short-wavelength UV light or by increasing the UV exposure duration [92-94]. However, these methods are ineffective, as various light sources must be prepared. There have also been some studies on the temperature dependence of UV degradation, but they were mostly conducted in the air atmospheric and low vacuum condition, meaning that

their results came from photo-degradation by oxygen [34, 94-97]. In the oxygen environment, the chain of the polymer was broken and oxidized easily by the UV exposure, resulting in the degraded mechanical properties. In AO tests, the AO flux is often increased artificially to predict durability [98].

The properties of polymer composites are highly dependent on time and temperature; thus, their long-term behavior can be predicted using the time-temperature superposition principle (TTSP). The TTSP provides the means to measure long-term behavior at a specific temperature, by carrying out experiments at a higher temperature and within a shorter time; with regard to polymer composites, molecular motions accelerate as the temperature of the polymer increases [34, 85, 86, 99-101]. In particular, measurement of long-term durability of polymer composites are expensive and time-consuming, temperature-frequency dependent dynamic mechanical model was used to minimize these issue [89, 91, 92]. Using this principle, many studies have been conducted to predict not only the viscoelastic properties of composite materials, but also the mechanical properties. Representatively, Miyano et al. [93, 102-105] conducted research to predict various long-term properties of polymers such as flexural strength, fatigue properties, and creep properties using TTSP.

The responsiveness of polymers to external stimuli increases with temperature. For example, the reactivity of materials to UV light exposure is more pronounced at higher temperatures, resulting in rapid degradation [105]. In addition, given the same source flow rate of argon and oxygen, the AO flux received by the polymer surface

increases with the exposure temperature, resulting in an acceleration effect [92]. These reports suggest that AO and UV effects can be accelerated by raising the exposure temperature.

In this chapter, the long-term properties of CF-SMPCs were investigated in a LEO environment, in which the TTSP was applied to characterize harsh high vacuum, UV light and AO exposure conditions under accelerated testing.

## **2.1. Experimental**

### **2.1.1. Materials and sample preparation**

A thermoset SMP was prepared using an epoxy resin (Epofix®; Struer, Denmark) and curing agent (Jeffamine D-230; Huntsman, USA) as a matrix for the carbon fiber composite. The resin and curing agent were mixed and stirred at 60 rpm. The epoxy mixture was defoamed in a vacuum oven for 1 h. Four layers of woven carbon fabric were used for reinforcement. CF-SMPCs were fabricated with a vacuum-assisted resin transfer molding (VARTM) method. Polymer composite specimens were cured at 110°C for 3 h, and removed from the mold used in the VARTM process. Then, specimens were further cured at 80°C for 2 h for shape stability and thermodynamically stability of switching segment, which play important role in shape memory mechanism. Experimental results can be influenced by the cure level of the SMPCs. Therefore, we prepared SMPCs with complete cure level by thermal

treatment. To check this, we carried out DSC analysis for specimens prepared using different curing schedules (Figure 2-1 and Table 2-1). The samples were heated from 0 to 200°C at a heating rate of 5°C /min while nitrogen gas was purged to maintain the inert environment. The exothermic peak in DSC thermogram was analyzed to determine the degree of curing. There was clearly an exothermic peak for uncured and partially cured specimens. However, the exothermic peak disappeared for the specimen prepared using fully cured condition. After that, we prepared all specimens used in this study using this curing condition. The fiber volume fraction of the CF-SMPC was 46%. The shape of the CF-SMPC samples was a rectangular parallelepiped having a length of 50 mm, a width of 6 mm and a thickness of 1 mm.

**Table 2-1** Curing schedule of the samples

Sample	Curing schedule
Uncured	X
Partially cured	50°C 2h
Fully cured	110°C 3h + 80°C 2h

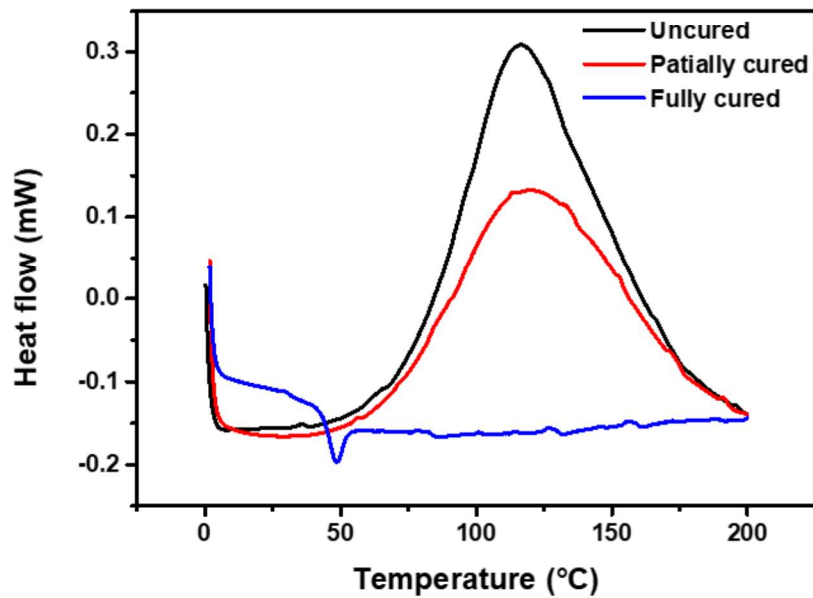


**Figure 2-1** DSC analysis of CF-SMPCs according to curing schedule

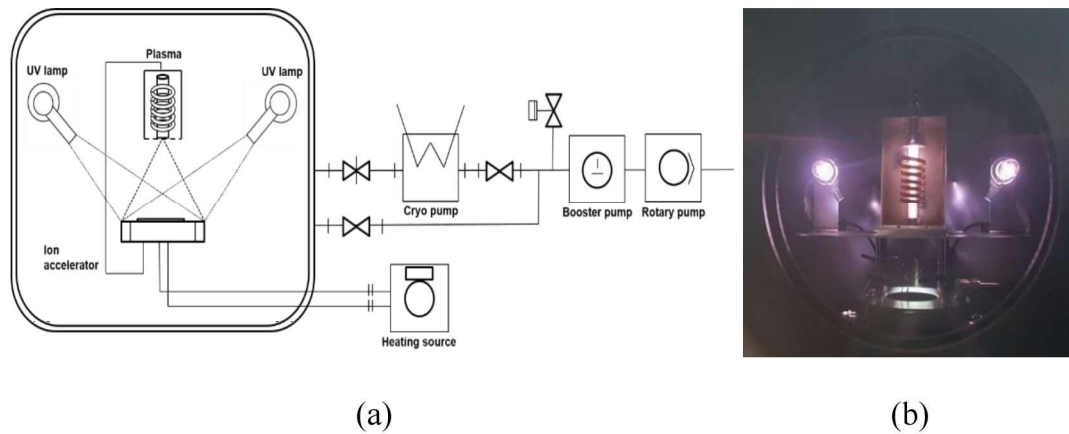
### 2.1.2. Environmental chamber and acceleration test

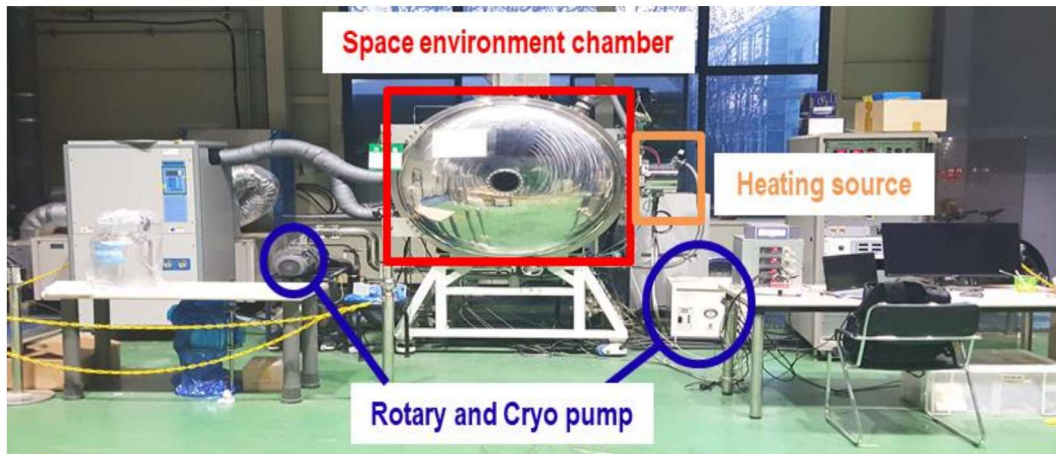
Figure 2-2 shows the LEO environmental chamber in our laboratory. The high vacuum system included a rotary pump and a cryogenic pump (Spacetorr, Suzuki Shokan, Japan). The system had a high vacuum atmosphere equivalent to about  $10^{-6}$  Torr. Deuterium lamps (L2D2 lamp, Hamamatsu, Japan) were used to generate UV radiation with a predominant wavelength range between 190 and 250 nm. Two UV lamps were installed on either side of the sample in the environmental chamber. The temperature of the sample was controlled by a heating source connected to the sample support. AO experiments used an inductively coupled plasma source, with an ion accelerator to provide a similar AO flux to all samples. AO was generated using Ar and O<sub>2</sub>, each with a flow rate of 0.8 cc/min, resulting in a plasma power of

0.612 mW. The AO flux in this environment was verified based on the ASTM-E2089 standard [92], in which the AO flux is predicted based on the mass change of the reference material (Kapton® HN; DuPont, Wilmington, DE, USA). The corresponding relationship is as follows:

$$f = \frac{\Delta M}{A\rho Et} \quad (1)$$

where  $f$  is the effective AO flux,  $\Delta M$  is the mass change of the reference materials,  $A$  is the exposed area,  $\rho$  is the density,  $E$  is the erosion yield, and  $t$  is the exposure duration. The AO flux was calculated based on the mass loss measured over a 21-h exposure period.





(c)

**Figure 2-2** Space environmental chamber: (a) schematic diagram, (b) built-in chamber, and (c) overall appearance

Accelerated tests in UV, AO and LEO environment were designed as follows. Acceleration tests were designed to consider the three factors affecting the durability of the polymer: time-temperature relaxation, UV and AO in high vacuum effects. The time-degradation acceleration test was based on the TTSP, in which the storage modulus of the SMPC was measured at various temperatures to obtain the acceleration/shift factor. To accelerate the effect of UV, AO and LEO exposure, SMPCs were exposed to each condition under vacuum at various temperatures for 21 h.

In general, the temperature range of the LEO space was  $-150^{\circ}\text{C}$  to  $150^{\circ}\text{C}$  [34]. In this range,  $70^{\circ}\text{C}$  was set as the reference temperature, as it resides within the transition region of the epoxy polymer composites. To confirm the acceleration effect of UV and AO on the CF-SMPCs, an environmental exposure test was conducted at

three temperatures: 70°C, 110°C, and 150°C. There is no specific standard condition for the exposure experiment of the LEO space. The test proceeded for 21 h. To create high vacuum conditions in the environmental chamber, 3 h was required; thus, a 21-h test was used for experimental convenience. In the case of LEO space, UV light and AO simultaneously affected the polymer composite material under high vacuum; for these experiments, the temperature was set to 70°C, 90°C, 110°C, 130°C, and 150°C. After each exposure test, shift factors were calculated using the TTSP to obtain a master curve for forecasting the long-term physical properties. In addition, to verify the acceleration test methodology, five new data sets having different times and exposure temperatures, but showing the same effect, were selected and compared.

### **2.1.3. Characterization**

The thermomechanical behavior of the polymer composite specimens was observed to confirm the influence of UV, AO and a LEO environment. The storage modulus and glass transition temperature ( $T_g$ ) were measured using a DMA Q800 system (TA Instruments, Inc., New Castle, DE, USA). Three-point bending measurements were conducted, using a span length of 20 mm and multi-frequency strain mode. The temperature range was from 30–150°C, the heating rate was 5°C/min, the frequency was 1 Hz, and the amplitude was 15  $\mu\text{m}$ . To quantify the acceleration effect, the samples were characterized with respect to the reference temperature of 70°C based

on the TTSP, over the frequency range of 1–25 Hz. An additional thermal analysis was performed using a simultaneous differential temperature analysis/thermogravimetric analysis (DTA/TGA; SDT650, TA Instruments) system. In a nitrogen atmosphere, the heating rate was 10°C/min, and the measurement temperature range was from 0 to 600°C. Surface analysis was carried out with secondary electron microscopy (JSM-7600F; JEOL, Ltd., Tokyo, Japan). Chemical analysis was performed using Fourier-transform infrared (FTIR) spectroscopy in attenuated total reflectance mode (Nicolet 6700; Nicolet Instrument Company/Thermo Fisher Scientific, Waltham, MA, USA).

Shape memory performance was characterized under three-point bending thermomechanical cyclic testing [95, 101]. First, the temperature was raised above the transition region to form a rubbery state, after which the specimen was deformed by 1.5% strain ( $\varepsilon_i \rightarrow \varepsilon_d$ ). After cooling to a temperature below the transition temperature, the deformation of the specimen was fixed by releasing external loads. Here, the shape fixity ratio ( $R_f$ ) was calculated by comparing the fixed strain with the initially imposed strain ( $\varepsilon_d \rightarrow \varepsilon_f$ ). Then, the temperature was raised above the transition temperature, allowing for strain recovery ( $\varepsilon_f \rightarrow \varepsilon_r$ ). The recovery ratio ( $R_r$ ) was calculated from the strain in the final recovered state, as follows:

$$R_f(\%) = \frac{\varepsilon_f}{\varepsilon_d} \times 100, \quad R_r(\%) = \frac{\varepsilon_d - \varepsilon_r}{\varepsilon_d} \times 100 \quad (2)$$

## **2.2. Effects of Ultraviolet radiation**

### **2.2.1. Effects of UV irradiation and exposure temperature**

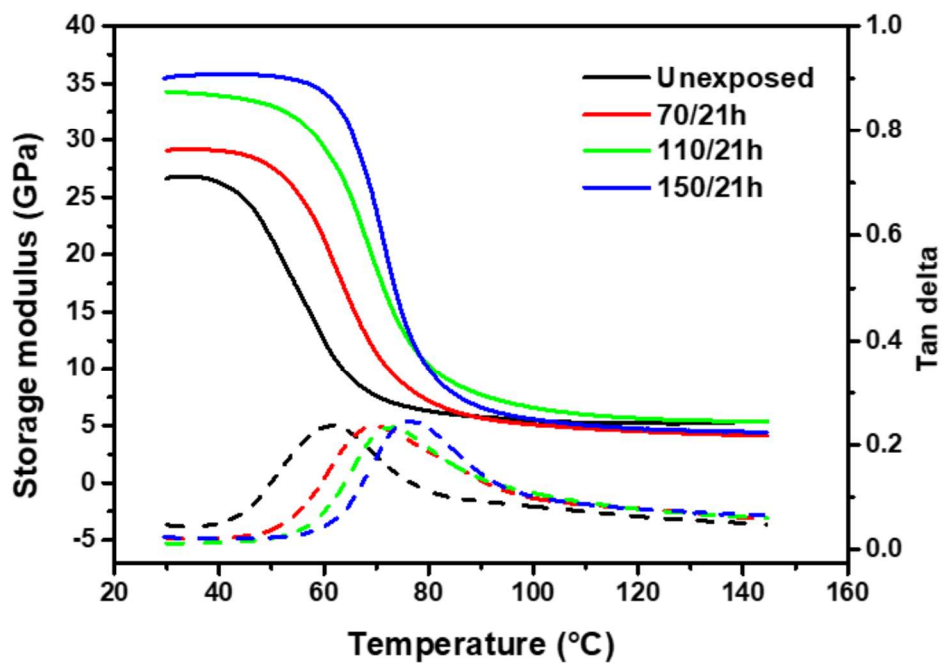
The glass transition temperature ( $T_g$ ) of CF-SMPC samples exposed to UV environments was measured by DMTA (Figure 2-3(a)). The storage modulus of unexposed CF-SMPCs decreased as the treatment temperature increased (Table 2-2).  $T_g$  and the storage modulus of the glassy region increased depending on the UV exposure temperature. Generally, molecular bonds can break under UV irradiation in air with photo-degradation occurring by reactions with ambient oxygen [34, 94, 101, 106, 107]. In this study, however, the opposite phenomenon was observed, in which the CF-SMPC samples hardened as they were exposed to UV. This phenomenon can be explained by post-curing behavior. Radicals generated in the CF-SMPC by UV irradiation did not form oxides under high vacuum, but instead, seemed to induce post-curing processes. We hypothesized that these processes accelerate at high temperatures, resulting in an increased crosslinking density and thus an increased  $T_g$  and the storage modulus. To test this, the crosslinking density of CF-SMPC samples was investigated using FTIR analysis (Figure 2-3(b)). For quantitative analysis, FTIR spectra were normalized based on the para-substituted benzene peak [98, 108]. Comparing the FTIR spectra before and after UV exposure, the position of the characteristic absorption peaks did not change. This means that the main functional groups did not change after UV exposure. However, the absorbance of peaks at 1,250, 1,509, and 1,296  $\text{cm}^{-1}$  tended to decrease as the sample

temperature during UV exposure increased. (Figure 2-3(c)) The absorbance peaks at 1,250 and 1,509  $\text{cm}^{-1}$  are attributed to the stretching and vibrational modes of the oxirane ring in the epoxy and N-H deformation of the polyamine crosslinking agent, respectively, while the peak at 1,296  $\text{cm}^{-1}$  is due to C-N stretching modes caused by chain scissoring [95, 109]. Changes in these peak intensities indicate that UV-induced radicals in the oxirane ring and the amine group form crosslinks between the epoxy and the hardener. Thus, the crosslinking of CF-SMPCs was promoted by UV irradiation under vacuum, and these effects were accelerated by the irradiation temperature.

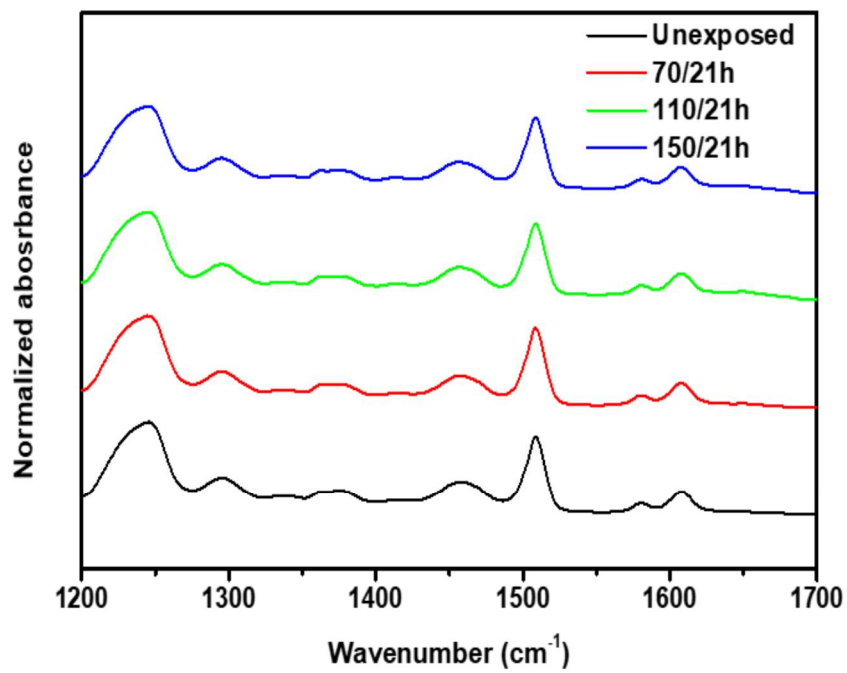
The surface morphologies of unexposed and UV-exposed CF-SMPCs were investigated using SEM. As shown in Figure 2-3(d), there were no significant differences in the surface morphologies of CF-SMPC samples exposed at 70°C, suggesting that UV-induced surface degradation rarely occurs in a vacuum environment. As the exposure temperature increased to 110°C and further to 150°C, small pieces of debris originating from the deterioration of the CF-SMPC surface by UV were observed. The type of degradation could easily affect the thermomechanical properties of SMPCs.

The mechanism of the crosslinking caused by UV exposure is different from that of the thermal curing which we used for sample preparation. The thermal curing for the sample preparation occurs by the reaction of epoxide ring and amine group by heat, whereas the crosslinking by UV exposure occurs when the radicals in main chains, including unreacted epoxide ring and amine group, generated by UV exposure are

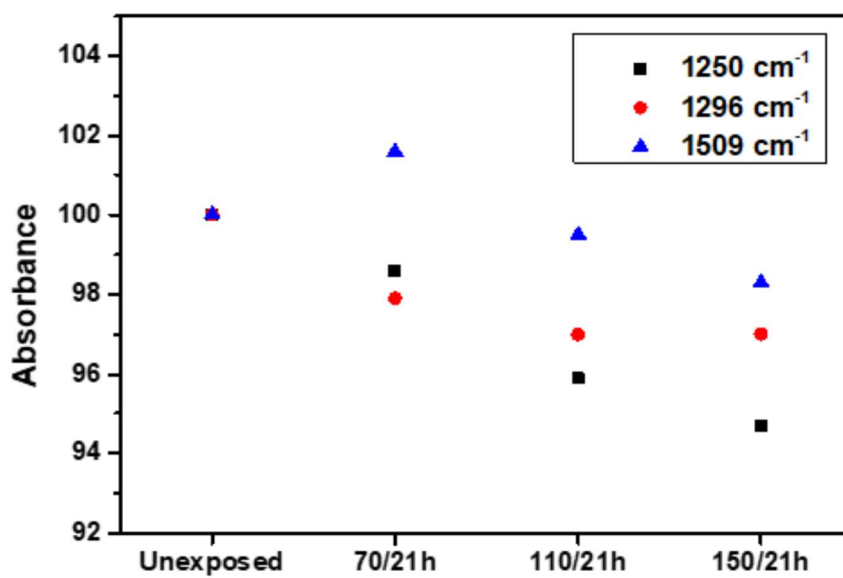
combined each other. As such, the relationship between the crosslinking and degradation in UV environment depends on exposure time. At the initial stage, the crosslinking is prominent. When the crosslinking is saturated, then the chain scissoring becomes prominent [110, 111] .



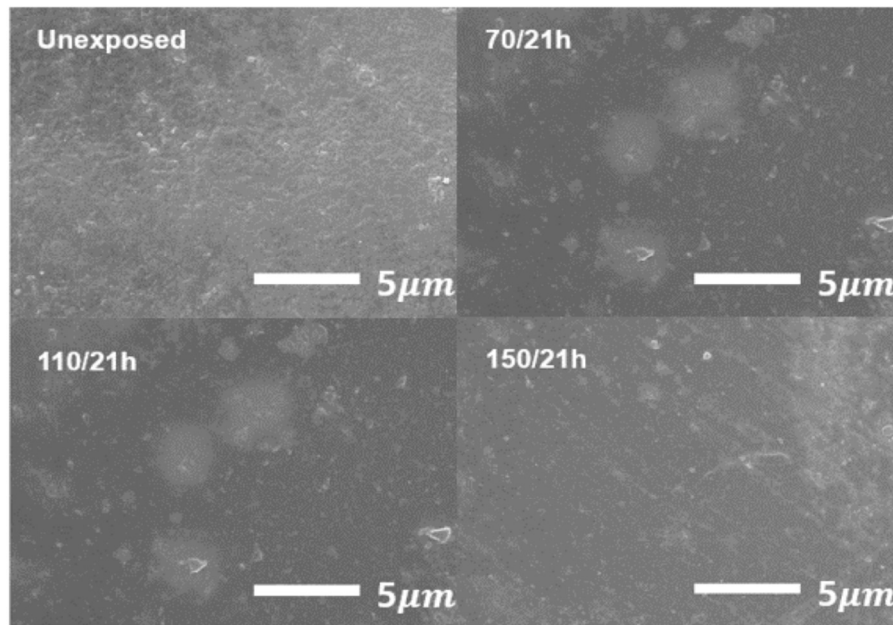
(a)



(b)



(c)



(d)

**Figure 2-3** Effects of VUV exposure on carbon fiber-reinforced shape memory epoxy/polymer composites (CF-SMPCs): (a) thermomechanical behavior (straight line – storage modulus, dash line – tangent delta), (b) FTIR spectra, (c) the absorbance changes in the characteristic peak, and (d) the surface morphology.

**Table 2-2.** Glass transition temperature of unexposed and UV-exposed SMPCs

VUV exposure	Abbreviation	Glass transition temperature (°C)
No treatment	U	68.0
70°C / 21 h	70/21h	69.7
110°C / 21 h	110/21h	71.4
150°C / 21 h	150/21h	74.6

SMPC: shape memory polymer composite, VUV: vacuum UV

### 2.2.2. Acceleration effects of time degradation by temperature

Long-term properties of polymeric materials can be predicted by the TTSP. In this study, the long-term properties of CF-SMPCs were investigated according to this principle. Figure 2-4(a) shows that the storage modulus of untreated CF-SMPCs decreased as a function of both temperature and time. These data were used to construct a master curve of the storage modulus at a reference temperature of 70°C. The storage modulus curves that had been measured at different temperatures were shifted along a log scale of time, such that the shifted curves overlapped the reference curve smoothly. Here, the shift factors shown in Figure 2-4(b) can be used to represent the distance moved along the log scale of time during superpositioning of the modulus curves. The CF-SMPC samples exhibited thermo-rheologically simple behavior, as shown in Figure 2-4(a), implying that all of the relaxation processes within the materials have the same temperature dependencies [98]. The temperature/time dependency of the storage modulus can be formulized by

$$G(t, T) = G^{ref} \left( \frac{t}{a_T(T)}, T^{ref} \right) \quad (3)$$

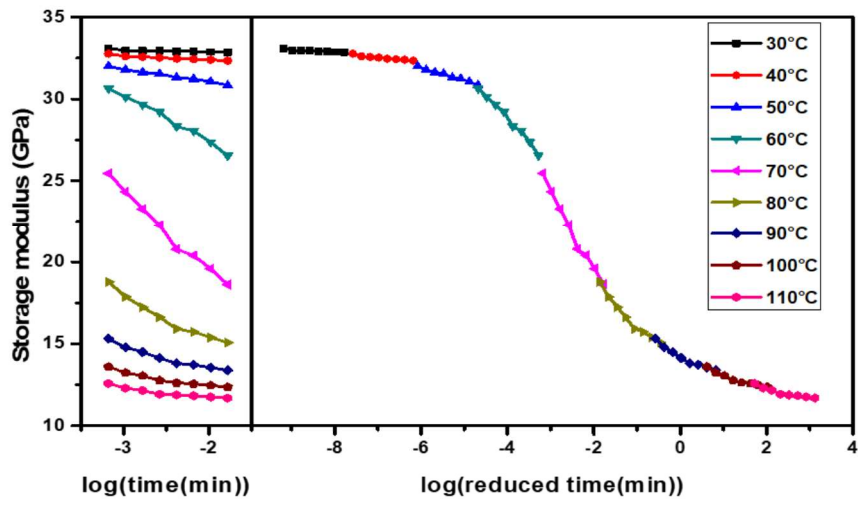
where  $G^{ref}$  is the storage modulus of the CF-SMPC sample at the reference temperature and  $a_T(T)$  is the shift factor. Note that shift factors are functions of temperature and can be formally expressed as

$$a_T(T) = \frac{t}{t'} \quad (4)$$

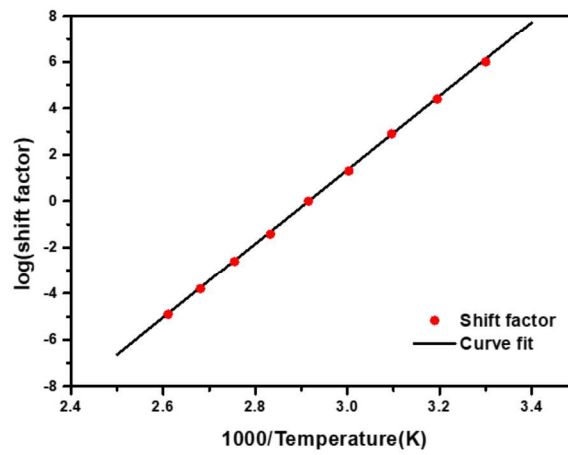
where  $t'$  is the reduced time. Shift factors are usually plotted by the WLF equation or the Arrhenius equation [92, 112-115]. Experimentally obtained shift factors were best plotted using the Arrhenius equation (see Figure 2-4(b))

$$\log a_T(T) = \frac{\Delta H_T}{2.303R} \left( \frac{1}{T} - \frac{1}{T^{ref}} \right) \quad (5)$$

where  $\Delta H_T$  is the activation energy of the material relaxation process (or degradation process in cases of reduced storage modulus) occurring in the CF-SMPC samples due to temperature, R is the gas constant, and  $T^{ref}$  is the reference temperature in absolute scale. The Arrhenius equation fitted well the glassy and rubbery regions, even though their activation energies were equal to 305.5 kJ/mol. Since the glassy and rubbery state showed the same activation energy, the fitting of the shift factor in the UV environment was carried out with the same activation energy for the glassy and rubbery state (Section 3.3). The long-term properties of the CF-SMPC samples were then predicted using the master curve and the shift factors, e.g., the storage modulus of SMPC samples at 70 °C, decreased from 14 GPa to 11 GPa over the time period from 0 to 103 min.



(a)

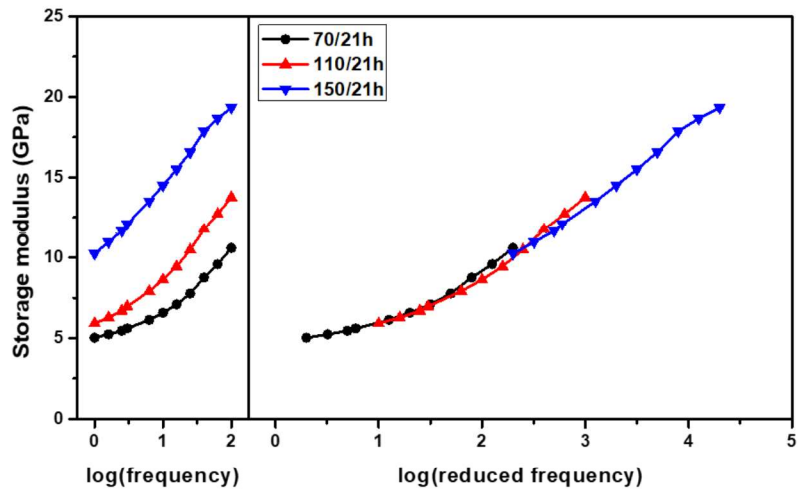


(b)

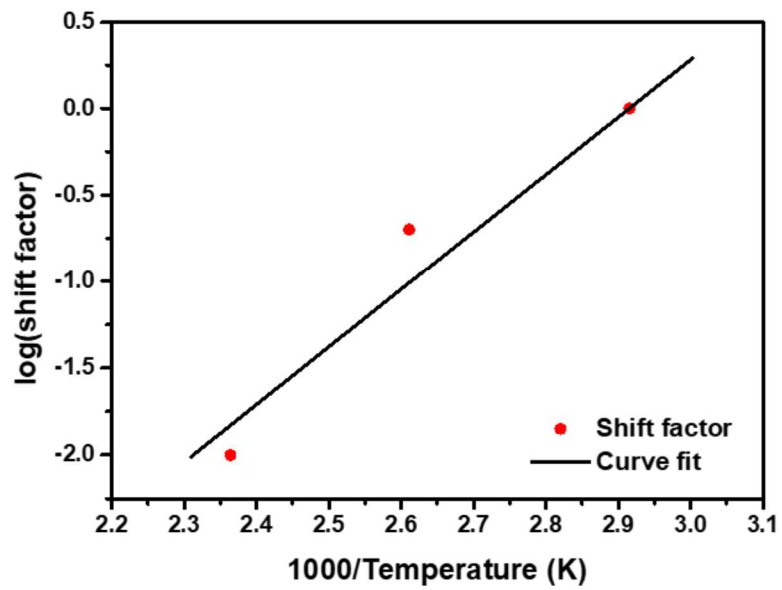
**Figure 2-4** (a) Storage modulus of unexposed CF-SMPCs as a function of temperature (left) and its master curve determined at 70°C (right), and (b) the corresponding shift factors used to build the master curve.

### **2.2.3. Quantitative analysis of the UV effects on long-term properties**

To investigate the effects of UV irradiation on the mechanical behavior of CF-SMPCs, samples were treated for 21 h at various temperatures (70, 110 and 150°C) in the UV environmental chamber. The storage modulus values of these UV-exposed samples were then measured as a function of frequency at a reference temperature of 70°C (Figure 2-5(a)); note that the reference temperature refers to the sample temperature during DMA testing. The storage modulus of the CF-SMPCs increased with the UV-exposed temperature. This was due to the effects of UV irradiation, as observed in Section 2.2.1, where the degree of crosslinking in the SMP matrix increased with the treatment temperature. It has been reported that outgassing of the polymer can occur in vacuum environments, resulting in the degradation of material properties [34]. However, this phenomenon was not dominant in the current study. The storage modulus of CF-SMPCs increased following UV exposure, indicating that the effects of UV-induced crosslinking were greater than those of polymer outgassing.



(a)



(b)

**Figure 2-5** Thermomechanical behavior of VUV-exposed SMPCs. (a) Storage moduli measured as a function of frequency at a reference temperature of 70°C (in DMA) and a master curve built at the reference temperature of 70°C (in the VUV chamber), and (b) shift factors for the master curve.

Interestingly, the storage modulus curves could be shifted and superimposed into a single, smooth curve (Figure 2-5(a)). The storage modulus curves of untreated CF-SMPCs obtained at different temperatures were also superimposed onto the master curve in Section 2.2.2. The data in Figure 2-5(a) suggest that, in addition to the time-temperature superposition of untreated CF-SMPCs in Section 2.2.2, the superpositioning of the duration of UV exposure and temperature can be described by

$$G(t, T^{VUV}) = G^{ref} \left( \frac{t}{a_{VUV}(T)}, T^{VUV,ref} \right) \quad (6)$$

where  $G^{ref}$  refers to the storage modulus of CF-SMPCs treated at the reference exposure temperature,  $T^{VUV,ref}$  is the reference exposure temperature (70°C),  $a_{VUV}(T)$  is the shift factor, and  $G(t, T^{VUV})$  is the predicted storage modulus of CF-SMPCs treated at the UV exposure temperature ( $T^{VUV}$ ). The activation energies of material processes (such as crosslinking and degradation) occurring during UV treatment can be obtained using the shift factors and the Arrhenius equation,

$$\log a_{VUV}(T) = \frac{\Delta H_{VUV}}{2.303R} \left( \frac{1}{T^{VUV}} - \frac{1}{T^{VUV,ref}} \right) \quad (7)$$

where  $\Delta H_{VUV}$  is the activation energy. The data in Fig. Figure 2-5(b) give an activation energy of 63.51 kJ/mol. The lower activation energy obtained above, relative to that of untreated CF-SMPCs, indicates that crosslinking and degradation during VUV treatment occurred more easily under the given conditions.

The meaning of this superposition can be determined by focusing on the nature of the UV irradiation. Considering particle-wave duality, a longer duration of UV exposure can be interpreted as an increased number of UV photons bombarding the materials. To impose the same effect over a shorter time frame would require energy input at a higher rate, in the form of a greater number of particles/photons or some other means. The effects of increased particle bombardment can be simulated by particle bombardment at a higher temperature. Figure 2-5(a) shows that UV exposure at high temperatures enhanced crosslinking, similar to the results achieved by increasing the UV intensity. We denote this as time–VUV–temperature superposition.

To validate this, four VUV-treatment temperature and time conditions (150°C/21h, 130°C/50h, 108°C/100h, 103°C/200h) were selected using the shift factor that would bring about the same VUV treatment effect; i.e., four specimens treated by these four conditions were expected to show the same mechanical behavior theoretically. T<sub>g</sub> and the storage modulus of these four specimens were measured. T<sub>g</sub> was measured at an average of 75°C, and the difference between each set was measured within 1.5°C (Table 2-3). The storage modulus values of all four specimens showed similar results, i.e., the average value of the storage modulus was 29.5 GPa. As a result, it can be claimed that the time-VUV-temperature superposition using the Arrhenius relationship is meaningful. Note that the time-VUV-temperature superposition does not take into account the degradation of CF-SMPCs over time as observed in Section 2.2.2.

**Table 2-3** Glass transition temperature and storage modulus of UV- exposed SMPC

with different treatment temperatures and times.

Sample	Abbreviation	Glass transition temperature (°C)	Storage modulus of glassy state (GPa)
150°C / 21 h	150/21h	74.6 (0.5)	29.93 (2.85)
130°C / 50 h	130/50h	76.3 (1.7)	27.83 (2.37)
108°C / 150 h	108/150h	75.0 (1.3)	27.43 (1.30)
103°C / 200 h	103/200h	74.5 (2.3)	32.53 (3.17)

To accurately predict the long-term properties of CF-SMPCs under VUV conditions, the two mechanisms, shown in Figure. 2-4 and 2-5, should be considered concurrently as follows. The storage modulus of CF-SMPCs decreased over time, as described by the master curve and the shift factors in Figure 2-4 (Section 2.2.2), which can be modeled by general time-temperature superposition. However, the UV environment brought about the opposite behavior, i.e., the storage modulus of CF-SMPCs decreased with UV-exposure time, as described in the master curve and shift factors shown in Figure 2-5. We describe these two phenomena in the TTSP and the time-UV-TTSP, respectively. In the current study, we suggest a prediction model of long-term mechanical properties of CF-SMPCs with long UV-exposure time by combining the two superposition principles as follows:

$$G(t, T, T^{VUV}) = G^{ref} \left( \frac{t}{a_T(T)a_{VUV}(T)}, T^{ref}, T^{VUV,ref} \right) \quad (8)$$

The variables in Eq. (8) are defined in Eqs. (3) through (7). Note that the combined

effects are described by the product of the shift factors obtained in Figures 2-4 and 2-5. The linear product of the shift factors, which describes more than two material processes, has been adopted to explain and numerically define the overall process. Yang et al. [92] suggested the time/curing dependency of relaxation times by applying the linear product of the time-temperature and time-conversion superposition principles. We also utilized this approach, although the two effects observed herein may not contribute equally to the mechanical behavior of CF-SMPCs.

The storage modulus of UV-exposed CF-SMPC samples was measured at various sample temperatures. These data were shifted and superimposed to create a single curve representing the storage modulus of UV-exposed CF-SMPCs at 70°C as a function of time, based on Eq (8) (Figure 2-6). The storage modulus of CF-SMPCs initially increased with UV exposure duration due to UV-induced crosslinking. When UV-induced crosslinking was saturated, the storage modulus decreased due to increasing contributions from relaxation phenomena and chain scissoring due to UV [85, 91]. Using this combined superposition principle, the mechanical behavior of CF-SMPCs exposed to a UV environment at 70°C can be predicted up to 1012 h. This method can be applied to predict the mechanical behavior of CF-SMPCs at higher temperatures under UV irradiation.

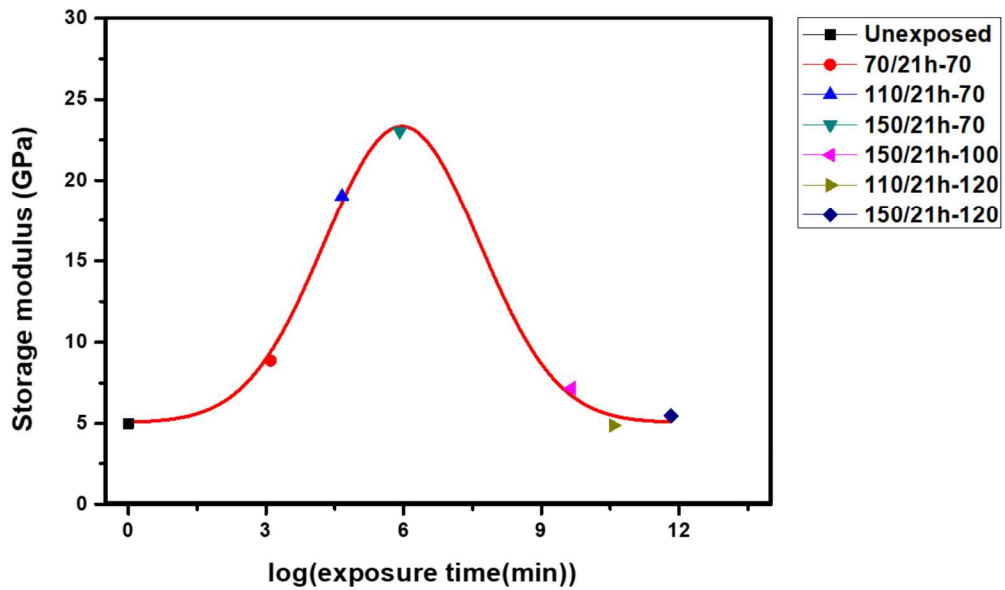


**Figure 2-6** Long-term variation in the storage modulus of CF-SMPCs when left at 70°C under VUV irradiation. Legends for each data point represent VUV-exposure conditions. The original data were subjected to shift operations.

## 2.3. Effects of atomic oxygen irradiation

### 2.3.1. Effects of AO irradiation and temperature on matrix erosion

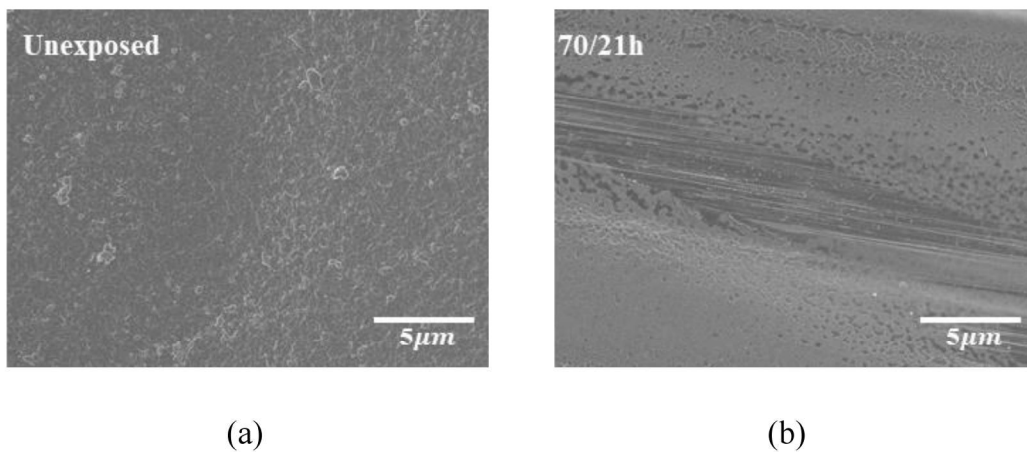
First, AO flux was characterized via the mass change of the reference material (Kapton® HN; erosion yield:  $2.81 \times 10^{-24}$  cm<sup>3</sup>/atom) based on ASTM-E2089 [34, 88]. Note that the erosion yield of the material represents the volume thereof that is eroded by incident oxygen atoms. The mass loss of the reference film increased with the exposure temperature in the AO environment. Based on the erosion yield of the film, the AO flux in the environmental chamber was determined with respect to the

exposure temperature (Table 2-4), showing the same order of AO flux as that of the space environment ( $10^{14}\sim 10^{15}$  atoms $\cdot$ cm $^{-2}$ /s) [33, 34].

**Table 2-4** Mass change of Kapton® HN film and atomic oxygen (AO) flux estimation.

Exposure temperature	70 °C	110 °C	150 °C
Mass change (g)	0.002	0.005	0.008
AO Flux (atoms/(cm $^2$ s))	$1.7 \times 10^{15}$	$4.1 \times 10^{15}$	$6.6 \times 10^{15}$
Erosion yield ( $E_y$ )	/	$2.81 \times 10^{-24}$	/

The surface morphology of AO-irradiated CF-SMPCs was observed, and erosion of the SMP matrix was confirmed (Figure 2-7). In addition, erosion accelerated as the exposure temperature increased, i.e., the matrix exhibited severe erosion at 150 °C, compared to samples exposed to 70°C and 110°C. This was reflected in the mass loss of the composites. The mass losses of CF-SMPCs were 0.5 %, 1 %, and 1.45 % at exposure temperatures of 70 °C, 110 °C, and 150 °C, respectively (Figure 2-8(a)).



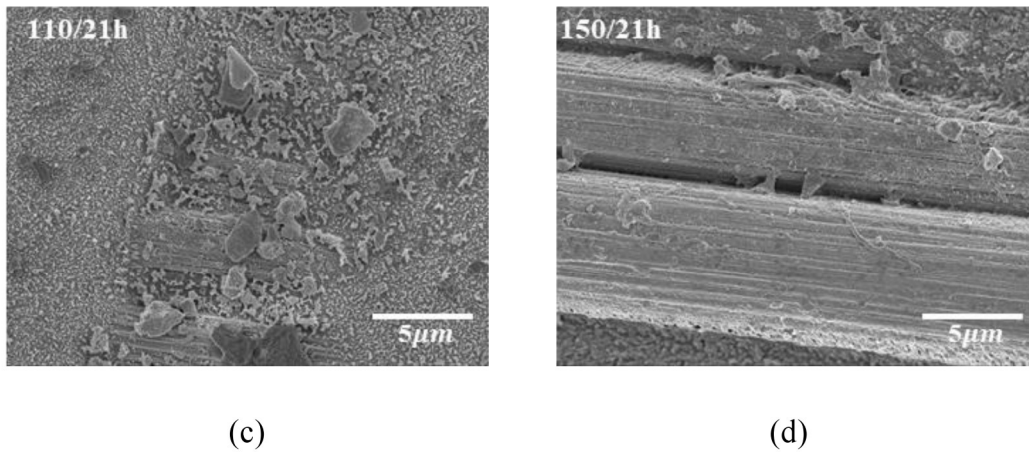


**Figure 2-7** Effects of atomic oxygen (AO) exposure on surface morphology of carbon fiber-reinforced shape memory polymer composites (CF-SMPCs) according to exposure temperature: (a) unexposed, (b) 70°C, (c) 110°C and (d) 150°C

The viscoelastic properties of CF-SMPCs before and after AO exposure were measured using dynamic mechanical thermal analysis (DMTA) (Figure 2-8(b), Table 2-5). The  $T_g$  of the unexposed sample was 70°C, and its storage modulus in the glassy region was about 30 GPa. As the exposure temperature increased,  $T_g$  increased, whereas the storage modulus decreased. In general, the interface between the fiber and matrix is weakened due to the effect of matrix erosion in an AO environment, resulting in degradation of the composite's mechanical properties [101, 116]. In our study, this phenomenon manifested in the storage modulus of the glassy region, in which the apparent degradation accelerated (from 30 to 22.75 GPa) as the exposure temperature increased. On the other hand, the  $T_g$  of CF-SMPCs increased due to AO exposure. This can be also explained, in part, by the matrix erosion of AO. Due to the erosion of the matrix, the weight fraction of the reinforcing material (i.e.,

CFs) increased, bringing about a higher  $T_g$ . The reinforcement itself does not contribute directly to the  $T_g$  change of the matrix; however, the interface between the polymer chain and fiber can significantly affect chain kinetics in the region around the fiber. Therefore, an increase in the weight fraction of reinforcement due to matrix erosion can cause an increase in  $T_g$  [33, 34]. Since the increase in  $T_g$  was too large to be explained solely by erosion of the matrix, a chemical analysis of the CF-SMPCs was performed.

Chemical changes in the CF-SMPCs according to the exposure temperature were observed before and after AO exposure using FTIR spectroscopy. When using bisphenol A-type epoxy and a diamine-based hardener, three characteristic peaks were observed. The peak at  $1250\text{ cm}^{-1}$  is related to the oxirane ring of the epoxy, the peak at  $1509\text{ cm}^{-1}$  is associated with the N-H deformation of polyamine, and that of  $1509\text{ cm}^{-1}$  corresponds to the C-N stretching vibration peak [101, 117]. There was no change in the main characteristic peaks, as shown in Figure 2-8(c), i.e., the functional group did not change after AO exposure. Whether there were chemical changes was inconclusive based on these results alone, as the chemical reactions between functional groups may not be detectable with FTIR spectroscopy [118].

TGA/DTA curves of CF-SMPCs were obtained (Figure 2-8(d)). The onset temperature of degradation was characterized according to ASTM E2550 to investigate the change in degree of crosslinking [119]. The onset temperature before AO exposure was  $344.98^\circ\text{C}$ ; this increased to  $351.67^\circ\text{C}$  for an exposure temperature

of 150°C (Table 2-5). These results suggest the possibility of post-curing by AO; in addition, the high energy of AO breaks the molecular chains inside the polymer, and the radicals generated create crosslinks [98]. This post-curing by AO exposure increased the  $T_g$  of the CF-SMPCs. In summary, AO causes erosion and post-curing of the SMP matrix, which are accelerated by the increased temperature of the AO exposure environment.

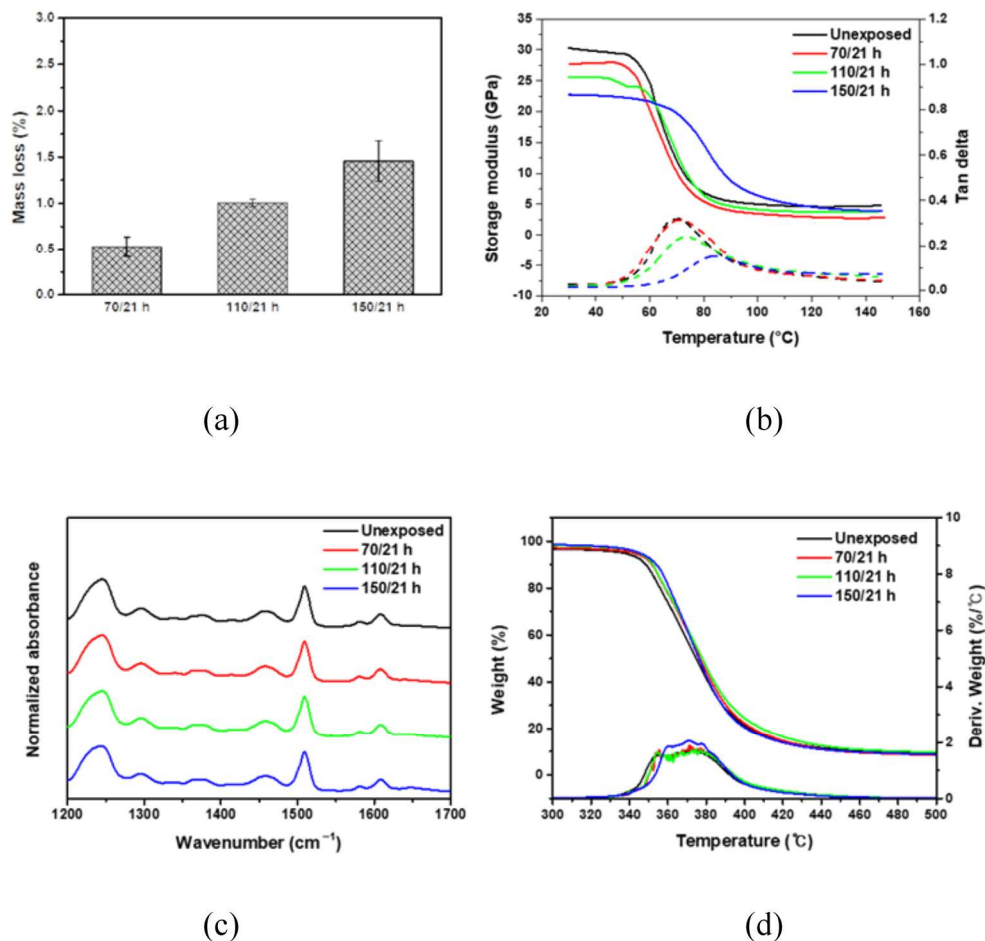


**Figure 2-8** Effects of atomic oxygen (AO) exposure on CF-SMPCs: (a) mass loss, (b) thermomechanical behavior (straight line—storage modulus, dashed line—tangent delta), (c) Fourier transform infrared (FT-IR) spectra and (d) thermogravimetric analysis/differential thermal analysis (TGA/DTA) data.

**Table 2-5** Thermomechanical properties and mass loss of AO-exposed carbon fiber-reinforced shape memory polymer composites (CF-SMPCs).

AO exposure	Glass transition temperature (°C)	Mass loss (%)	TGA onset temperature (°C)
No treatment	70.00	0	344.98
70°C / 21 h	71.00	0.525±(0.107)	349.82
110°C / 21 h	73.50	1.001±(0.040)	349.17
150°C / 21 h	84.00	1.454±(0.219)	351.67

### 2.3.2. Quantitative analysis of the AO effects on long-term properties

Given that the AO effect (matrix erosion and post-curing) accelerates as the temperature of the exposure environment increases, the TTSP, which is commonly used to analyze the long-term properties of polymeric materials, was applied to evaluate the long-term properties of CF-SMPCs exposed to a space environment. In this study, CF-SMPCs were exposed to a high vacuum and AO environment for 21 h at three temperatures (70°C, 110°C, and 150°C). The storage modulus of the CF-SMPCs was measured over the frequency range of 1–25 Hz at a reference temperature of 70°C (Figure 2-9(a)). In Figure 2-8(b), the storage modulus of AO-exposed CF-SMPCs decreased in glassy state, and the decrease was accelerated by exposure temperature mainly due to matrix erosion. In contrast, Figure 2-9(a) showed that the storage modulus increased according to exposure temperature. These can be explained by the glass transition temperature of the shape memory polymer

(SMP). The reference temperature (70°C), which is close to the glass transition temperature, was within temperature region where the phase of the SMP transits from the glassy state to the rubbery state. When the exposure temperature of AO increased, not only the matrix erosion but also the post-curing of the matrix due to the energy of the AO irradiation occurred, so the glassy state of the sample exposed to the AO became more dominant at the reference temperature than the unexposed sample. Therefore, despite the occurrence of matrix erosion, the storage modulus increased at the reference.

The long-term properties of CF-SMPCs can be predicted by the TTSP. By simple horizontal shifting the measured data as a function of exposure and time (frequency), a smooth master curve was obtained, from which shift factors could be determined according to the temperature of the AO environment (Figure 2-9(b)). This time/environment dependency is described by

$$G(t, T^{AO}) = G^{ref} \left( \frac{t}{a_{AO}(T)}, T^{AO,ref} \right) \quad (9)$$

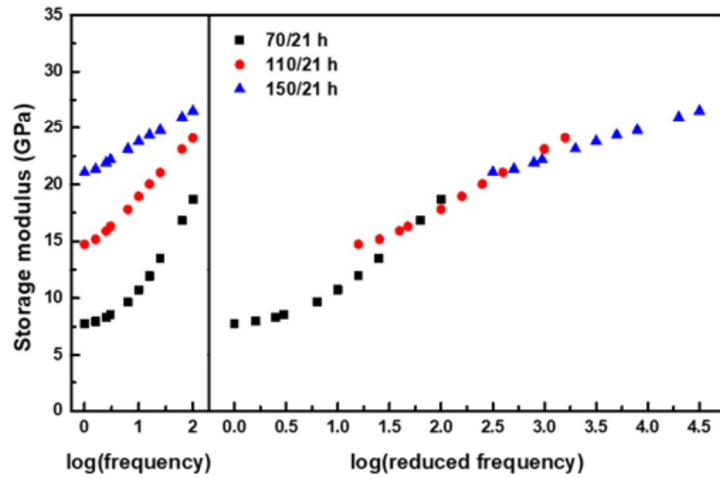
where  $G^{ref}$  refers to the storage modulus of CF-SMPCs exposed at the reference temperature,  $T^{AO,ref}$  is the reference exposure temperature (70°C),  $a_{AO}(T)$  is the shift factor at the exposure temperature, and  $G$  is the predicted storage modulus of CF-SMPCs at the exposure temperature. The shift factor is a quantitative index of how much acceleration has occurred in the actual experimental environment compared to the reference temperature. Experimentally obtained shift factors (Figure

4(b)) can be expressed using the Arrhenius equation [38, 112, 120].

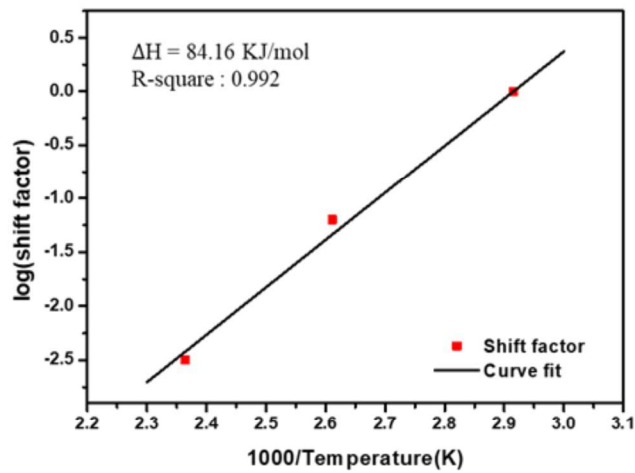
$$\log a_{AO}(T) = \frac{\Delta H_{T,AO}}{2.303R} \left( \frac{1}{T^{AO}} - \frac{1}{T^{AO,ref}} \right) \quad (10)$$

where  $\Delta H_{T,AO}$  is the activation energy. The activation energy of the AO process was 84.16 KJ/mol. This shift factor and TTSP were validated by carrying out additional experiments. Here, five conditions, 150°C/21 h, 139°C/50 h, 129°C/100 h, 124°C/150 h, and 120°C/200 h, were selected using the Arrhenius equation. After the exposure experiment with the selected conditions, the storage modulus and  $T_g$  of CF-SMPCs were measured through DMTA. Mass loss measurements and TGA/DTA analysis were conducted (Table 2-6). In this validation test, samples with different fiber orientations from those of acceleration tests (acceleration test: [0/90] orientation and validation test: [+45/-45] orientation) was used. Since the shift factor obtained in the previous acceleration test was mainly due to the post-curing of the polymer matrix, it was necessary to confirm whether this shift factor can be applied to different orientations with the same fiber volume fraction. For this reason, the storage modulus obtained from validation tests was lower than that from acceleration test and the glass transition temperature was also decreased, as reported in a literature [121]. It was confirmed that the prediction model based on acceleration test can be applied to polymer composite regardless of fiber orientation because there was no significant difference the five validation sets. The average  $T_g$  was 75.50°C, with a small deviation of about 0.79°C. In addition, the storage modulus of the glassy region, mass loss, and TGA onset temperature were somewhat similar, confirming the

validity of the shift factors and TTSP, as shown in Figure 2-9.



(a)



(b)

**Figure 2-9** Thermomechanical behavior of AO-exposed CF-SMPCs. (a) Storage moduli measured as a function of frequency at a reference temperature of 70 °C using dynamic mechanical thermal analysis (DMA) and the master curve built at the reference temperature of 70 °C, and (b) shift factors for the master curve.

**Table 2-6** Thermomechanical properties and mass loss for five validation data sets in an AO environment.

AO exposure	Glass transition temperature (°C)	Storage modulus of glass state (GPa)	Mass loss (%)	TGA onset temperature (°C)
150°C / 21 h	75.00	10.00	1.454	351.67
136°C / 50 h	76.50	10.25	1.119	352.19
124°C / 100 h	75.50	9.78	1.496	352.95
118°C / 150 h	76.00	11.39	1.394	351.65
113°C / 200 h	74.50	8.71	1.165	354.04
Average (Stdev)	75.50±(0.79)	10.03±(0.96)	1.330±(0.17)	352.50±(1.01)

To predict the long-term properties of CF-SMPCs in a high-vacuum AO environment, the effects of AO should be considered, along with degradation of the polymer due to the time-relaxation process. In addition to obtaining shift factors for accelerated relaxation of polymers over time, our group previously conducted similar tests in a UV environment, proposing a methodology to predict long-term properties based on the linear product of UV and time acceleration factors [45]. In this study, the same concept was utilized to predict the long-term properties of CF-SMPCs in the AO environment, based on the linear product of the shift factors for time-relaxation and AO effects:

$$G(t, T, T^{AO}) = G^{ref} \left( \frac{t}{a_T(T)a_{AO}(T)}, T^{ref}, T^{AO,ref} \right) \quad (11)$$

where  $a_T(T)$  is the shift factor of time degradation obtained from previous research. The storage modulus of AO-exposed CF-SMPC samples was measured at various temperatures (Figure 2-10). The storage modulus of AO-exposed CF-SMPCs

increased in the early stage due to the post-curing process. However, after post-curing saturation, the storage modulus decreased due to the erosion and time-relaxation phenomena of the polymer matrix.

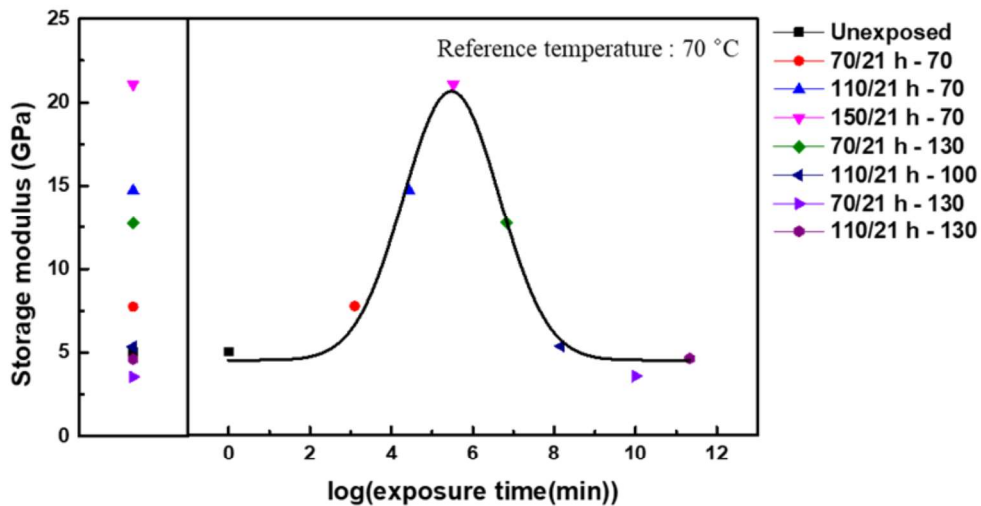


**Figure 2-10** Long-term variation in the storage modulus of CF-SMPCs when maintained at 70°C under AO irradiation. Legends for each data point represent the AO exposure conditions. The original data were subjected to shift operations.

## 2.4. Effects of a Low earth orbit environment

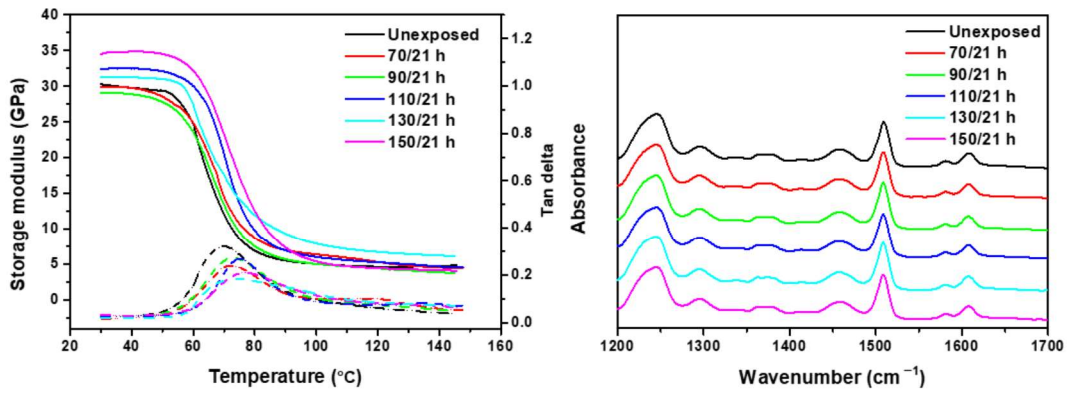
### 2.4.1. Quantitative analysis of long-term properties under LEO environment

Accelerated tests were also carried out in the LEO environment under AO and UV conditions. For more rigorous verification than in previous exposure tests conducted in AO environments, the temperature interval was set to 20°C and exposure tests were conducted at five temperatures (70°C, 90°C, 110°C, 130°C, and 150°C). The

other experimental conditions were the same as those used in the previous experiments.  $T_g$  increased, and the increase was more pronounced at higher temperatures (Figure 2-11(a)). However, the storage modulus tended to decrease in the AO environment. Notably, the opposite trend was observed in the LEO environment. This was because both UV and AO exposure resulted in the formation of radicals via the breaking of bonds in the polymer matrix, thereby causing post-curing to occur competitively. Thus, the matrix-eroding effect of AO was reduced. Both UV and AO promoted post-curing, which resulted in an increase in the storage modulus. The FTIR spectroscopy results also revealed no change in major peaks (Figure 2-11(b)), as in the AO environment, and post-curing was confirmed through TGA analysis (Figure 2-11(c)). Through these analyses, the  $T_g$  of the epoxy-based polymer composite became saturated around 75°C and did not increase further. Detailed experimental values are summarized in the Table 2-7

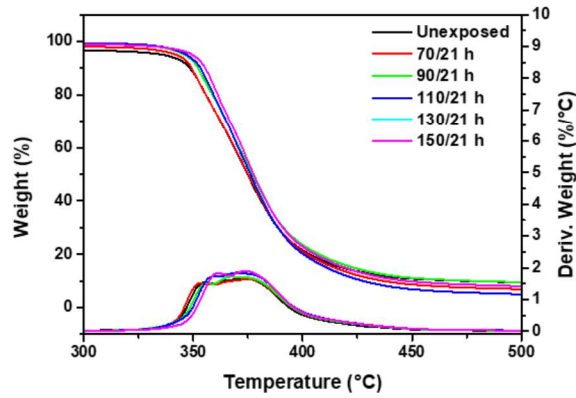
**Table 2-7** Thermomechanical properties of LEO-exposed CF-SMPCs

LEO exposure	Storage modulus of glassy state (GPa)	Glass transition temperature (°C)	TGA onset temperature (°C)
No treatment	30.32	70.00	344.98
70°C / 21 h	29.92	72.00	344.61
90°C / 21 h	29.11	73.00	347.74
110°C / 150 h	32.40	72.00	348.92
130°C / 200 h	31.25	74.00	347.13
150°C / 200 h	34.53	77.00	352.39



(a)

(b)



(c)

**Figure 2-11** Effects of LEO exposure on CF-SMPCs: (a) thermomechanical behavior, (b) FT-IR spectra, and (c) TGA/DTA curve of LEO-exposed CF-SMPCs.

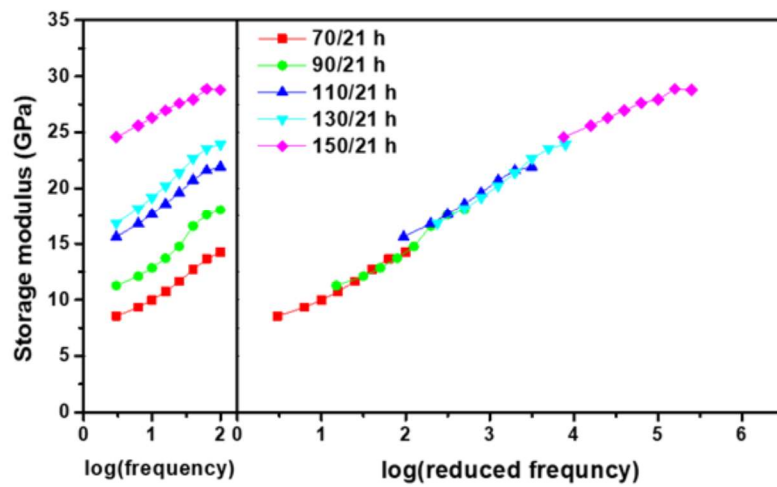
If there are two competing processes, non-linear Arrhenius behavior can be represented by modifying the coefficients such that two activation energies are considered [92, 105]. When such a competitive reaction occurs in an accelerated

experiment, a modified Arrhenius equation can be applied that introduces an additional term to represent temperature dependence [122]. In this study, to quantify the acceleration effect in the LEO environment wherein UV and AO are combined, the shift factors of UV and AO obtained through the simple Arrhenius equation were modified with additional coefficients for quantitative analysis. For the experimentally determined shift factor of the LEO environment, as in the previous method, CF-SMPCs were exposed to five temperatures in the LEO space, and the associated storage moduli were measured over the frequency range of 1–25 Hz for the given reference temperature (Figure 2-12(a)). A master curve was constructed through the horizontal shifting process of the measured storage modulus. The master curve of the LEO exposed CF-SMPCs showed similar outline to the master curve of the AO-exposed in Figure 2-9(a), but they represent different shift factors. Figure 4 showed a quantified shift factor to show how much the AO effect was accelerated by exposure temperature, while Figure 2-12 was a quantified shift factor for the acceleration of LEO environment by exposure temperature, which is the linear product of shift factors of UV and AO. As mentioned in Section 2.3.1, in the transition region, as the exposure temperature increased, the fraction of glass state increased and the storage modulus tended to increase. However, in the LEO environment, unlike in the AO environment, the acceleration effect on UV exposure was also included, so the calculated shift factors were different each other.

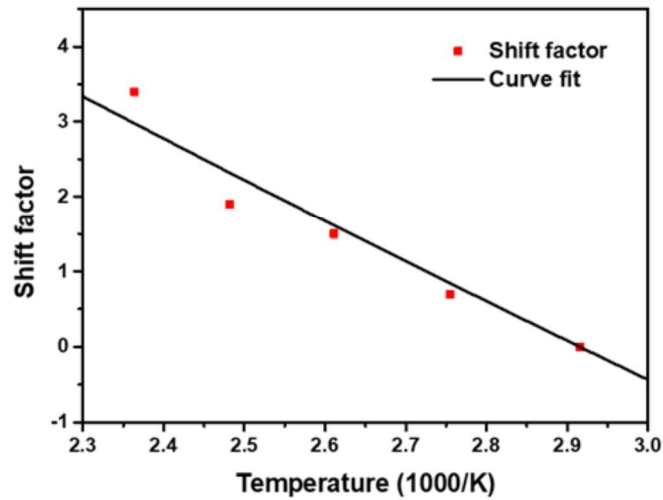
The shift factor obtained was analytically fit using the following equation (Figure 2-12(b)):

$$\log a_{LEO} = \alpha \log a_{UV} + \beta \log a_{AO} \quad (12)$$

where  $a_{UV}$  is the shift factor of the UV environment, which was obtained from our previous work [45], and  $\alpha$  and  $\beta$  are the coefficients representing the individual UV and AO processes, respectively. Validation was conducted by comparing five data sets (150°C/21 h, 139°C/50 h, 129°C/100 h, 124°C/150 h, 120°C/200 h) that were expected to show the same acceleration effects under different exposure times and temperatures. The measurement results are summarized in Table 2-8.  $T_g$ , the storage modulus, and the TGA onset temperature showed similar results, supporting the validity of Eq. (12).



(a)



(b)

**Figure 2-12** Thermomechanical behavior of LEO-exposed SMPCs. (a) Storage moduli measured as a function of frequency at a reference temperature of 70 °C (in DMA) and a master curve built at the reference temperature of 70 °C, and (b) shift factors for the master curve.

**Table 2-8** Thermomechanical properties for five validation datasets in a low-Earth orbit (LEO) environment

LEO exposure	Glass transition temperature (°C)	Storage modulus of glass state (GPa)	TGA onset temperature (°C)
150°C / 21 h	77.00	34.53	352.39
139°C / 50 h	78.50	33.50	352.80
129°C / 100 h	77.00	35.36	352.60
124°C / 150 h	75.50	34.77	352.58
120°C / 200 h	76.50	36.77	352.83
Average (Stdev)	76.90±(1.08)	34.99±(1.08)	352.64±(0.16)

The storage modulus of CF-SMPCs decreased over time, as described by the master curve and shift factors of time relaxation. However, the LEO environment, which included UV light and AO exposure, gave rise to other behavior, such as post-curing

and matrix erosion. We describe these three phenomena (time-temperature relaxation, UV and AO effects in high vacuum) as a linear product of the shift factors which considering them independently. In the current study, we created a prediction model to represent the long-term mechanical properties of CF-SMPCs with long LEO exposure times, by combining the three superposition principles as follows:

$$G(t, T, T^{LEO}) = G^{ref} \left( \frac{t}{a_T(T)a_{LEO}(T)}, T^{ref}, T^{LEO,ref} \right) \quad (13)$$

In the same manner as predicted in Section 2.3.2, a master curve was created by shifting the data with respect to the exposure temperature (Figure 2-13); a similar master curve is shown for the previous AO environment. The effect of increasing the exposure temperature emphasized the change in properties when the reactions are accompanied by post-curing in the transition region. After exposure, post-curing was dominant in the early part; however, in the second half of the curve, time-relaxation aging and AO-induced degradation were prominent.

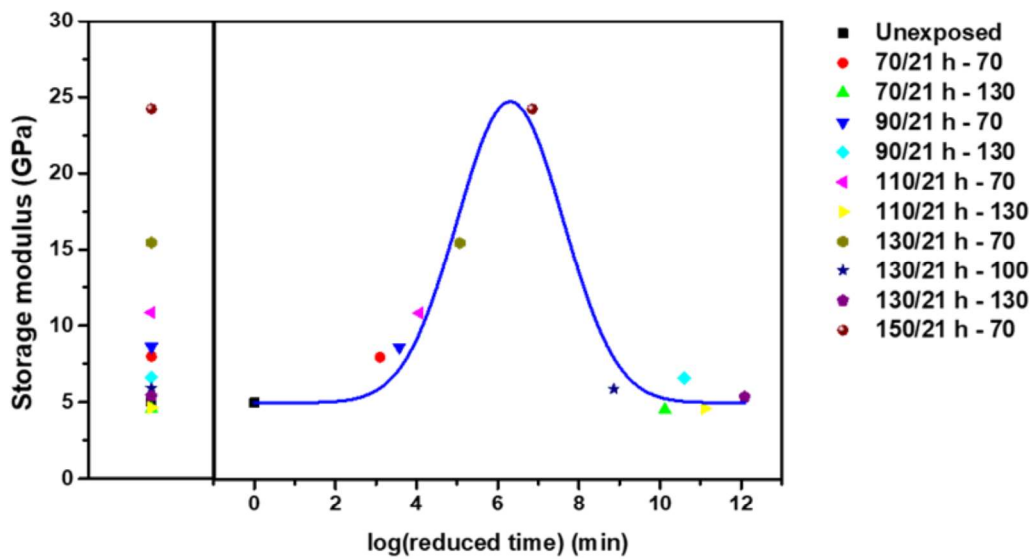


**Figure 2-13** Long-term variation in the storage modulus of CF-SMPCs when maintained at 70 °C under a LEO environment. Legends for each data point represent the LEO-exposure conditions. The original data were subjected to shift operations.

We obtained master curves for three environments (UV, AO, and LEO), considering previous research results. In previous our research, as in the AO and LEO environment, UV-induced crosslinking occurred under UV irradiation in high vacuum. The mechanism of this induced crosslinking was different from the thermal curing. In the thermal curing during specimen preparation, the reaction occurred between the epoxide group of main chain and the amine group of crosslink agent. However, UV-induced crosslinking was a newly formed crosslinking during exposure test through the reaction of radicals after chain scissoring by UV irradiation. It was confirmed in our previous work that in UV environment, the storage modulus

increased at the initial stage of exposure and then decreased [45].

In UV, AO, and LEO spaces, the storage modulus increased initially, and subsequently decreased at the reference temperature (Figure 2-14). However, there was a significant difference in the storage modulus value. In the case of AO, the initial properties increased due to post-curing; however, matrix erosion had only a small effect. The greatest effect was observed with UV exposure; notably, post-curing occurred without any AO effect. In the case of LEO space, the intermediate values between the AO and UV environments reflected the long-term properties under a UV environment.

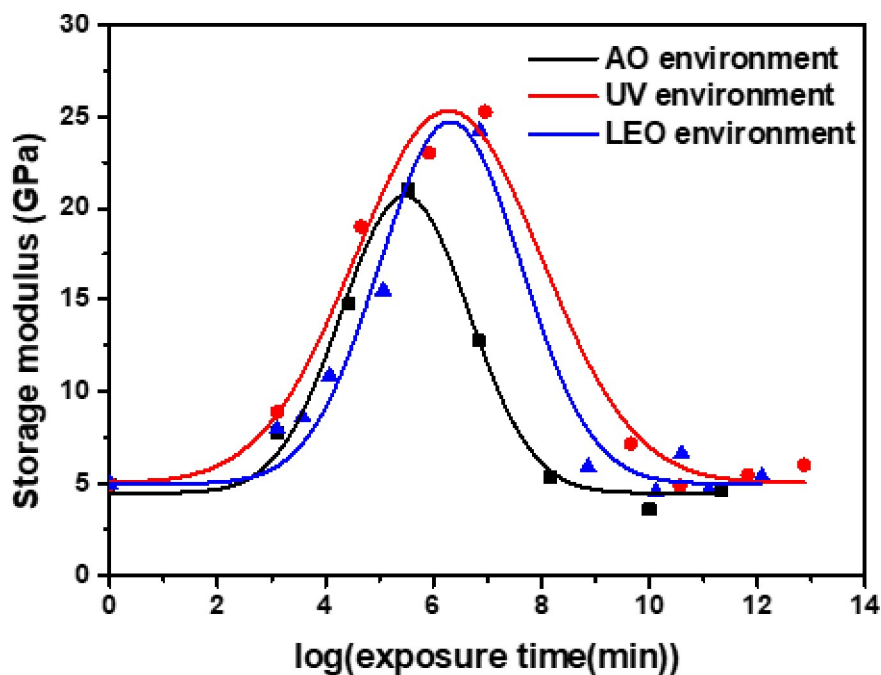


**Figure 2-14** Master curve for each environment (UV, AO and LEO exposure). Each data point represents an experimental value.

#### **2.4.2. Shape memory properties under UV/AO/LEO environment**

The shape memory performance of CF-SMPCs is important for their application to deployable structures in LEO environments. The shape memory properties of CF-SMPCs were characterized by two classical methods with DMA strain rate mode [45, 123, 124]. A general thermomechanical cyclic test was used to obtain the fixity and recovery ratio. It consisted of four steps: step 1) above the transition temperature (100°C), the sample was deformed by 1.5%, step 2) the deformed sample was then cooled down below the transition temperature at a cooling rate of 10°C/min maintaining the strain (i.e., to fix the shape), step 3) the sample was unloaded, and step 4) the strain was recovered under zero load condition as the temperature increased to 100°C at a heating rate 10°C/min (Fig. 7(a)). In addition, a constrained-strain recovery test was performed using the same procedure of the general thermomechanical cyclic test up to 2) step omitting step 3). In the step 4), the strain was fixed measuring the recovery stress (Figure 2-15).

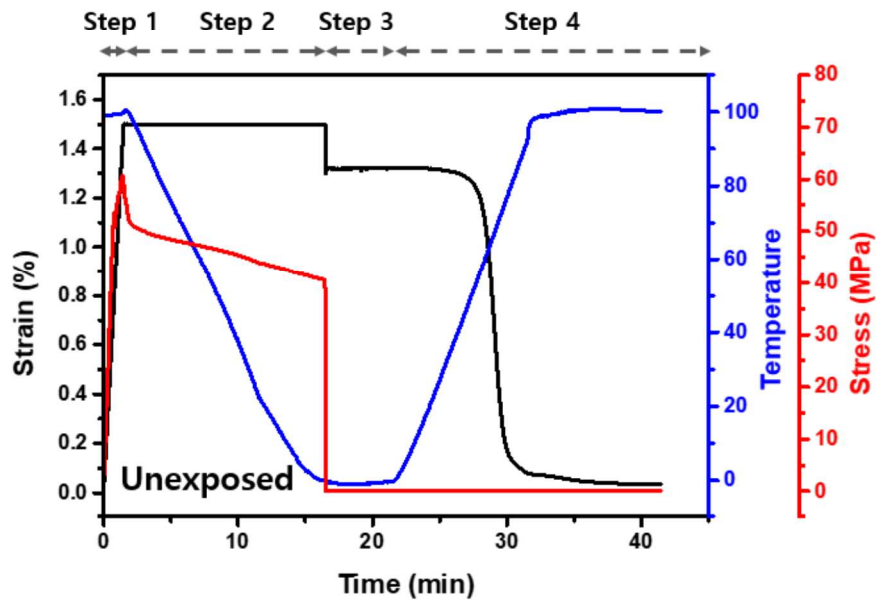


**Figure 2-15** Shape memory properties of unexposed-CF SMPCs (cyclic test)

**Table 2-9** Shape memory properties of unexposed and UV/AO/LEO-exposed CF-SMPCs

UV/AO/LEO - exposure	Fixity ratio (%)	Recovery ratio (%)
Unexposed	88±(0.01)	97±(0.01)
UV—70 °C / 21 h	89±(0.21)	98±(0.03)
UV—110 °C / 21 h	88±(0.47)	98±(0.45)
UV—150 °C / 21 h	88±(0.02)	97±(0.21)
AO—70 °C / 21 h	91±(0.56)	97±(1.42)
AO—110 °C / 21 h	88±(0.23)	96±(0.40)
AO—150 °C / 21 h	89±(0.89)	93±(0.83)
LEO—70 °C / 21 h	90±(0.42)	100±(0.50)
LEO—110 °C / 21 h	91±(0.04)	98±(0.08)
LEO—150 °C / 21 h	90±(0.06)	96±(0.01)

The shape memory properties of UV/AO/LEO exposed CF-SMPCs was summarized in Table 2-9. There was no significant change in shape memory performance before

and after exposure to the UV/AO/LEO environments. The fixity and recovery ratios were about 89% and 97%, respectively, indicating good shape memory behavior. Considering acceleration phenomena in the UV/AO/LEO environments, our results showed that the shape memory performance did not change significantly due to long-term exposure to the UV/AO/LEO environments. The shape memory performance of epoxy-based thermosetting SMPCs was determined based on the net points of the crosslinking structure and the flexible switching segments. In this epoxy-based material, the crosslink points act as a net point like an anchor, while the main chain of epoxy acts as a flexible switching segment. As such, the number of crosslink (i.e., net points) can determine the shape memory performance [99, 100]. In UV/AO/LEO spaces, post-curing of CF-SMPCs progressed and crosslinking increased; however, there was no further change in shape memory performance, as crosslinking had already occurred sufficiently. Note that, as confirmed in Section 2.2.1 and 2.3.1, the main functional group of the epoxy-amine-based SMP matrix did not change even after exposure to the AO and LEO environments, which can also explain the unchanged shape memory performance of CF-SMPCs.

## **2.5. Summary**

The thermomechanical properties of CF-SMPCs exposed to a LEO environment were characterized using a custom LEO environmental chamber designed to simulate high vacuum and UV and AO exposure conditions. These harsh conditions

brought about erosion and post-curing of the polymer matrix, which accelerated as the temperature of the LEO environment increased. The acceleration effect was quantified and modeled using the TTSP. Three shift factors for each acceleration effect (time–temperature relaxation, UV and AO effects in high vacuum) were obtained, and combined based on their linear products, to predict the long-term properties of CF-SMPCs. Finally, the effects of the LEO environment on the shape memory performance of CF-SMPCs were investigated; only slight effects were evident.

## **Chapter 3. 3D printing of shape memory polymers**

Several researchers have examined the 3D printing of SMPs using fused deposition modeling (FDM), stereolithography apparatus (SLA), and digital lighting processing (DLP) method methods [53-57]. FDM is based on the extrusion of thermoplastics and can be used to print thermoplastic SMPs into solid 3D objects [125-127]. In contrast, thermoset SMPs cannot be printed by FDM because they do not retain their structure prior to polymerization. Recently, the rheological properties of a thermoset resin were modified by incorporating reinforcing materials, such as nanoclay, to increase viscosity. However, after printing, this strategy requires a long post-curing period, ranging from 4 to 24 h [79, 81-83]. In addition, this method is not suitable for printing SMPs into geometrically complex shapes and free-standing forms. SLA and DLP printing techniques employ photocurable resins and layer-by-layer stacking of polymer resins [80]. However, the availability of photocurable SMPs is limited, and SLA and DLP processes require supporting frames, making them unsuitable for creating unsupported structures [82].

Recently, 3D printing has been realized using thermoset polymers in an FDM manner. In these processes, the extruded filament is polymerized immediately after exiting the nozzle and prior to collapse, thereby retaining its extruded shape in the 3D print [128]. This requires a monomer solution that is rheologically suitable for 3D printing.

Such systems feature oligomeric mixtures in a gel state. Radical-based frontal polymerization is then initiated by exposing the extruded gel to heat or light. Since the polymerization process is exothermic, the heat produced during initiation and subsequent polymerization catalyzes polymerization throughout the rest of the material [129]. This type of polymerization is called frontal polymerization. A schematic illustration of the frontal polymerization used in 3D printing was shown in Figure 3-1(a).

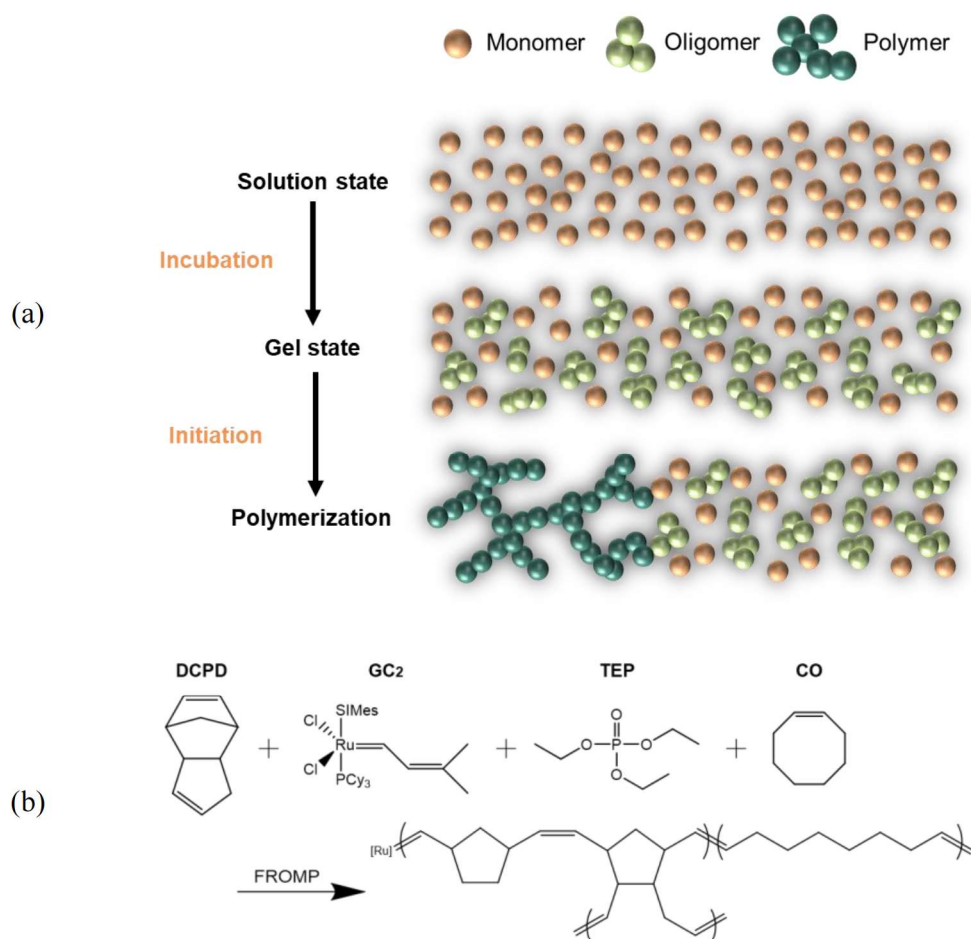


**Figure 3-1** (a) Schematic diagram of frontal polymerization and (b) polymerization mechanism and chemical structure of frontal SMP.

The polymerization is very fast and energy efficient. If the frontal polymerization is used for 3D printing, it is possible to 3D print a free-standing structure directly without any supporting materials because the 3D printed filament is polymerized and retains its shape before it collapses. The use of free-standing structure can increase the complexity of geometric shapes, which expanding the use of SMP.

In this chapter, a thermoset SMP capable of frontal polymerization was synthesized using dicyclopentadiene (DCPD) and cyclooctene (CO) with Grubbs' catalyst. Here, CO was co-polymerized with DCPD to impart the shape memory behavior (Figure 3-2(b)). Hereafter, this frontal polymerizable SMP is referred to as *fp*SMP. The thermodynamic and shape memory properties of the synthesized *fp*SMP were measured. In addition, the rheological properties and speed of frontal polymerization were evaluated to identify optimal conditions for 3D printing. Finally, a free-standing 3D structure was printed to demonstrate the printability and shape memory behavior of *fp*SMP.

## **3.1. Experimental**

### **3.1.1. Materials and sample preparation**

*fp*SMP was synthesized from DCPD, *cis*-CO, 5-ethylidene-2-norborene (ENB), second-generation Grubbs catalyst (GC2), phenylcyclohexane (PCH), and triethyl phosphate (TEP), all of which were purchased from Sigma-Aldrich and used as

received without further purification. Since DCPD is solid at room temperature, it was melted at 50°C after 5 wt% of ENB had been added to lower the melting point. A CO solution was prepared separately and 0, 0.15, or 0.3 molar equivalents of DCPD were added to the DCPD solution. The mixture was then mixed for 5 min at 2,000 rpm in a planetary centrifugal mixer (ARE-310; Thinky Corporation, Japan). For the catalyst solution, GC2, in an amount corresponding to 100 ppm of the DCPD/CO solution, was mixed with 100 molar equivalents of PCH and TEP (phosphate inhibitor) for 5 min at 2,000 rpm in a planetary centrifugal mixer. Finally, the DCPD/CO and catalyst solutions were mixed for 1 min at 2,000 rpm in the planetary centrifugal mixer and degassed at 2,200 rpm for 1 min. This final solution was used as the extrusion medium, or ink, for 3D printing.

### **3.1.2. Characterization**

#### **3.1.2.1. Thermomechanical and shape memory properties**

Thermal analyses were used to confirm synthesis of the DCPD/CO copolymer. Samples were heated at 10°C/min in a nitrogen atmosphere from room temperature to 600°C in a thermogravimetric analyzer (TGA; Discovery TGA; TA Instruments, USA). The thermomechanical properties and shape memory performance of *fp*SMP were measured with a dynamic mechanical analyzer (DMA; DMA Q800; TA Instruments). All properties were measured in tensile mode. The thermomechanical properties [glass transition temperature ( $T_g$ ) and storage modulus] of each sample

were also measured from 0°C to 150°C at a heating rate of 5°C/min and frequency of 1 Hz through a multifrequency-strain module.

The shape memory performance of *fp*SMP was determined using a common one-dimensional characterization method [42, 130] and a DMA strain module. Samples were deformed at a temperature above  $T_g$  (100°C) [strain:  $\varepsilon_d$ (10%)]. While maintaining the deformation, the sample was cooled to below  $T_g$  (25°C). The external force was then removed and the deformed, i.e., temporary, shape was fixed, corresponding to the  $\varepsilon_d \rightarrow \varepsilon_f$  transition. The temperature was then raised above  $T_g$ , allowing the deformed shape to recover its original form, i.e., the  $\varepsilon_f \rightarrow \varepsilon_r$  transition. The recovery ratio ( $R_r$ ) can be calculated according to the final shape as follows:

$$R_f(\%) = \frac{\varepsilon_f}{\varepsilon_d} \times 100 \quad R_r(\%) = \frac{\varepsilon_d - \varepsilon_r}{\varepsilon_d} \times 100$$

where ( $R_f$ ) corresponds to the fixity ratio.

### 3.1.2.2. Measurement of rheological properties and frontal velocities

The rheological properties of the ink were measured as a function of incubation time at 25°C with an AR2000 rheometer (TA Instruments). Tests were conducted using a 20 mm, 1° steel extrusion cone at a frequency of 1 Hz and strain of 0.1% at 25°C. The ink was incubated at 25°C to ensure that its rheological properties were suitable for 3D printing. The ink was then placed in a syringe of the 3D printing system and

its behavior was observed as a function of incubation time while extruding at a rate of 0.147 mL/min.

To measure the velocity of frontal polymerization, the ink was fed into a cylinder with an inner diameter of 6.5 mm and length of 72 mm. The ink was heated locally using a soldering iron and temperature changes in the ink were observed as a function of time using an infrared (IR) camera (FLIR A320; FLIR Systems, USA).

### **3.1.3. 3D printing process for shape memory polymer**

To 3D print our synthesized *fp*SMP, the ink was placed into a 6-mL syringe and incubated at 25°C. The syringe was then placed in a cooling chamber (-5°C) to delay the rate of gelation. The printing head was installed into the 3D plotter of a 3D printer (Pinter 300; Samdimall Co., Republic of Korea). Ink was extruded from the printing head onto the build plate at a constant rate. Heat from a soldering iron, positioned 10 mm from the end of the nozzle, initiated frontal polymerization to fix the shape of the printed product.

## **3.2. 3D printing of frontal polymerized shape memory polymer**

### 3.2.1. Thermomechanical and shape memory properties

DCPD is a representative monomer of thermoset plastics that can be polymerized through ring-opening metathesis polymerization (ROMP). A typical ruthenium-based catalyst (Grubbs catalyst) is used for this reaction. Applying a thermal stimulus initiates a self-propagating polymerization [128]. In contrast, CO is a representative monomer of thermoplastics and can undergo ROMP using a ruthenium catalyst [131, 132]. Therefore, the polymerization of DCPD and CO can occur simultaneously to afford a copolymer, referred to herein as *fpSMP*.

Thermogravimetric analyses were used to assess the thermal stability of the synthesized *fpSMP* as a function of CO content (Figure 3-2). As the molar equivalent of CO increased, the copolymer began to decompose at lower temperatures. This was attributed to the linear chain structure of polymerized CO, which is more vulnerable to temperature [133].

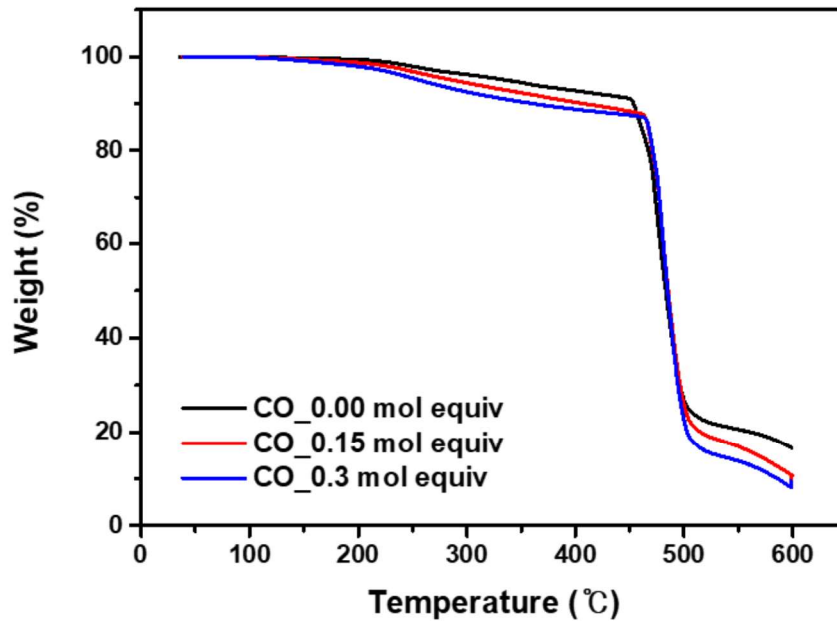


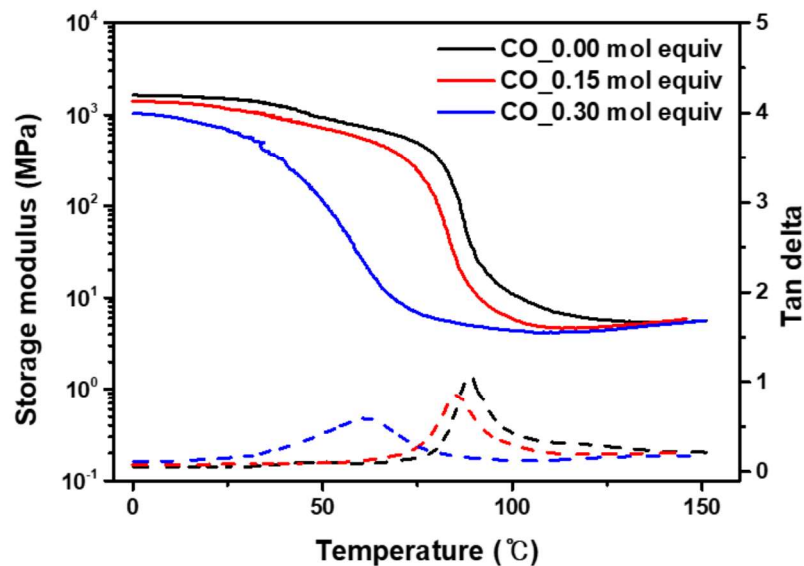
**Figure 3-2** TGA analysis of *fpSMP* according to CO content.

This trend was also evident in the thermomechanical behavior of *fpSMP*, as shown in Figure 3-3(a). Storage modulus decreased as the amount of CO increased, and the  $T_g$  decreased by 27°C from 88°C to 61°C. As the proportion of polymerized CO, which is a linear polymer, increased, the flexibility of the polymer chain increased, resulting in a decrease in  $T_g$  [134, 135].

The shape memory performance of *fpSMP* was also measured (Figure 3-3(b)) as a function of CO content (Table.3-1). While the fixity ratio was not significantly affected by the proportion of CO, the recovery ratio was greatly affected. In general, shape memory behavior is determined by the proportions of hard polymeric segments, such as those resulting from physical entanglement and crosslinking, and

switching segments such as flexible linear chains. The hard segments serve as anchors and maintain the deformed state when the shape is fixed. In contrast, switching segments allow the polymer to be more easily deformed, and to recover its original shape [1]. Increasing the proportion of CO therefore increased the proportion of switching segments and had a strong effect on the recovery process. Shape recovery increased with increasing CO. In addition, less stress was required to deform the structure with increasing proportions of CO.

(a)



(b)

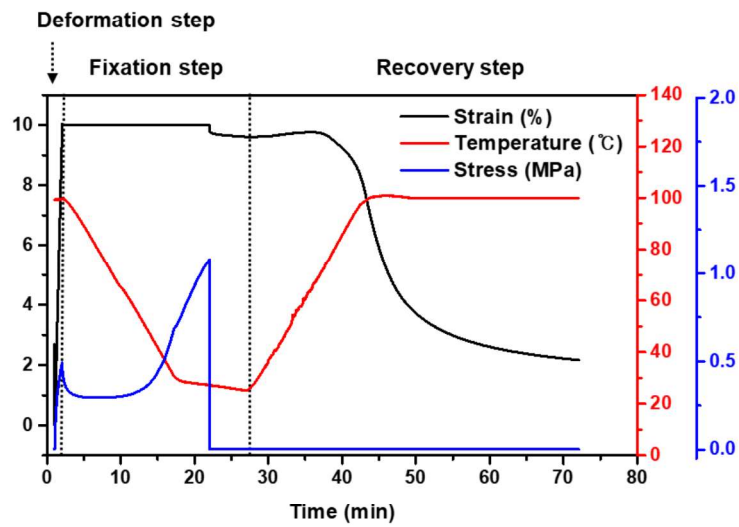


**Figure 3-3** (a) Thermomechanical behavior of *fpSMP* according to CO content (straight line - storage modulus, dash line - tan delta) and (b) shape memory behavior is shown for a formulation containing 0.15 molar equivalents of CO.

**Table 3-1** Thermomechanical and shape memory properties of *fpSMP*.

CO mol equiv	Storage modulus of glassy state (GPa)	Glass transition temperature (°C)	Fixity ratio (%)	Recovery ratio (%)	Maximum stress (MPa)
CO 0	1641.81	88.41	95.92	63.54	1.54
CO 0.15	1407.44	85.20	96.13	78.36	1.08
CO 0.3	1017.59	61.72	94.14	89.30	0.50

Considering these results, *fpSMP* having a 0.15 molar equivalent of CO was selected as the optimal 3D printing ink. Compared with other blends, this composition did

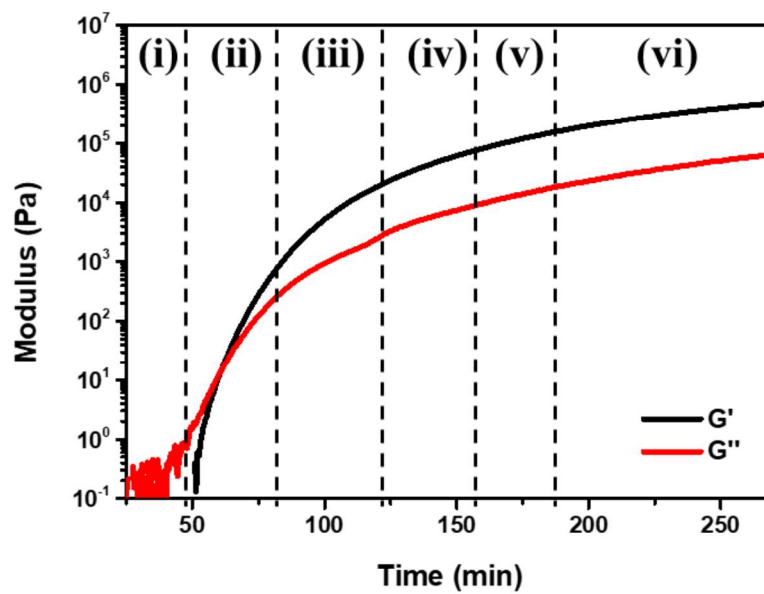
not degrade mechanically, and exhibited satisfactory fixity and recovery ratio. can be confirmed that less stress was required to deform due to the structure of CO.

### **3.2.2. Rheological properties and frontal velocity**

The rheological properties of the ink were used to gauge printability. Figure 3-4 shows the storage and loss moduli as a function of incubation time (Figure 3-4(a)), and the appearance of the printed ink (Figure 3-4(b)). When the storage modulus was smaller than the loss modulus, *i.e.*, under low viscosity conditions, the ink formed droplets (region (i)). In region (ii), where the storage modulus was close to the loss modulus, *i.e.*, near the gel point, gelation resulting in a stream line. In regions (iii) and (iv), increasing viscosity of the ink resulted in thicker extrusions and the printed ink tended to pile up on the build plate. However, in these regions, the printed structure had fused and fallen. Thus, while 3D printing in these regions was possible as long as frontal polymerization occurred before the printed structure fell or collapsed, free-standing structures could not be printed. In region (v), the storage modulus increased to a  $10^4\sim 10^5$  Pa. The printed ink was deposited onto the build plate and maintained its shape; the newly printed filaments were fused with the surface of the previously printed filament. However, in region (vi), while the printed ink maintained its shape, subsequent layers did not fuse with the preceding layers. With further incubation, the printing head was not able to extrude the ink. These data indicate that 3D printing of *fp*SMP is possible with incubation times of 165–200 min,

corresponding to regions (v) and (vi).

(a)



(b)

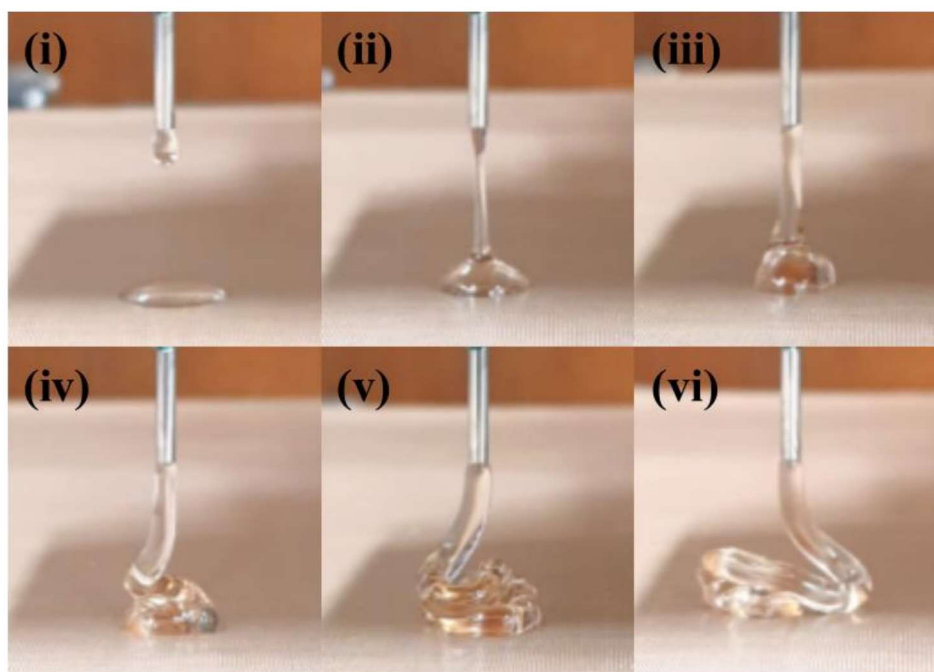


**Figure 3-4** (a) Rheological properties of *fpSMP* and (b) the appearance of extruded filaments at each state

During printing, the distance between the end of the print nozzle and the frontal polymerization line was held at 10 mm. Therefore, to print a free-standing structure, the extruded filament needs to maintain its shape over 10 mm without any support. Smay et al. [136] applied Euler-Bernoulli beam theory to calculate the effective homogeneous shear modulus ( $G'_{\text{eff}}$ ) required for a gel ink to be printed with cylindrical spanning filaments.  $G'_{\text{eff}}$  is defined by the shear modulus of deflection, the magnitude of which is less than 5% of the diameter of the filament at the center point of the span.  $G'_{\text{eff}}$  can be calculated as follows,

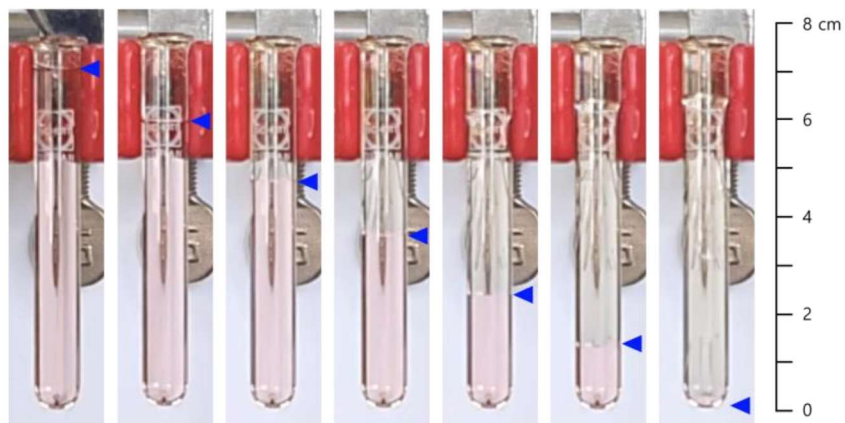
$$G'_{\text{eff}} \geq \frac{1.4\rho gL^4}{D^3}$$

where  $\rho$  is the density of the gel,  $g$  is gravitational acceleration,  $L$  is the span distance, and  $D$  is the diameter of the filament. In this study, the span distance, *i.e.*, the distance between the nozzle and frontal polymerization line, was 10 mm. The diameter of the filament was 2.5 mm and the density of the gel was 0.390 g/cm<sup>3</sup>. Equation (1) dictates that  $G'_{\text{eff}}$  should be at least 9,226 Pa. The incubation time to attain this  $G'_{\text{eff}}$  was 183 min and 3D printing was possible for up to 225 min using a cooling chamber to delay gelation.

To determine the optimal print speed, the frontal polymerization velocity was measured as shown in Figure 3-5. Figure 3-5(a) shows frontal polymerization of ink that had been incubated for 30 min (indicated by blue arrows). When heat was applied locally, polymerization initiated in that area and generated additional heat

via exothermic polymerization. The generated heat transferred to adjacent monomers, spreading the polymerization reaction through the printed solid. Changes in temperature were confirmed by IR images, as shown in Figure 3-5(b). This process continued until all of the available monomers in the material had been polymerized. As the “line” of frontal polymerization advanced, the temperature of the ink increased to 90°C, and the heat from polymerization propagated. The frontal polymerization velocity was defined by the speed of the advancing edge and was obtained as a function of incubation time. The data in Figure 3-5(c) show that frontal velocity tended to decrease with increasing incubation time, reaching 3 cm/min in regions where 3D printing is possible. Accordingly, 3 cm/min was deemed the optimal print speed in accordance with the frontal polymerization velocity.

(a)



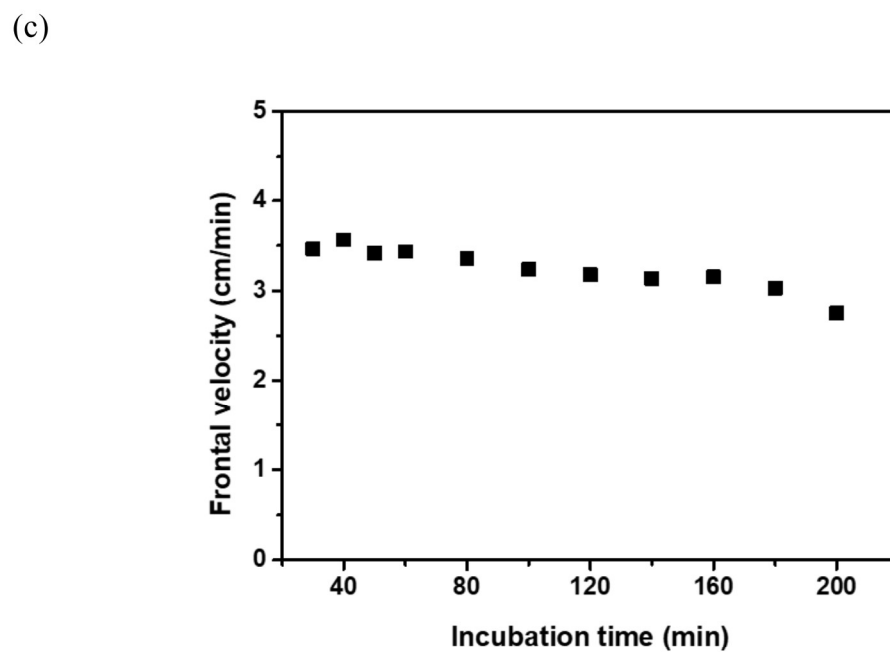
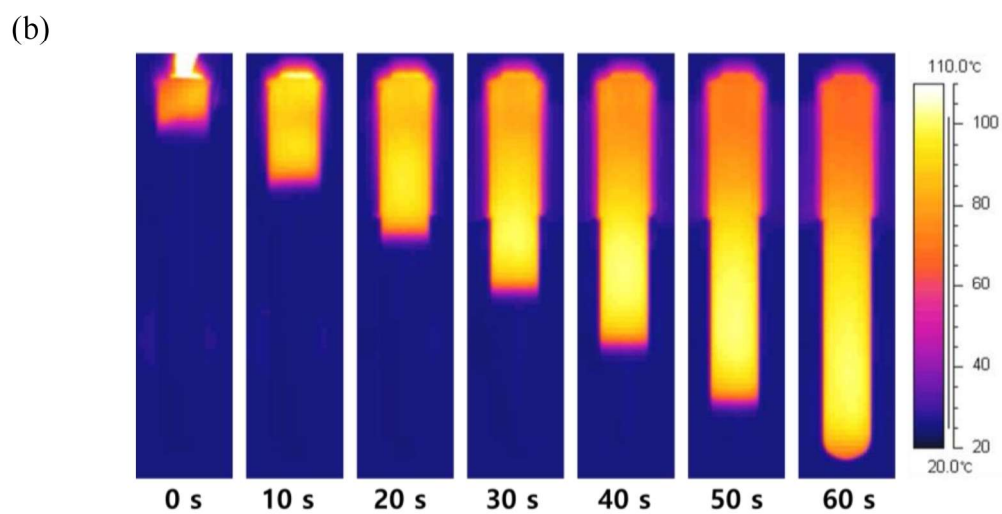
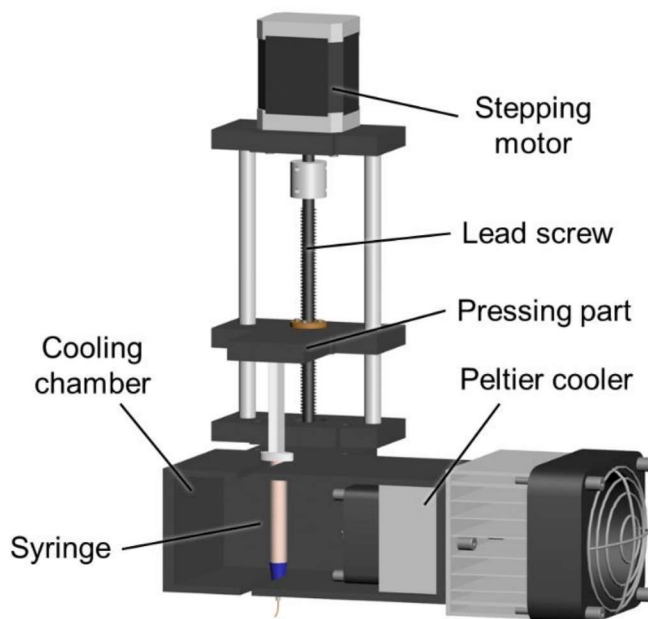


**Figure 3-5** (a) Frontal polymerization of *fpSMP* ink, (b) IR camera image for frontal velocity, and (c) frontal velocity according to incubation time.

### 3.2.3. 3D printing and the shape memory properties of *fp*SMP

The optimal 3D printing conditions were determined based on the rheological properties of the *fp*SMP, as described in Section 3.2. A 3D printing system was built, as shown in Figure 3-6(a), with three-axis motion control. Note that after an incubation period of 183 min, the syringe was placed in a cooling chamber and maintained at  $-5^{\circ}\text{C}$  using a Peltier cooler. The speed of the stepper motor was adjusted so that the ink was extruded with a diameter of 1.77 mm, being pushed with the piston of the syringe moving at 0.147 ml/min. During printing, frontal polymerization was initiated by heating at a distance of 10 mm from the nozzle tip.

(a)



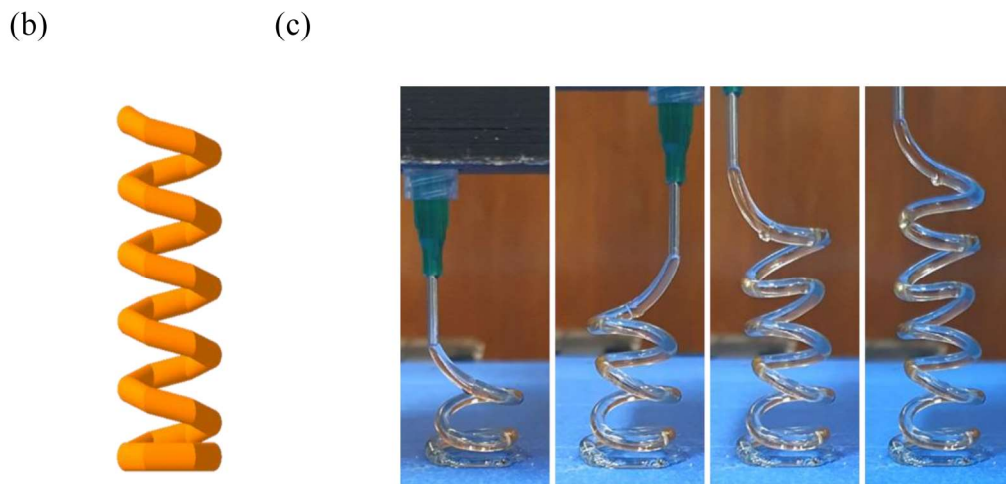


**Figure 3-6** (a) Schematic showing the printing head used to extrude *fpSMP*, (b) 3D design of free-standing structure along with a (c) picture of the actual 3D-printed part.

To demonstrate printing of a free-standing structure, a regular hexagonal spiral was designed with side and lead lengths of 10 mm (Figure 3-6(b)). The printed product, shown in Figure 3-6(c). Thus, *fpSMP* was successfully printed into an unsupported, free-standing structure as frontal polymerization along the printing path fixed the emerging shape. Since the distance between the nozzle and frontal line was held at 10 mm, there were some slight differences between the designed and printed products, e.g., a circular spiral with softer edges was obtained instead of a regular hexagonal spiral.

Figure 3-7(a) shows the shape memory behavior of a printed *fpSMP* wire as it is heated above its transition temperature, stretched in the longitudinal direction, cooled to fix it in a temporary shape, and then heated above the transition

temperature to recover its original shape

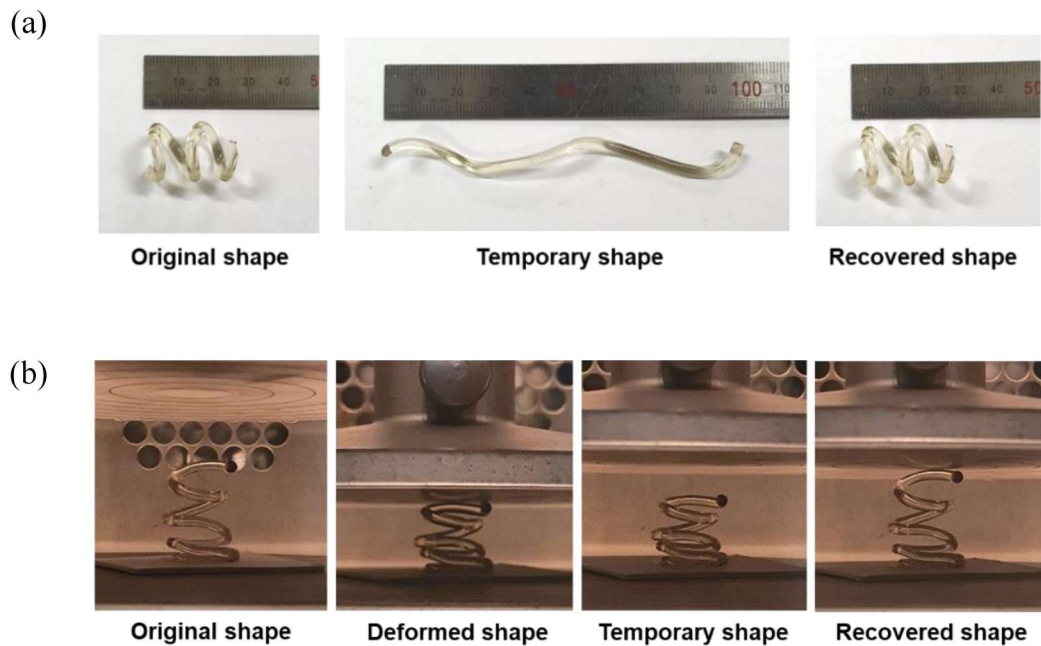


**Figure 3-7** Shape memory behavior of 3D printed *fpSMP* under (a) tensile deformation and (b) compressive deformation.

Figure 3-7(b) shows the shape memory behavior of printed *fpSMP* under compression. The printed *fpSMP* was compressed by 30% in the longitudinal direction. The shape memory properties of the printed *fpSMP* were quantified by periodically measuring the length of the shape along the axis of compression. The fixity and recovery ratio were 94.5% (1.6) and 88.8% (2.7), respectively, indicating a high degree of shape memory.

### 3.3. Summary

A thermoset SMP capable of frontal polymerization (*fp*SMP) was synthesized from DCPD and CO monomers with GC2 as a catalyst. The thermomechanical properties of *fp*SMP were consistent with its amenability to frontal polymerization and high degree of shape memory. The printing conditions were optimized with a focus on the rheological properties of *fp*SMP as a function of incubation time and frontal polymerization velocity, resulting in a 3D printing system capable of creating complex, free-standing structures. Finally, to demonstrate the utility of the developed system, a free-standing hexagonal spiral was successfully printed using *fp*SMP.

# **Chapter 4. 3D printing of porous shape memory polymer**

Porous polymers are gaining increased interest in several areas due to their large surface area and unique physiochemical properties [58-62]. In particular, porous polymers are used as shielding materials due to their large internal surface area [65]. Due to the low thermal conductivity of the air and the reflection of radiation due to the large surface area, it is used as an insulator [66-68], and is also used as electromagnetic interference shielding materials due to internal reflection [61, 69]. However, the porous structure has a disadvantage in that mechanical properties are poor [70, 137]. Therefore, it is necessary to design a porous structure with excellent shielding properties while maintaining mechanical properties.

Methods for fabricating porous polymer include supercritical fluids [76], emulsion templating [75], freeze drying [68, 74] and microfluidic [71, 72]. Most methods are suitable for making simple shapes, but difficult to use for constructing complex shapes. In the case of microfluidic method, researches have been conducted to fabricate a porous structure by grafting it to 3D printing system. This method has the advantage of being able to easily control the pore size and porosity, but has the disadvantage of requiring additional supporting materials to make a complex structure [71, 72]. In addition to this, direct bubble writing method has been

combined with 3D printing. In this study, pores were well formed inside the polymer using a core-shell nozzle similar to the microfluidic method. However, this method was also not suitable for making complex shapes in that the shape of the material could not be fixed immediately after printing [138].

In this chapter, a porous shape memory polymer was manufactured by 3D printing with a core-shell nozzle. By continuously injecting air into the core nozzle, a porous structure corresponding to the low porosity region was fabricated. In addition, mechanical and thermal properties of a porous SMP were evaluated to confirm their applicability as shielding materials. Frontal polymerization mechanism of shape memory polymers was suitable for printing porous polymers with complex structures. Finally, a free-standing structure was printed to demonstrate printability and shape memory behavior of the porous *fp*SMP.

## **4.1. Experimental**

### **4.1.1. Materials and sample preparation**

DCPD, cis-cyclooctene (CO), 5-ethylidene-2-norbornene (ENB), 2nd generation Grubbs' catalyst (GC2), phenylcyclohexane (PCH) and triethyl phosphate (TEP) were purchased from Sigma-Aldrich. DCPD/CO solution was prepared by adding CO in an amount corresponding to 0.15 to the molar equivalent of DCPD, and then mixed for 2 minutes at 2000 rpm through a planetary centrifugal mixer (ARE-310,

Thinky corporation, Japan). In the case of the catalyst solution, GC2 in an amount corresponding to 100 ppm of the DCPD/CO solution was mixed with PCH and TEP (phosphate inhibitor) in an amount of corresponding to 100 molar equivalents of GC2 was added. After that, it was mixed for 5 minutes at 2000 rpm through the planetary centrifugal mixer. The DCPD/CO solution and the catalyst solution were further mixed for 1 minute at 2000 rpm through the planetary centrifugal mixer, followed by degassed at 2200 rpm for 1 minute. The final solution is the ink for 3D printing.

#### **4.1.2. 3D printing system for porous shape memory polymer**

3D printing system for porous shape memory polymer was mainly composed of nozzle part, flow rate control part and material cartridge part (Figure 4-1). A core-shell nozzle was used to form pores inside the *fpSMP*. In the outer nozzle, the *fpSMP* was extruded, and in the inner nozzle, air bubble came out. The diameter of the inner nozzle was 200 $\mu\text{m}$  and the diameter of the outer nozzle was 1mm. Polymer solution and air flow rate was controlled through an air compressor. The polymer solution was extruded at a pressure of 0.3 MPa and the flow rate was controlled through a flow rate controller. In order to confirm the change of the porous structure according to the flow rate of polymer solution and air pressure of the inner nozzle, the air pressure of the inner nozzle was adjusted in the range from 0.02 MPa to 0.2 MPa. To make a gel state suitable for 3D printing, the polymer solution was incubated at room

temperature for a sufficient time, and then the gel state was maintained in a cooling chamber connected to a Peltier cooler. 3D printing was performed by mounting the flow rate control valve connected to the nozzle on a 3D printer.

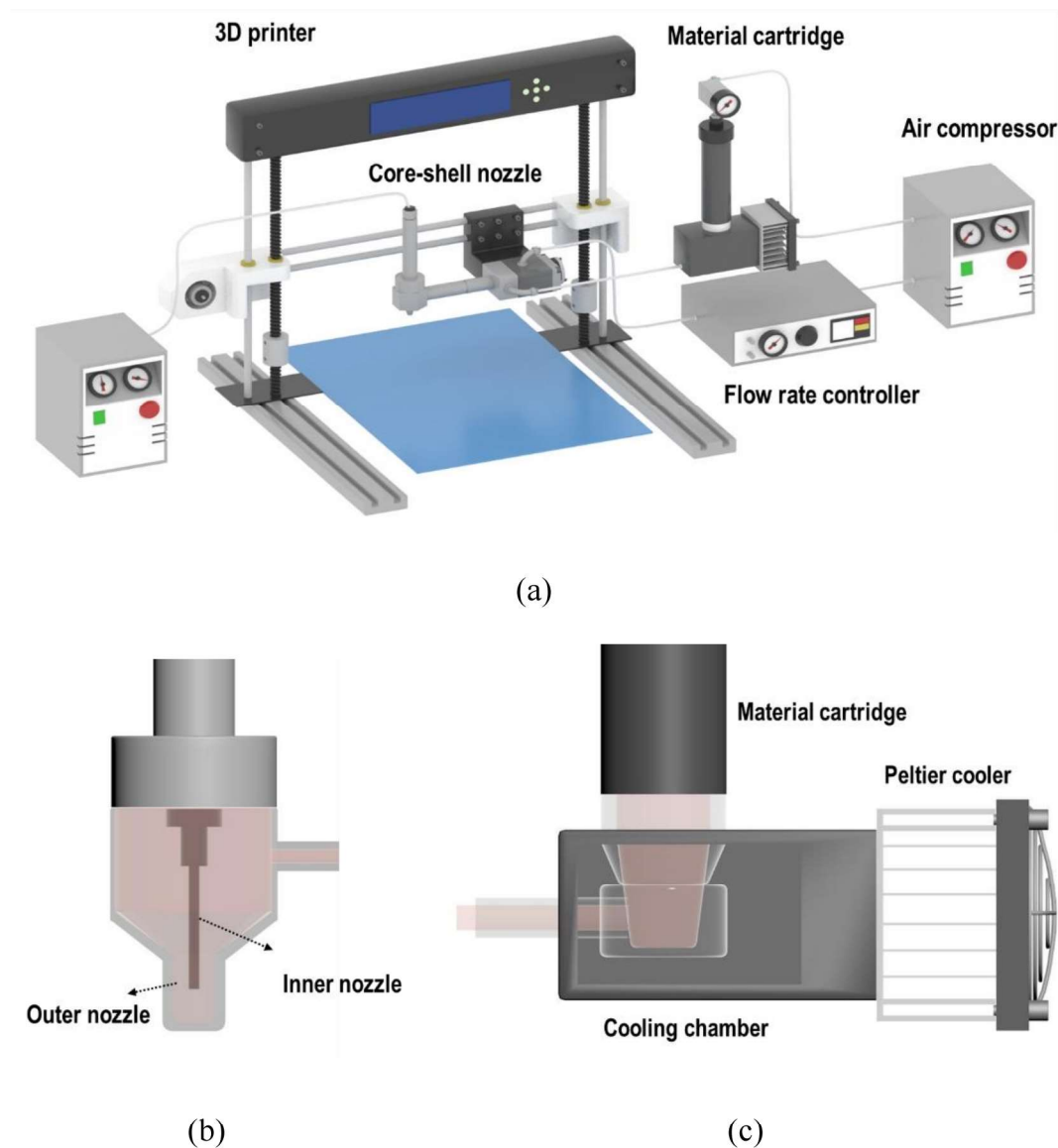


**Figure 4-1** Schematic diagram of (a) 3D printing system for porous shape memory polymer (b) core-shell nozzle and (c) cooling chamber with Peltier cooler

### 4.1.3. Characterization

The structure of the printed porous shape memory polymer was analyzed through X-ray microtomography (Micro CT) analysis (Skyscan 1272, Bruker microCT, MA, USA). After micro CT scan, porosity and average pore diameter were analyzed using CT analysis software (CTan, Bruker, MA, USA). The mechanical properties of the porous shape memory polymer were measured using a universal tensile machine (Quasar 5, Galdabini, Italy), and the measurement was carried out according to ASTM D638. For the measurement of thermal conductivity, thermal diffusivity was measured through laser flash method (LFA457, NETZSCH, Germany), and specific heat was measured through Differential calorimetry scanning measurement (200 F3 Maia, NETZSCH, Germany). Through these measurement, the thermal conductivity was calculated as follow.

$$k = \alpha * \rho * C_p$$

where  $\alpha$  is thermal diffusivity,  $\rho$  is density and  $C_p$  is specific heat. For printed free-standing structures, shape memory properties were measured under compressive conditions.

## **4.2. Modeling approach of mechanical/thermal analysis of porous structure**

### **4.2.1. Generation of porous structure**

The porous structure was generated through Matlab software. First, the porosity was set to have a low porosity range from 0.01 to 0.1, and the diameter was set randomly in the range of 150 ~ 450  $\mu\text{m}$ . In order to generate various types of pore structures, spheroid-type pores were set, and rotation was applied to give variation to orientation. It was confirmed whether it had a closed pore shape under the set porosity and diameter conditions. After having a closed porous structure, the coordinates of the pores were randomly set using a random seed array method. Then, by checking whether each pore overlaps each other, a non-overlapping porous structure was generated. A total of 1000 geometries were generated and the porous structure was used as a representative volume element (RVE) in finite element modeling. The porosity of 1000 geometries was randomly generated within the set range, and it was confirmed that the pores did not overlap each other.

### **4.2.2. Mechanical/thermal analysis of porous structure**

Mechanical and thermal analysis of the porous structure was simulated through ABAQUS software (SIMULIA, RI, USA). Because the RVE type porous structure was used for uniformity of geometry, the analysis was conducted by applying the periodic boundary condition [139, 140]. The mechanical simulation was performed

in the elastic region to obtain effective elastic modulus of porous structure and the materials parameters used for the analysis were obtained through the tensile test of the *fp*SMP according to ASTM D638 (Table 4-1).

The mechanism of heat transfer can be classified into conduction, convection, and radiation. Conduction is a process in which transfer of heat takes place between objects by direct contact. Convection refers to the form of heat transfer in which energy transition occurs within the fluid or gas. Radiation alludes to the mechanism in which heat is transmitted without any physical contact between objects. Energy radiated from an object in the form of electromagnetic waves or photons due to changes in the arrangement of electrons in an atom or molecule [141]. Among these mechanisms, the mechanism of heat transfer that can occur in the porous structure is conduction in the matrix, gaseous conduction generated in the pores, and radiation and convection that can occur in the pores. Among these, convection can be neglected for pores with a diameter smaller than 4 mm [142]. Therefore, it was not implemented. The radiation in the pores was implemented as cavity radiation in the interface properties that calculated using the Stefan-Boltzman equation. The materials parameters are summarized in Table 4-1.

**Table 4-1** Material parameter for mechanical/thermal analysis

Elastic modulus	2013.42 MPa
Poisson's ratio	0.4087
Thermal conductivity of <i>fp</i> SMP	0.18382 W/mK
Thermal conductivity of air	0.02551 W/mK
Emissivity	0.9

### **4.3. 3D printing of porous shape memory polymer.**

#### **4.3.1. Structural analysis of porous shape memory polymer**

Printing was carried out by changing the flow rate (1.57 / 5.41 / 15.71 ml/min) of the *fp*SMP solution and the air pressure (from 0.02 to 0.2 MPa) of the inner nozzle to confirm the change of the porous structure according to the printing conditions. Four types of printing phenomena were observed. First, the dripping that occurred because the flow rate was too low. Second, the printing proceeded, but the air pressure was too low, so a non-porous structure was formed. Third, a porous structure was formed due to the proper air pressure and the flow rate of the polymer solution. Last, there was a spraying phenomenon that occurred because the air pressure was too high. Figure 4-2 summarized the printing phenomena that occurred under each flow rate and air pressure condition. Under the flow rate printing condition of 1.57ml/min, the range of air pressure was narrow and printing was performed with an interval of 0.02 MPa, and for the other two flow rates, printing was performed with an interval of 0.05 MPa. In the section where the flow rate was less than 1.57ml/min, printing was not performed and the solution was dripping. As the flow rate increased, the range of air pressure at which the porous structure was formed widened, and the maximum air pressure also increased.

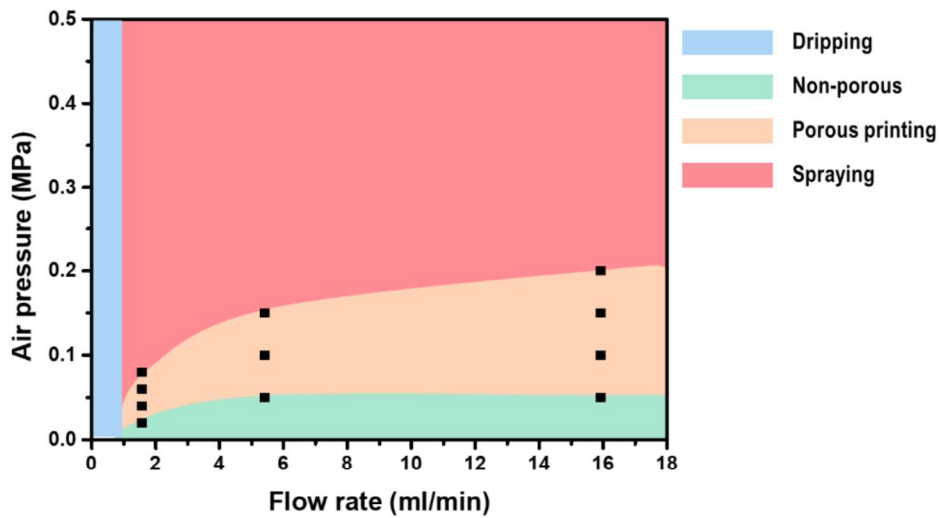
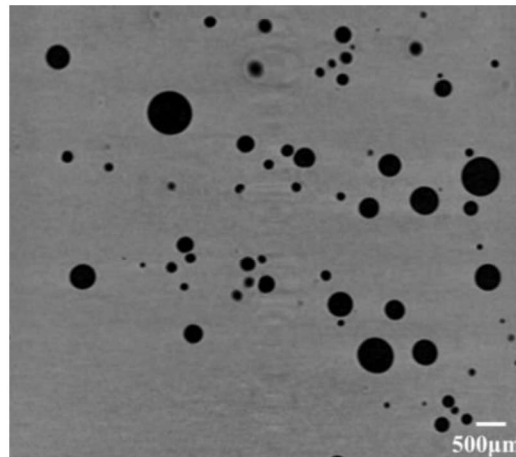


**Figure 4-2** Printability of porous shape memory polymer at different printing condition

Structural analysis was carried out by micro CT analysis of the porous shape memory polymer made under each condition. It was confirmed that a porous structure was formed in the printed sample (Figure 4-3). Porosity and pore diameter were measured through CT analysis software. The change in porosity according to the flow rate was not large, but it was confirmed that the porosity increased as the air pressure increased at the same flow rate (Figure 4-4). The diameter of the pore was about 250  $\mu\text{m}$  on average and was hardly affected by the flow rate and air pressure (Table 4-2). This was because the pore diameter was dependent on diameter of inner nozzle [71, 72].

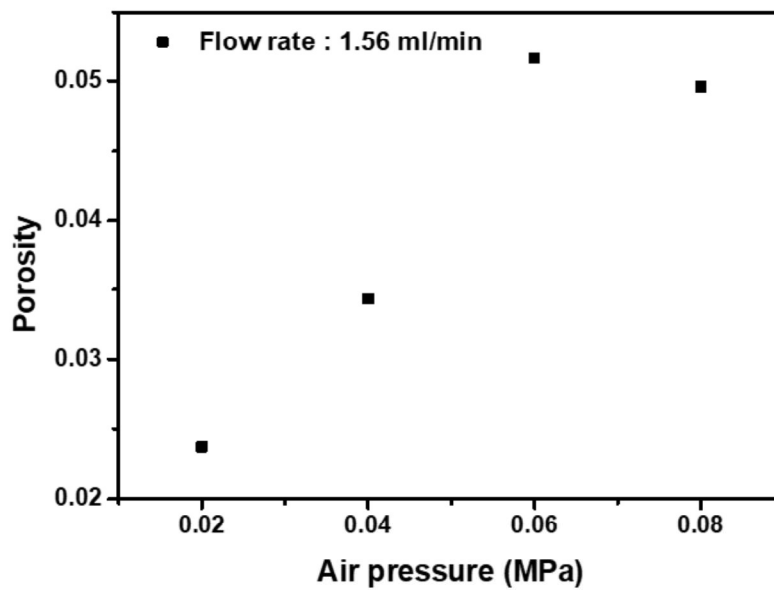


(a)

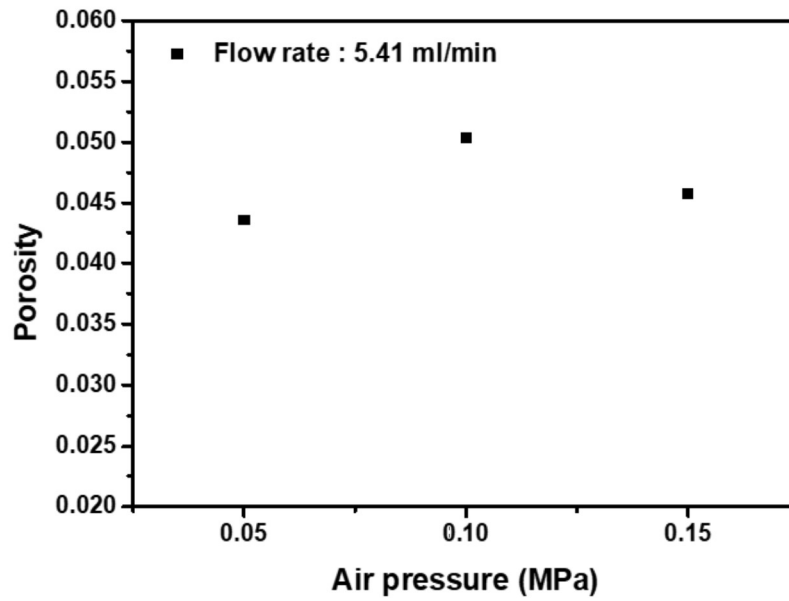


(b)

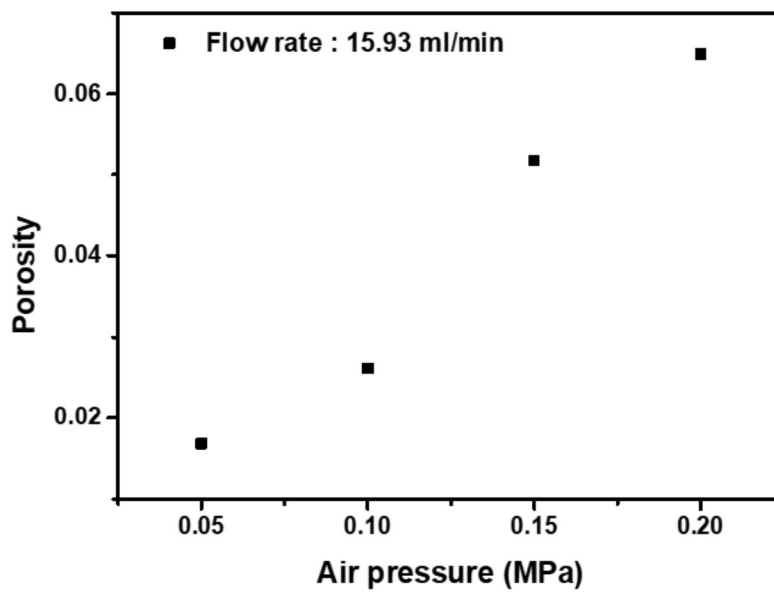
**Figure 4-3** (a) Reconstructed 3D micro CT image and (b) 2D micro CT image of porous *fpSMP* (Flow rate : 1.57ml/min, air pressure : 0.08 MPa)



(a)



(b)



(c)

**Figure 4-4** Porosity of printed *fp*SMP at each printing condition (a) 1.56 ml/min (b) 5.41 ml/min and (c) 15.93 ml/min

**Table 4-2** Average pore diameter of porous *fp*SMP at each printing condition

Flow rate	Air pressure	Pore diameter ( $\mu\text{m}$ )
1.56 ml/min	0.02 MPa	199.02 $\pm$ (91.40)
	0.04 MPa	205.61 $\pm$ (61.54)
	0.06 MPa	180.98 $\pm$ (70.35)
	0.08 MPa	239.21 $\pm$ (73.25)
5.41 ml/min	0.05 MPa	277.84 $\pm$ (71.21)
	0.10 MPa	255.80 $\pm$ (95.09)
	0.15 MPa	256.73 $\pm$ (86.46)
15.93 ml/min	0.05 MPa	208.45 $\pm$ (71.21)
	0.10 MPa	176.56 $\pm$ (32.80)
	0.15 MPa	245.82 $\pm$ (51.52)
	0.20 MPa	194.85 $\pm$ (38.84)

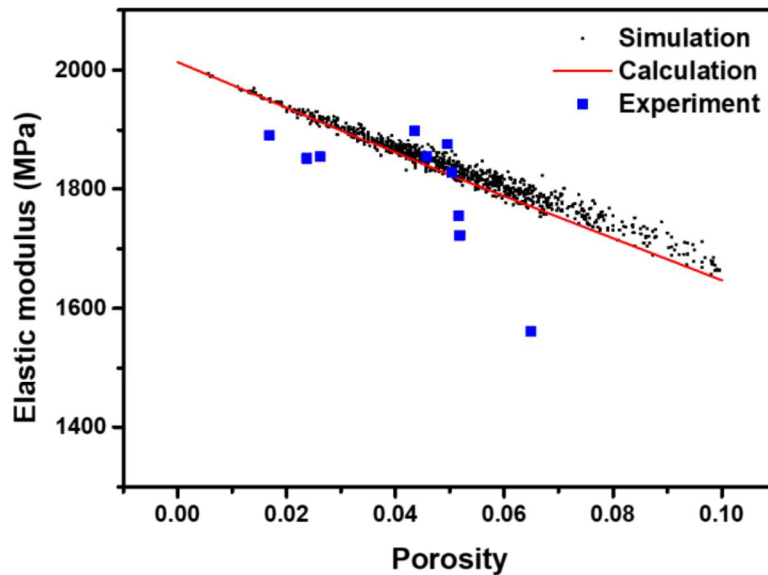
#### 4.3.2. Mechanical/thermal properties of porous shape memory polymer

The effective modulus of generated porous structures was analyzed through ABAQUS simulation. To check the validity of the simulation results, the mechanical properties according to the porosity were calculated using the Composite Sphere model (CSM), the classical theories to calculate the effective modulus of the porous structure [137, 143]. In the composite sphere model, the effective modulus can be calculated as follows.

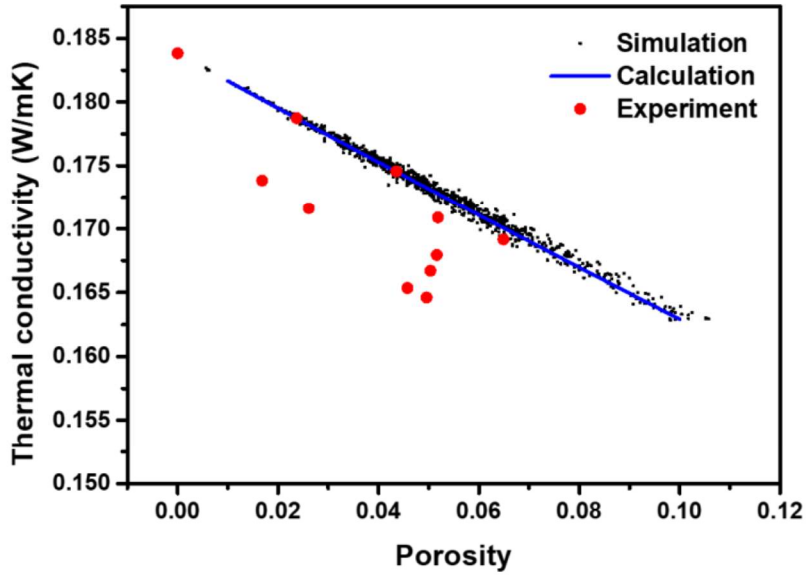
$$\frac{K}{E_m} = 1 - \frac{c}{1 - \frac{(1-c)(1+\nu_m)}{3(1-\nu_m)}}, \quad E = 3K(1-2\nu)$$

where K is effective bulk modulus of porous structure. E is effective modulus of porous structure,  $E_m$  is modulus of matrix, c is porosity and  $\nu_m$  is Poisson's ratio of matrix. It was confirmed that there was no significant difference between the

Results of the composite sphere model and the analysis results. The mechanical properties of the *fp*SMP were measured according to ASTM D638. However, most of the experimental data tended to be lower than the simulation results and calculation results (Figure 4-5). This is because, in case of printed porous *fp*SMP, the distribution of pore was not uniform as shown in the Figure 4-3. The effective modulus decreased as the porosity increased. At 0.1 of porosity, the elastic modulus decreased about 19%.



(a)



(b)

**Figure 4-5** Experiment/simulation results of (a) mechanical (elastic modulus) and (b) thermal (thermal conductivity) of porous *fpSMP*

Heat transfer simulation results were also compared with the existing theories to verify the validity of the model. Classical theories of thermal conductivity of porous materials include theories of Maxwell-Eucken, Landauer, and Rayleigh relation. Among them, in the low porosity region (porosity < 0.15), Maxwell-Eucken relation is well described [144].

$$k_{eff} = k_s \frac{k_p + 2k_m + 2v_p(k_p - k_m)}{k_p + 2k_m - v_p(k_p - k_m)}$$

where  $k_{eff}$  is effective thermal conductivity of porous materials,  $k_p$  is thermal

conductivity of pore,  $k_m$  is thermal conductivity of matrix and  $v_p$  is porosity. Because the conduction of air and radiation occur at the same time for heat transfer in the pores, thermal conductivity by radiation must be considered and can be calculated using Loeb's equation [145].

$$k_p = k_{con} + k_{rad}$$

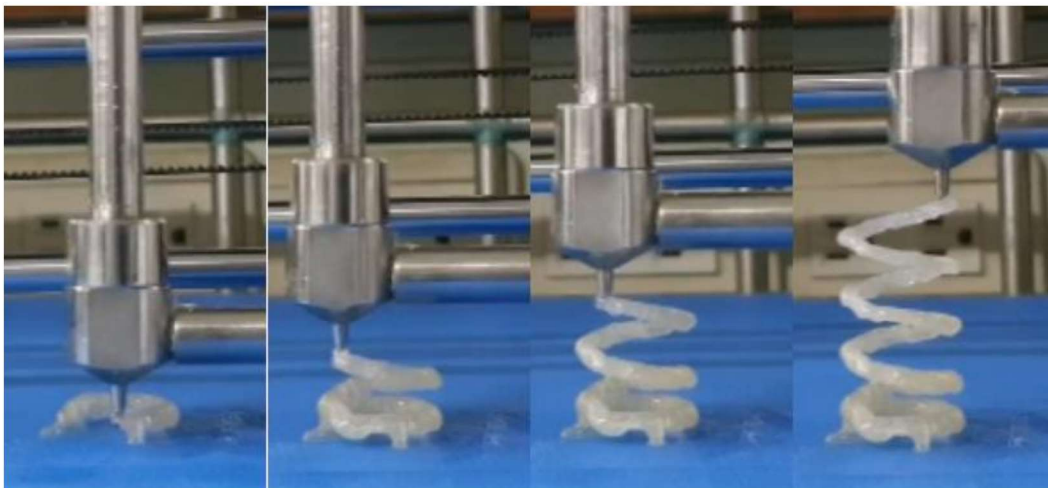
$$k_{rad} = 4\epsilon\sigma d_{max}\gamma T^3$$

where  $\epsilon$  is emissivity of matrix,  $\sigma$  is Stefan-Boltzmann constant,  $\gamma$  is geometrical factor (sphere: 2/3, cylinder:  $\pi/4$ ) and  $d_{max}$  is maximum distance inside the pore. There was no significant difference when comparing the simulation results with the thermal conductivity calculated through the Maxwell-Eucken equation. The thermal conductivity measured through the experiment also showed a lower result value when compared with the analysis and calculated values. At a porosity of 0.1, it was confirmed that the thermal conductivity decreased by about 13% compared to the thermal conductivity of matrix.

#### **4.3.3. 3D printing of porous *fp*SMP and shape memory properties**

To print a free-stand structure through 3D printing, the *fp*SMP solution was gelled at room temperature for 180 minutes and then put into material cartridge in a cooling chamber composed of a Peltier cooler. A printhead consisting of a flow rate control

valve and a core shell nozzle was installed in the 3D printer. A hexagonal spiral structure with a side length of 10 mm was designed for printing 3D free-standing structures. The printing speed was set to 50 mm/min to match the frontal polymerization speed and flow rate of polymer solution was set to 3.7 ml/min. Air pressure of inner nozzle was set to 0.05 MPa. Initiation of frontal polymerization was carried out using soldering iron. A free-standing structure was successfully printed as shown in the Figure 4-6. The porous structure of a part of the printed sample was confirmed through micro CT analysis. It was found that pores were well formed inside the printed sample, and the orientation was formed in that direction as the polymerization direction was determined in the printed direction. Porosity of printed *fp*SMP was 0.0916 and average diameter of pore was 87.5  $\mu\text{m}$  of shorter axis and 476  $\mu\text{m}$  of longer axis.



(a)

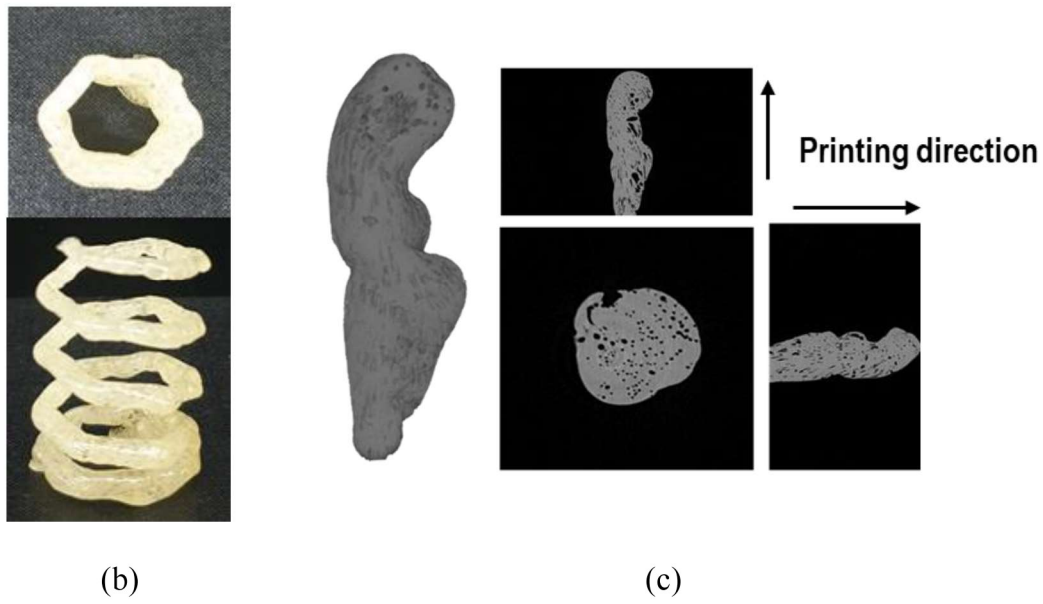


**Figure 4-6** (a) 3D printing of a free-standing structure, (b) top/side view of printed *fpSMP* and (c) 3D/2D micro CT image of printed porous *fpSMP*

In order to measure the shape memory performance of the printed sample, a shape memory test was performed under compressive conditions. Shape memory performance was measured in the following step. First, raising the temperature above glass transition temperature, *fpSMP* was deformed into deformed shape. The shape was fixed below the glass transition temperature (Temporary shape). After that, the permanent shape was recovered by raising the temperature again.

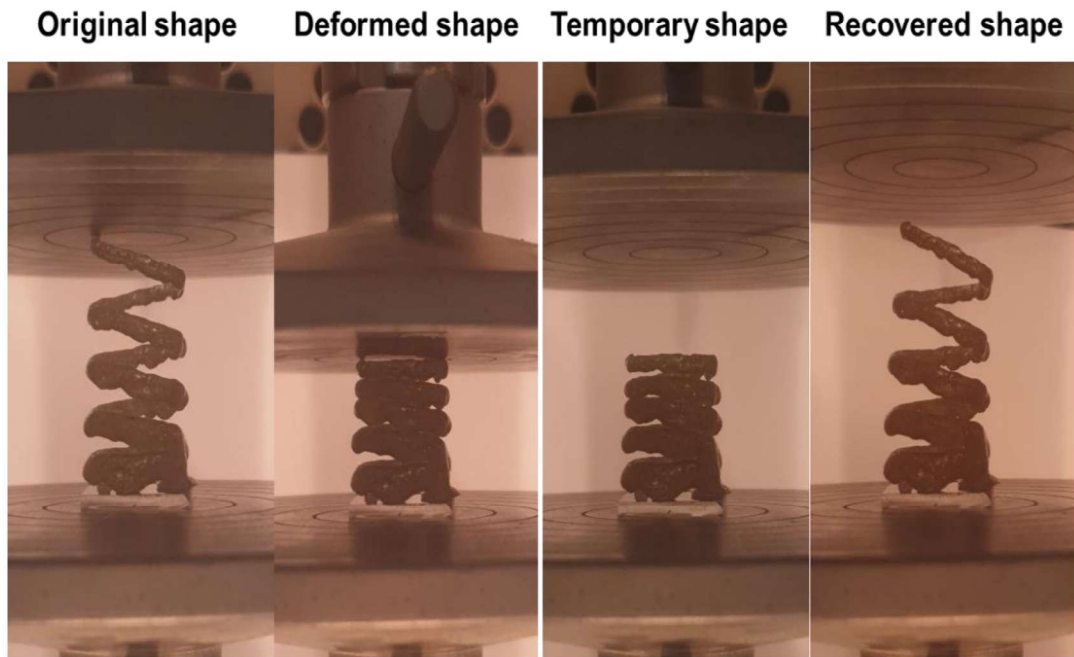


**Figure 4-7** Shape memory behavior of 3D printed porous *fpSMP* under compressive condition

Figure 4-7 showed the shape memory behavior of printed porous *fpSMP* under compression. The printed *fpSMP* was compressed by 35% in the longitudinal direction. The shape memory properties of the printed *fpSMP* were quantified by measuring the length of the shape along the axis of compression. The fixity and recovery ratio were 98% and 100%, respectively, indicating a high degree of shape memory.

#### **4.4. Summary**

3D printing of porous shape memory polymer was proceed using a new 3D printing system with core-shell nozzle and frontal polymerization. The porosity of the *fp*SMP was between 0 and 0.1, which is the low porosity region. The porous structure was analyzed through micro CT analysis and the mechanical/thermal behavior of porous structure was analyzed. The elastic modulus and thermal conductivity of the porous structure showed a linear decrease as the porosity increased and showed the same trend as the analysis results. 3D printing was capable of creating complex, free-standing structure using the optimization of appropriate rheological properties and frontal polymerization. Finally, a free-standing hexagonal spiral was successfully printed and showed a high degree of shape memory properties.

## Chapter 5. Concluding remarks

The purpose of this study is to develop a new 3D printing system for porous shape memory polymer, and to establish a model to predict long-term durability of shape memory polymer in space environment.

First, a method for predicting long-term properties of shape memory polymer in a Low earth orbit was proposed. In this study, we constructed a space environment chamber including a high vacuum, ultraviolet radiation and atomic oxygen condition. An accelerated test was conducted based on the time-temperature superposition, and for this purpose, a shape memory polymer was exposed to the space environment in a high temperature region. The long-term mechanical behavior of SMPs in the LEO environment was then predicted by the linear product of the shift factors obtained from the three accelerated tests.

Secondly, a new 3D printing system was developed for printing a complex geometry. A thermoset SMP capable of frontal polymerization was synthesized using dicyclopentadiene (DCPD) and cyclooctene (CO) with Grubbs' catalyst. Here, CO was co-polymerized with DCPD to impart the shape memory behavior. The rheological properties and speed of frontal polymerization were evaluated to identify optimal conditions for 3D printing. Finally, a free-standing 3D structure was printed to demonstrate the printability and shape memory behavior of *fp*SMP.

Thirdly, Porous shape memory polymer was 3D printed using core-shell nozzle

system. By continuously injecting air into the core nozzle, a porous structure corresponding to the low porosity region was fabricated. In addition, mechanical and thermal properties of a porous SMP were evaluated to confirm their applicability of shielding materials. Frontal polymerization mechanism of shape memory polymers was suitable for printing porous polymers with complex structures. Finally, a free-standing structure was printed to demonstrate printability and shape memory behavior of the porous *fp*SMP.

Using the accelerated testing method and prediction long-term properties in this study, the durability of shape memory polymer can be easily estimated. Especially, 3D printing system of porous shape memory polymer has an effect on the long-term durability improvement of the shape memory polymer and shows the potential as a shielding material. Additionally, methods to analyze thermodynamic and rheological properties to investigate printability will be helpful in the development of 3D printing processes of thermosetting polymers

## Reference

1. Lendlein, A. and S. Kelch, *Shape-Memory Polymers*. Angewandte Chemie International Edition, 2002. **41**(12): p. 2034-2057.
2. Xue, L., S. Dai, and Z. Li, *Biodegradable shape-memory block co-polymers for fast self-expandable stents*. Biomaterials, 2010. **31**(32): p. 8132-8140.
3. Govindarajan, T. and R. Shandas, *A survey of surface modification techniques for next-generation shape memory polymer stent devices*. Polymers, 2014. **6**(9): p. 2309-2331.
4. Yakacki, C.M., et al., *Unconstrained recovery characterization of shape-memory polymer networks for cardiovascular applications*. Biomaterials, 2007. **28**(14): p. 2255-2263.
5. Lendlein, A. and R. Langer, *Biodegradable, elastic shape-memory polymers for potential biomedical applications*. Science, 2002. **296**(5573): p. 1673-1676.
6. Gall, K., et al., *Thermomechanics of the shape memory effect in polymers for biomedical applications*. Journal of Biomedical Materials Research Part A: An Official Journal of The Society for Biomaterials, The Japanese Society for Biomaterials, and The Australian Society for Biomaterials and the Korean Society for Biomaterials, 2005. **73**(3): p. 339-348.
7. Monkman, G.J., *Advances in shape memory polymer actuation*. Mechatronics, 2000. **10**(4): p. 489-498.
8. Firouzeh, A., M. Salerno, and J. Paik, *Stiffness control with shape memory polymer in underactuated robotic origamis*. IEEE Transactions on Robotics, 2017. **33**(4): p. 765-777.
9. Jin, B., et al., *Programming a crystalline shape memory polymer network with thermo-and photo-reversible bonds toward a single-component soft robot*. Science advances, 2018. **4**(1): p. eaao3865.
10. Hines, L., V. Arabagi, and M. Sitti, *Shape memory polymer-based flexure stiffness control in a miniature flapping-wing robot*. IEEE Transactions on Robotics, 2012. **28**(4): p. 987-990.
11. Lu, H. and S. Du, *A phenomenological thermodynamic model for the chemo-responsive shape memory effect in polymers based on Flory–*

- Huggins solution theory*. Polymer Chemistry, 2014. **5**(4): p. 1155-1162.
12. Sun, L., et al., *Stimulus-responsive shape memory materials: a review*. Materials & Design, 2012. **33**: p. 577-640.
  13. Liu, Y., et al., *Shape memory polymers and their composites in aerospace applications: a review*. Smart Materials and Structures, 2014. **23**(2): p. 023001.
  14. Lendlein, A. and S. Kelch, *Shape-memory polymers*. Angewandte Chemie International Edition, 2002. **41**(12): p. 2034-2057.
  15. Huang, W., *On the selection of shape memory alloys for actuators*. Materials & Design, 2002. **23**(1): p. 11-19.
  16. Lan, X., et al., *Fiber reinforced shape-memory polymer composite and its application in a deployable hinge*. Smart Materials and Structures, 2009. **18**(2): p. 024002.
  17. Meng, Q. and J. Hu, *A review of shape memory polymer composites and blends*. Composites Part A: Applied Science and Manufacturing, 2009. **40**(11): p. 1661-1672.
  18. Bye, D. and P. McClure. *Design of a morphing vehicle*. in *48th AIAA/ASME/ASCE/AHS/ASC structures, structural dynamics, and materials conference*. 2007.
  19. Arzberger, S.C., et al. *Elastic memory composites (EMC) for deployable industrial and commercial applications*. in *Smart structures and materials 2005: industrial and commercial applications of smart structures technologies*. 2005. International Society for Optics and Photonics.
  20. Tupper, M., et al. *Developments in elastic memory composite materials for spacecraft deployable structures*. in *2001 IEEE Aerospace Conference Proceedings (Cat. No. 01TH8542)*. 2001. IEEE.
  21. Keller, P., et al. *Development of a deployable boom for microsattellites using elastic memory composite material*. in *45th AIAA/ASME/ASCE/AHS/ASC Structures, Structural Dynamics & Materials Conference*. 2004.
  22. Dao, T.D., et al., *Design, fabrication, and bending test of shape memory polymer composite hinges for space deployable structures*. Journal of

- Intelligent Material Systems and Structures, 2017. **29**(8): p. 1560-1574.
23. Hinkle, J., J. Lin, and D. Kling. *Design and materials study on secondary structures in deployable planetary and space habitats*. in *52nd AIAA/ASME/ASCE/AHS/ASC Structures, Structural Dynamics and Materials Conference 19th AIAA/ASME/AHS Adaptive Structures Conference 13t*. 2014.
  24. Wang, W., H. Rodrigue, and S.-H. Ahn, *Deployable soft composite structures*. Scientific reports, 2016. **6**(1): p. 1-10.
  25. Barrett, R., et al., *Deployable reflectors for small satellites*. 2007.
  26. Lake, M., et al. *Application of elastic memory composite materials to deployable space structures*. in *AIAA Space 2001 Conference and Exposition*. 2001.
  27. Lin, J., C. Knoll, and C. Willey. *Shape memory rigidizable inflatable (RI) structures for large space systems applications*. in *47th AIAA/ASME/ASCE/AHS/ASC Structures, Structural Dynamics, and Materials Conference 14th AIAA/ASME/AHS Adaptive Structures Conference 7th*. 2006.
  28. Yin, W., J. Liu, and J. Leng, *Deformation analysis of shape memory polymer for morphing wing skin under airflow*. Frontiers of Mechanical Engineering in China, 2009. **4**(4): p. 447.
  29. Keller, P., et al. *Development of elastic memory composite stiffeners for a flexible precision reflector*. in *47th AIAA/ASME/ASCE/AHS/ASC Structures, Structural Dynamics, and Materials Conference 14th AIAA/ASME/AHS Adaptive Structures Conference 7th*. 2006.
  30. Francis, W., et al. *Development and testing of a hinge/actuator using elastic memory composites*. in *44th AIAA/ASME/ASCE/AHS/ASC Structures, Structural Dynamics, and Materials Conference*. 2003.
  31. Beavers, F., et al. *Design and testing of an elastic memory composite deployment hinge for spacecraft*. in *43rd AIAA/ASME/ASCE/AHS/ASC Structures, Structural Dynamics, and Materials Conference*. 2002.
  32. Shin, K.-B., et al., *Prediction of failure thermal cycles in graphite/epoxy composite materials under simulated low earth orbit environments*.

- Composites Part B: Engineering, 2000. **31**(3): p. 223-235.
33. Grossman, E. and I. Gouzman, *Space environment effects on polymers in low earth orbit*. Nuclear Instruments and Methods in Physics Research Section B: Beam Interactions with Materials and Atoms, 2003. **208**: p. 48-57.
  34. Han, J.-H. and C.-G. Kim, *Low earth orbit space environment simulation and its effects on graphite/epoxy composites*. Composite structures, 2006. **72**(2): p. 218-226.
  35. Moon, J.-B., et al., *Improvement of tensile properties of CFRP composites under LEO space environment by applying MWNTs and thin-ply*. Composites Part A: Applied Science and Manufacturing, 2011. **42**(6): p. 694-701.
  36. Awaja, F., et al., *Surface molecular degradation of 3D glass polymer composite under low earth orbit simulated space environment*. Polymer Degradation and Stability, 2010. **95**(6): p. 987-996.
  37. Tan, Q., et al., *Study of low earth orbit ultraviolet radiation and vacuum thermal cycling environment effects on epoxy-based shape memory polymer*. Journal of Intelligent Material Systems and Structures, 2019. **30**(18-19): p. 2688-2696.
  38. Tan, Q., et al., *Effects of atomic oxygen on epoxy-based shape memory polymer in low earth orbit*. Journal of Intelligent Material Systems and Structures, 2017. **29**(6): p. 1081-1087.
  39. Qian, M., et al., *Resistance of POSS Polyimide Blends to Hyperthermal Atomic Oxygen Attack*. ACS Appl Mater Interfaces, 2016. **8**(49): p. 33982-33992.
  40. Wang, X., et al., *Mechanically Robust Atomic Oxygen-Resistant Coatings Capable of Autonomously Healing Damage in Low Earth Orbit Space Environment*. Adv Mater, 2018: p. e1803854.
  41. He, Y., et al., *Atomic oxygen degradation mechanisms of epoxy composites for space applications*. Polymer Degradation and Stability, 2019. **166**: p. 108-120.
  42. An, Y., et al., *Quantitative evaluation of the three-dimensional deployment*

- behavior of a shape memory polymer antenna*. Smart Materials and Structures, 2018. **27**(10): p. 105007.
43. Fabrizio, Q., S. Loredana, and S.E. Anna, *Shape memory epoxy foams for space applications*. Materials Letters, 2012. **69**: p. 20-23.
  44. Gall, K., et al., *Carbon Fiber Reinforced Shape Memory Polymer Composites*. Journal of Intelligent Material Systems and Structures, 2000. **11**(11): p. 877-886.
  45. Jang, J.H., et al., *Long-term properties of carbon fiber-reinforced shape memory epoxy/polymer composites exposed to vacuum and ultraviolet radiation*. Smart Materials and Structures, 2019. **28**(11): p. 115013.
  46. Liu, T., et al., *Integrative hinge based on shape memory polymer composites: Material, design, properties and application*. Composite Structures, 2018. **206**: p. 164-176.
  47. Momeni, F., et al., *A review of 4D printing*. Materials & Design, 2017. **122**: p. 42-79.
  48. Bakarich, S.E., et al., *4D printing with mechanically robust, thermally actuating hydrogels*. Macromolecular rapid communications, 2015. **36**(12): p. 1211-1217.
  49. Gladman, A.S., et al., *Biomimetic 4D printing*. Nature materials, 2016. **15**(4): p. 413-418.
  50. Guo, J., et al., *4D printing of robust hydrogels consisted of agarose nanofibers and polyacrylamide*. ACS Macro Letters, 2018. **7**(4): p. 442-446.
  51. Hu, Y., et al., *Botanical-inspired 4D printing of hydrogel at the microscale*. Advanced Functional Materials, 2020. **30**(4): p. 1907377.
  52. Naficy, S., et al., *4D printing of reversible shape morphing hydrogel structures*. Macromolecular Materials and Engineering, 2017. **302**(1): p. 1600212.
  53. Choong, Y.Y.C., et al., *4D printing of high performance shape memory polymer using stereolithography*. Materials & Design, 2017. **126**: p. 219-225.
  54. Ding, Z., et al., *Direct 4D printing via active composite materials*. Science advances, 2017. **3**(4): p. e1602890.

55. Ge, Q., et al., *Multimaterial 4D printing with tailorable shape memory polymers*. Scientific reports, 2016. **6**: p. 31110.
56. Wei, H., et al., *Direct-write fabrication of 4D active shape-changing structures based on a shape memory polymer and its nanocomposite*. ACS applied materials & interfaces, 2017. **9**(1): p. 876-883.
57. Zhang, Y., et al., *4D printing of a digital shape memory polymer with tunable high performance*. ACS applied materials & interfaces, 2019. **11**(35): p. 32408-32413.
58. Wu, J., et al., *Porous Polymers as Multifunctional Material Platforms toward Task-Specific Applications*. Advanced Materials, 2019. **31**(4): p. 1802922.
59. Berro, S., et al., *From Plastic to Silicone: The Novelties in Porous Polymer Fabrications*. Journal of Nanomaterials, 2015. **2015**: p. 142195.
60. Zhang, Q., et al., *Effect of porosity on long-term degradation of poly ( $\epsilon$ -caprolactone) scaffolds and their cellular response*. Polymer Degradation and Stability, 2013. **98**(1): p. 209-218.
61. Singh, A.K., et al., *A review of porous lightweight composite materials for electromagnetic interference shielding*. Composites Part B: Engineering, 2018. **149**: p. 188-197.
62. Sadasivuni, K.K., et al., *A review on porous polymer composite materials for multifunctional electronic applications*. Polymer-Plastics Technology and Materials, 2019. **58**(12): p. 1253-1294.
63. Hou, Q., D.W. Grijpma, and J. Feijen, *Porous polymeric structures for tissue engineering prepared by a coagulation, compression moulding and salt leaching technique*. Biomaterials, 2003. **24**(11): p. 1937-47.
64. Cao, C.-X., et al., *Synthesis of porous polymer/tissue paper hybrid membranes for switchable oil/water separation*. Scientific Reports, 2017. **7**(1): p. 3101.
65. Wu, C.-Y. and W.A. Aue, *Protected porous polymers*. Canadian Journal of Chemistry, 1989. **67**(3): p. 389-401.
66. Ruckdeschel, P., A. Philipp, and M. Retsch, *Understanding Thermal Insulation in Porous, Particulate Materials*. Advanced Functional Materials, 2017. **27**(38): p. 1702256.

67. Rizvi, A., R.K.M. Chu, and C.B. Park, *Scalable Fabrication of Thermally Insulating Mechanically Resilient Hierarchically Porous Polymer Foams*. ACS Applied Materials & Interfaces, 2018. **10**(44): p. 38410-38417.
68. Cui, Y., et al., *A Thermally Insulating Textile Inspired by Polar Bear Hair*. Advanced Materials, 2018. **30**(14): p. 1706807.
69. Shahzad, F., et al., *Electromagnetic interference shielding with 2D transition metal carbides (MXenes)*. Science, 2016. **353**(6304): p. 1137-1140.
70. Gong, L., S. Kyriakides, and W.Y. Jang, *Compressive response of open-cell foams. Part I: Morphology and elastic properties*. International Journal of Solids and Structures, 2005. **42**(5): p. 1355-1379.
71. Chung, K.-y., et al., *Fabricating scaffolds by microfluidics*. Biomicrofluidics, 2009. **3**(2): p. 022403.
72. Abate, A.R., et al., *Valve-based flow focusing for drop formation*. Applied Physics Letters, 2009. **94**(2): p. 023503.
73. Costantini, M., et al., *3D-Printing of Functionally Graded Porous Materials Using On-Demand Reconfigurable Microfluidics*. Angewandte Chemie International Edition, 2019. **58**(23): p. 7620-7625.
74. Zhang, H. and A.I. Cooper, *Aligned Porous Structures by Directional Freezing*. Advanced Materials, 2007. **19**(11): p. 1529-1533.
75. Gurevitch, I. and M.S. Silverstein, *Nanoparticle-Based and Organic-Phase-Based AGET ATRP PolyHIPE Synthesis within Pickering HIPEs and Surfactant-Stabilized HIPEs*. Macromolecules, 2011. **44**(9): p. 3398-3409.
76. Marascio, M.G.M., et al., *3D Printing of Polymers with Hierarchical Continuous Porosity*. Advanced Materials Technologies, 2017. **2**(11): p. 1700145.
77. Hasan, S.M., L.D. Nash, and D.J. Maitland, *Porous shape memory polymers: Design and applications*. Journal of Polymer Science Part B: Polymer Physics, 2016. **54**(14): p. 1300-1318.
78. Jiang, Z., et al., *Extrusion 3D Printing of Polymeric Materials with Advanced Properties*. Advanced Science, 2020. **7**(17): p. 2001379.
79. Shi, Q., et al., *Recyclable 3D printing of vitrimer epoxy*. Materials Horizons, 2020. **7**(17): p. 2001379.

2017. **4**(4): p. 598-607.
80. Standard, A., *Standard terminology for additive manufacturing technologies*. ASTM International F2792-12a, 2012.
  81. Chandrasekaran, S., et al., *3D printing of high performance cyanate ester thermoset polymers*. Journal of Materials Chemistry A, 2018. **6**(3): p. 853-858.
  82. Compton, B.G. and J.A. Lewis, *3D-printing of lightweight cellular composites*. Advanced materials, 2014. **26**(34): p. 5930-5935.
  83. Lewicki, J.P., et al., *3D-printing of meso-structurally ordered carbon fiber/polymer composites with unprecedented orthotropic physical properties*. Scientific reports, 2017. **7**(1): p. 1-14.
  84. Ishisaka, A. and M. Kawagoe, *Examination of the time–water content superposition on the dynamic viscoelasticity of moistened polyamide 6 and epoxy*. Journal of applied polymer science, 2004. **93**(2): p. 560-567.
  85. Rajaneesh, A., et al., *Long-term life prediction of woven CFRP laminates under three point flexural fatigue*. Composites Part B: Engineering, 2016. **91**: p. 539-547.
  86. Reeder, J.R., *Prediction of long-term strength of thermoplastic composites using time-temperature superposition*. NASA Technical Report NASA/TM-2002-211781, 2002.
  87. Wolfrum, J., S. Eibl, and L. Lietch, *Rapid evaluation of long-term thermal degradation of carbon fibre epoxy composites*. Composites Science and Technology, 2009. **69**(3): p. 523-530.
  88. Yang, D.-G., et al., *Numerical modeling of warpage induced in QFN array molding process*. Microelectronics Reliability, 2007. **47**(2): p. 310-318.
  89. Gentry, T., et al., *Accelerated test methods to determine the long-term behavior of composite highway structures subject to environmental loading*. Journal of Composites, Technology and Research, 1998. **20**(1): p. 38-50.
  90. Kim, Y.K. and S.R. White, *Stress relaxation behavior of 3501-6 epoxy resin during cure*. Polymer Engineering & Science, 1996. **36**(23): p. 2852-2862.
  91. Bank, L.C., T.R. Gentry, and A. Barkatt, *Accelerated test methods to*

- determine the long-term behavior of FRP composite structures: environmental effects.* Journal of Reinforced Plastics and Composites, 1995. **14**(6): p. 559-587.
92. Miyano, Y., M. Nakada, and N. Sekine, *Accelerated testing for long-term durability of FRP laminates for marine use.* Journal of composite materials, 2005. **39**(1): p. 5-20.
  93. Fukushima, K., et al. *DETERMINATION OF TIME-TEMPERATURE SHIFT FACTOR FOR LONG-TERM LIFE PREDICTION OF POLYMER COMPOSITES.* in *Proc. ICCM.*
  94. Torikai, A. and H. Hasegawa, *Accelerated photodegradation of poly (vinyl chloride).* Polymer Degradation and Stability, 1999. **63**(3): p. 441-445.
  95. Torikai, A., A. Takeuchi, and K. Fueki, *The effect of temperature on the photo-degradation of polystyrene.* Polymer degradation and stability, 1986. **14**(4): p. 367-375.
  96. Liu, M. and A.R. Horrocks, *Effect of Carbon Black on UV stability of LLDPE films under artificial weathering conditions.* Polymer Degradation and Stability, 2002. **75**(3): p. 485-499.
  97. Valadez-Gonzalez, A., J.M. Cervantes-Uc, and L. Veleza, *Mineral filler influence on the photo-oxidation of high density polyethylene: I. Accelerated UV chamber exposure test.* Polymer Degradation and Stability, 1999. **63**(2): p. 253-260.
  98. Kumar, B.G., R.P. Singh, and T. Nakamura, *Degradation of carbon fiber-reinforced epoxy composites by ultraviolet radiation and condensation.* Journal of Composite Materials, 2002. **36**(24): p. 2713-2733.
  99. *Effects of accelerated aging on thermal, mechanical and shape memory properties of cyanate-based shape memory polymer: I vacuum ultraviolet radiation.* Polymer Degradation and Stability, 2017. **138**: p. 91 - 97.
  100. *Investigation of ultraviolet radiation effects on thermomechanical properties and shape memory behaviour of styrene-based shape memory polymers and its composite.* Composites Science and Technology, 2018. **165**: p. 266 - 273.
  101. Zhao, X.-H., et al., *An experimental study of low earth orbit atomic oxygen*

- and ultraviolet radiation effects on a spacecraft material – polytetrafluoroethylene*. *Polymer Degradation and Stability*, 2005. **88**(2): p. 275-285.
102. Feng, J. and Z. Guo, *Effects of temperature and frequency on dynamic mechanical properties of glass/epoxy composites*. *Journal of Materials Science*, 2016. **51**(5): p. 2747-2758.
103. Feng, J. and Z. Guo, *Temperature-frequency-dependent mechanical properties model of epoxy resin and its composites*. *Composites Part B: Engineering*, 2016. **85**: p. 161-169.
104. Naresh, K., et al., *Temperature-Frequency-Dependent Viscoelastic Properties of Neat Epoxy and Fiber Reinforced Polymer Composites: Experimental Characterization and Theoretical Predictions*. *Polymers*, 2020. **12**(8): p. 1700.
105. Miyano, Y., M. Nakada, and R. Muki, *Applicability of Fatigue Life Prediction Method to Polymer Composites*. *Mechanics of Time-Dependent Materials*, 1999. **3**(2): p. 141-157.
106. Wu, X.L., et al., *Characterization of the thermoresponsive shape-memory effect in poly(ether ether ketone) (PEEK)*. *Journal of Applied Polymer Science*, 2014. **131**(3): p. 39844.
107. Wu, X.L., et al., *Characterization of polymeric shape memory materials*. *Journal of Polymer Engineering*, 2017. **37**(1): p. 1.
108. Rosu, L., et al., *Effect of UV radiation on the semi-interpenetrating polymer networks based on polyurethane and epoxy maleate of bisphenol A*. *Journal of Photochemistry and Photobiology A: Chemistry*, 2005. **169**(2): p. 177-185.
109. Woo, R.S., et al., *Environmental degradation of epoxy-organoclay nanocomposites due to UV exposure. Part I: Photo-degradation*. *Composites science and technology*, 2007. **67**(15): p. 3448-3456.
110. Stark, N.M. and L.M. Matuana, *Surface chemistry changes of weathered HDPE/wood-flour composites studied by XPS and FTIR spectroscopy*. *Polymer Degradation and Stability*, 2004. **86**(1): p. 1-9.
111. Yoshida, S., *Quantitative evaluation of an epoxy resin dispersion by*

- infrared spectroscopy*. Polymer Journal, 2014. **46**: p. 430.
112. Kim, H. and M.W. Urban, *Molecular Level Chain Scission Mechanisms of Epoxy and Urethane Polymeric Films Exposed to UV/H<sub>2</sub>O. Multidimensional Spectroscopic Studies*. Langmuir, 2000. **16**(12): p. 5382-5390.
113. Kabanov, V.Y., et al., *Radiation chemistry of polymers*. High Energy Chemistry, 2009. **43**(1): p. 1-18.
114. Spadaro, G., S. Alessi, and C. Dispenza, *Ionizing radiation-induced crosslinking and degradation of polymers*. Applications of Ionizing Radiation in Materials Processing; Sun, Y., Chmielewski, AG, Eds, 2017: p. 167-182.
115. Oroian, M., et al., *A Viscoelastic Model for Honeys Using the Time-Temperature Superposition Principle (TTSP)*. Food and Bioprocess Technology, 2013. **6**(9): p. 2251-2260.
116. Delfini, A., et al., *Evaluation of atomic oxygen effects on nano-coated carbon-carbon structures for re-entry applications*. Acta Astronautica, 2019. **161**: p. 276-282.
117. Wang, X., et al., *An experimental study on improving the atomic oxygen resistance of epoxy resin/silica nanocomposites*. Polymer Engineering & Science, 2007. **47**(7): p. 1156-1162.
118. Iisaka, K. and K.S. Yama, *Mechanical  $\alpha$ -dispersion and interaction in filled polystyrene and polymethylmethacrylate*. Journal of Applied Polymer Science, 1978. **22**(11): p. 3135-3143.
119. Hergeth, W.-D., et al., *Polymerization in the presence of seeds. Part IV: Emulsion polymers containing inorganic filler particles*. Polymer, 1989. **30**(2): p. 254-258.
120. Yang, S.-I., et al., *Thermal and mechanical properties of chemical crosslinked polylactide (PLA)*. Polymer Testing, 2008. **27**(8): p. 957-963.
121. Hooshangi, Z., S.A. Hossein Fegghi, and R. Saeedzadeh, *The effects of low earth orbit atomic oxygen on the properties of Polytetrafluoroethylene*. Acta Astronautica, 2016. **119**: p. 233-240.
122. Karvanis, K., et al., *Preparation and Dynamic Mechanical Analysis of Glass*

- or carbon Fiber/Polymer Composites. IOP Conference Series: Materials Science and Engineering, 2018. **362**: p. 012005.
123. Celina, M., K.T. Gillen, and R.A. Assink, *Accelerated aging and lifetime prediction: Review of non-Arrhenius behaviour due to two competing processes*. Polymer Degradation and Stability, 2005. **90**(3): p. 395-404.
  124. Flynn, J.H., *The 'Temperature Integral' — Its use and abuse*. Thermochemica Acta, 1997. **300**(1): p. 83-92.
  125. Zhang, F., et al., *Magnetic programming of 4D printed shape memory composite structures*. Composites Part A: Applied Science and Manufacturing, 2019. **125**: p. 105571.
  126. Lin, C., et al., *4D-Printed Biodegradable and Remotely Controllable Shape Memory Occlusion Devices*. Advanced Functional Materials, 2019. **29**(51): p. 1906569.
  127. Liu, Y., et al., *Synergistic effect enhanced shape recovery behavior of metal-4D printed shape memory polymer hybrid composites*. Composites Part B: Engineering, 2019. **179**: p. 107536.
  128. Robertson, I.D., et al., *Rapid energy-efficient manufacturing of polymers and composites via frontal polymerization*. Nature, 2018. **557**(7704): p. 223-227.
  129. Robertson, I.D., et al., *Rapid stiffening of a microfluidic endoskeleton via frontal polymerization*. ACS Applied Materials & Interfaces, 2014. **6**(21): p. 18469-18474.
  130. Luo, X. and P.T. Mather, *Preparation and characterization of shape memory elastomeric composites*. Macromolecules, 2009. **42**(19): p. 7251-7253.
  131. Kuang, W. and P.T. Mather, *Tuning of reversible actuation via ROMP-based copolymerization semicrystalline polymers*. Polymer, 2018. **156**: p. 228-239.
  132. Martinez, H., et al., *Ring-opening metathesis polymerization of 8-membered cyclic olefins*. Polymer Chemistry, 2014. **5**(11): p. 3507-3532.
  133. Zong, R., et al., *Thermal degradation kinetics of polyethylene and silane-crosslinked polyethylene*. Journal of applied polymer science, 2005. **98**(3): p. 1172-1179.

134. Wang, H., et al., *Effect of Microstructure on Chain Flexibility and Glass Transition Temperature of Polybenzofulvene*. *Polymer*, 2020: p. 123276.
135. Alonso-Villanueva, J., et al., *Ring-Opening Metathesis Polymerization Kinetics of Cyclooctene with Second Generation Grubbs' Catalyst*. *Journal of Macromolecular Science, Part A: Pure and Applied Chemistry*, 2010. **47**(11): p. 1130-1134.
136. Smay, J.E., J. Cesarano, and J.A. Lewis, *Colloidal Inks for Directed Assembly of 3-D Periodic Structures*. *Langmuir*, 2002. **18**(14): p. 5429-5437.
137. Yang, P., et al., *An ultra-simple universal model for the effective elastic properties of isotropic 3D closed-cell porous materials*. *Composite Structures*, 2020. **249**: p. 112531.
138. Visser, C.W., et al., *Architected Polymer Foams via Direct Bubble Writing*. *Advanced Materials*, 2019. **31**(46): p. 1904668.
139. Omairey, S.L., P.D. Dunning, and S. Sriramula, *Development of an ABAQUS plugin tool for periodic RVE homogenisation*. *Engineering with Computers*, 2019. **35**(2): p. 567-577.
140. Tian, W., et al., *Periodic boundary condition and its numerical implementation algorithm for the evaluation of effective mechanical properties of the composites with complicated micro-structures*. *Composites Part B: Engineering*, 2019. **162**: p. 1-10.
141. Van De Walle, W., S. Claes, and H. Janssen, *Implementation and validation of a 3D image-based prediction model for the thermal conductivity of cellular and granular porous building blocks*. *Construction and Building Materials*, 2018. **182**: p. 427-440.
142. Fernandes, H.R., D.U. Tulyaganov, and J.M.F. Ferreira, *Preparation and characterization of foams from sheet glass and fly ash using carbonates as foaming agents*. *Ceramics International*, 2009. **35**(1): p. 229-235.
143. Christensen, R.M., *Two Theoretical Elasticity Micromechanics Models*. *Journal of Elasticity*, 1998. **50**(1): p. 15-25.
144. Smith, D.S., et al., *Thermal conductivity of porous materials*. *Journal of Materials Research*, 2013. **28**(17): p. 2260-2272.
145. LOEB, A.L., *Thermal Conductivity: VIII, A Theory of Thermal Conductivity*

*of Porous Materials*. Journal of the American Ceramic Society, 1954. **37**(2):  
p. 96-99.

## Korean abstract

형상기억고분자는 높은 변형성, 경량성 및 자가전개가 가능한 특성으로 인해 우주 환경에서 전개 구조체로 주목 받고 있다. 그러나 열, 자외선, 원자 산소와 같은 우주 환경에 취약하다는 단점이 있다. 따라서 우주환경에서 장기간 물성을 예측할 수 있는 모델과 형상 기억 폴리머의 장기 내구성을 위한 적절한 설계 및 제조 방법이 필요하다.

우주 환경에서 형상 기억 고분자의 장기적 특성을 예측하기 위해 가속 시험 방법이 제안되었다. 실제로 우주 환경을 시뮬레이션하는 것은 어렵고 장시간 연속적으로 형상기억고분자의 물성 변화를 관찰하기 어렵다. 따라서 시간-온도 중첩 원리를 기반으로 우주 환경에서 형상기억고분자의 장기 내구성 예측 모델을 제안하였다. 형상 기억 고분자의 저장 모듈러스의 변화는 고진공, 원자 산소 및 자외선 노출의 세 가지 가혹한 조건을 포함하는 저궤도 환경에서 조사되었다. 저궤도 환경에서 형상기억 고분자의 기계적 물성은 극한 온도와 원자 산소에 의한 고분자 매트릭스 침식으로 인해 시간이 지남에 따라 저하되었다. 하지만 저궤도 환경에서 원자 산소 및 자외선 광선 노출에 의해 유도 된 가교로 인해 저장 모듈러스가 증가하는 반대 동작도 관찰되었다. 형상기억고분자에 대한 세 가지 가혹한 조건의 영향은 우주 환경 챔버에서 다양한 온도에서 수행 된 가속 테스트를 적용하여 개별적으로 특성화되고 시간-온도 중첩 원리를 사용하여 결합되었다. 저궤도 환경에서 형상기억고분자의 장기적인 기계적 거동은 세 가지 가속 테스트에서 얻은 이동 계수의 선형 곱으로 예측되었다. 형상 기억 성능의 경우 우주환경 노출시험에서 약간의 변화만을 나타냈다.

장기적인 내구성을 위해 다공성 형상기억고분자가 제안되었다. 다공성 고분자는 내부 표면적이 넓기 때문에 차폐 재료로 연구되고있다. 공기의 열전도율이 낮고 표면적이 넓어 복사 열전달의 반사가 발생으로 인해 단열재로 사용되며 기공과 매트릭스간의 계면에서의 내부 반사로 인한 전자파 차폐제로도 연구되고있다. 그러나 다공성 구조는 기계적 물성이 부족하다는 단점이 있다. 따라서 기계적 물성을 유지하면서 차폐성이 우수한 다공성 구조의 설계가 필요하다. 다공성 형상 기억 폴리머를 프린팅하기 위해 새로운 3D 프린팅 공정이 개발되었다. 형상기억고분자를 사용하여 기하학적으로 복잡한 프리스탠딩 구조를 인쇄하는 것은 형상기억고분자의 적용 분야를 확장하는 데 중요하다. 자가 발열을 특징으로하는 정면 중합이 가능한 poly(dicyclooctene) 네트워크에 스위칭 세그먼트를 만들 수 있는 cyclooctene을 추가하여 정면 중합이 가능한 열경화성 형상기억고분자를 합성하였다. 이 형상기억고분자의 3D 프린팅을 가능하게 하기 위해서 유변학적 특성은 겔화 시간을 조정하여 제어되었다. 노즐 시스템은 코어 쉘 노즐을 도입하여 고분자 매트릭스 내부에 기공이 생성될 수 있게 하였다. 다공성 구조가 성공적으로 인쇄되었고 구조적 특성이 분석되었다. 다양한 인쇄 조건에서 0과 0.1 사이의 낮은 다공성 영역의 형상기억고분자가 제조되었다. 유한 요소 해석을 통해 다공성 구조의 열/기계적 특성을 분석하고 검증했다. 탄성 계수와 열전도도는 다공도에 따라 선형적으로 감소했으며, 0.1의 다공도에서 탄성 계수는 19 % 감소하였고 열전도도는 12 % 감소했다. 마지막으로 다공성 구조를 갖는 형상기억고분자를 프리스탠딩 구조로 프린팅하고 형상 기억 특성을 특성화 하였다. 프린팅 된 프리스탠딩 구조의 형상기억고분자는 훌륭한 형상 기억성능을 보였다.

핵심어: 형상기억고분자, 우주환경, 다공성 구조, 3D 프린팅, 정면 중합

학번: 2015-22757